Doctoral Program in Aerospace Science and Technology
Department of Physics, Universitat Politècnica de Catalunya

EXACT COHERENT STRUCTURES IN THE TRANSITIONAL REGIME OF SHEAR AND CENTRIFUGAL FLOWS

Dissertation submitted for the Degree of Doctor of Philosophy
as a collection of published articles

Roger Ayats López

Supervised by:
Dr. Alvaro Meseguer and Dr. Fernando Mellibovsky

March 2022

EXACT COHERENT STRUCTURES IN THE TRANSITIONAL REGIME OF SHEAR AND CENTRIFUGAL FLOWS

Roger Ayats López, PhD.
Universitat Politècnica de Catalunya, 2022

Turbulence is one of the major concerns for most technological problems involving fluid motion. Specially in aeronautics, a turbulent boundary layer results in structural stresses, vibrations and higher aircraft drag, leading to a significant increase in fuel consumption. Therefore, trying to comprehend the origin of turbulence by studying its most common transition routes is a crucial first step towards its effective control.

Transition to turbulence of an homogeneous flow is frequently mediated by transient visits to highly nonlinear laminar coherent structures that usually are at the threshold between laminarity and turbulence. From a dynamical systems point of view, these structures are invariant sets in the infinite-dimensional Navier-Stokes phase space that here we aim to identify in different canonical flows. With the use of direct numerical simulations together with Newton-Krylov solvers and Arnoldi iteration method for the linear stability analysis, invariant sets such as equilibria, relative equilibria or periodic orbits are accurately computed and tracked along the parameter space to understand the transition mechanisms. From a mathematical perspective, dynamical systems and bifurcation theory provide the suitable framework to understand the hydrodynamic instabilities and transition to turbulence from a deterministic point of view. In addition, the use of spectral methods for the spatial discretisation is particularly convenient due to the exponential convergence of the numerical solutions.

In the first work, the onset of transition in two-dimensional Plane Poiseuille flow is analysed. A new family of Tollmien-Schlichting waves, breaking the usual half-shift and reflect symmetry of the classical ones, has been identified and tracked across parameter space. In addition, the role of another classical travelling wave family that did not participate in the localisation mechanisms has been clarified.

We continue by analysing the nonlinear mode competition in purely hydrodynamic and also magnetised Taylor-Couette flow. Finite-amplitude mixed-mode solution branches, arising from both purely hydrodynamic and magneto-rotational instabilities, are identified. These nonlinear mode interactions are efficiently com-

puted in suitable skewed computational domains instead of the classical orthogonal ones, allowing for a significant reduction of the required computational resources.

Finally, the generalisation of extensional flows between biorthogonally stretching-shrinking parallel plates is analysed. Under the assumption of the self-similar ansatz, three-dimensional steady equilibria of the Navier-Stokes equations are identified and systematically tracked in parameter space, to cover all possible configurations of the acceleration rates and thus unfold all occurring bifurcations. After the explorations, up to seven different families of steady solutions have been identified, some of them related in pairs with symmetries. When increasing wall acceleration rates, the solution branches interact by means of fold and codimension-2 cusp bifurcations, increasing the complexity of the topology of equilibria.

Besides the specific interest attached to each one of the three problems we have addressed, these have further served as a proof-of-concept for the applicability and suitability of the methods and tools developed in the course of this thesis, which may assist in tackling a vast range of problems across a huge variety of physics and engineering disciplines.

EXACT COHERENT STRUCTURES IN THE TRANSITIONAL REGIME OF SHEAR AND CENTRIFUGAL FLOWS

Roger Ayats López, PhD.
Universitat Politècnica de Catalunya, 2022

La turbulència és una de les principals preocupacions per a la majoria de problemes tecnològics relacionats amb el moviment de fluids. Especialment en el cas de l'aeronàutica, una capa límit turbulenta produeix tensions estructurals, vibracions i una major força d'arrossegament de l'aeronau que resulten en un increment significatiu del consum de combustible. Per tant, intentar comprendre l'origen de la turbulència, tot estudiant-ne les rutes de transició més habituals, és un primer pas indispensable cap al seu control efectiu.

La transició a la turbulència d'un flux homogeni sovint es caracteritza per visites transitòries a estructures coherents, laminars i altament no-lineals, que acostumen a trobar-se al llindar entre la laminaritat i la turbulència. Des del punt de vista dels sistemes dinàmics, aquestes estructures són conjunts invariants en l'espai de fase infinit-dimensional de les equacions de Navier-Stokes, que aquí es pretén identificar en diferents fluxos canònics. Mitjançant la integració temporal de les equacions, resolutors de Newton-Krylov i el mètode iteratiu d'Arnoldi per a l'anàlisi d'estabilitat lineal, els diferents conjunts invariants siguin equilibris, equilibris relatius o òrbites periòdiques són acuradament calculats i continuats al llarg de l'espai de paràmetres per tal d'entendre els mecanismes involucrats en la transició. Des d'una perspectiva matemàtica, els sistemes dinàmics i la teoria de bifurcacions proporcionen el marc adequat per a comprendre les inestabilitats hidrodinàmiques i la transició a la turbulència des d'un punt de vista determinista. A més, l'ús de mètodes espectrals per a la discretització espaial resulta particularment convenient degut a la convergència exponencial de les solucions numèriques.

En el primer treball, s'analitza l'inici de la transició del flux bidimensional de Poiseuille pla. En aquest cas, una nova família d'ones de Tollmien-Schlichting, que trenca la clàssica simetria de translació i reflexió, ha estat identificada i continuada al llarg de l'espai de paràmetres. A més, s'ha aclarit el rol d'una vella família d'ones viatgeres que en estudis previs no participava dels mecanismes de localització.

A continuació, s'analitza la competició entre modes no lineals en el flux purament hidrodinàmic i també hidromagnètic de Taylor-Couette. Branques de solucions d'amplitud finita, en forma de modes mixtes, han estat identificades sorgint

d'inestabilitats purament hidrodinàmiques i magnètiques. Aquestes interaccions de modes no lineals són eficientment calculades mitjançant dominis computacionals inclinats, enlloc dels clàssics ortogonals, permetent una reducció significativa dels recursos computacionals necessaris.

Finalment, s'analitza la generalització dels fluxos extensibles entre plaques paral·leles que s'estiren i s'encongeixen biortogonalment. Sota la hipòtesi d'autosimilitud, s'identifiquen fluxos estacionaris tridimensionals de les equacions de Navier-Stokes i s'estenen al llarg de l'espai de paràmetres, tot estudiant totes les possibles configuracions d'acceleració de les plaques i trobant totes les bifurcacions existents. En finalitzar les exploracions s'han identificat un total de set famílies de solucions, algunes d'elles relacionades per simetries. La complexitat de la topologia d'aquests equilibris creix notablement en incrementar l'acceleració de les plaques, quan les diferents branques de solucions interaccionen per mitjà de bifurcacions de node-sella i punts de codimensió-2 en forma de bifurcacions de cúspide.

Al marge de l'interès específic de cada un dels tres problemes estudiats, aquests també han servit com a demostració conceptual de l'aplicabilitat i idoneïtat dels mètodes i eines desenvolupats en el transcurs d'aquesta tesi, que poden ajudar a abordar un ampli ventall de problemes en una gran varietat de disciplines de la física i l'enginyeria.

Acknowledgements

I would like to express my sincere thanks to my advisers, Dr. Alvaro Meseguer and Dr. Fernando Mellibovsky, for their priceless advice and vital guidance. Their dedication and mentoring has been essential for the completion of this thesis as well as for my personal development as a researcher. I am also very grateful to Dr. Kengo Deguchi for his exceptional dedication and for giving me the opportunity to further my research.

I would like to show my deep appreciation to Prof. Francisco Marques for the enlightening and inspiring discussions, and the whole nonlinear Fluid Dynamics group for their support.

Finally, I am very grateful to my parents, sister, and particularly to Elisenda, whose patience and invaluable encouragement have been crucial during these years.

Contents

List of Figures

Chapter 1

Introduction

Transition to turbulence in shear flows is still an open question that remains unsolved and far from being completely understood. Although it has been intensively studied since Reynolds (1883) performed the famous pipe experiments, even the most simple flows are continuously revealing unexpected features and mechanisms.

Turbulence is one of the major concerns for most technological problems related with fluid motion. While turbulent flows are still useful for certain engineering applications involving fluid mixing, laminar flows are widely preferred for reducing frictional losses. This is for example the case of atmospheric flight, where a turbulent boundary layer results in higher aircraft drag and a significant increase in fuel consumption.

1.1 Transition to turbulence in aeronautics

Recent studies within the field reported that friction drag represents more than a 50% of the total drag of an aircraft in cruise (Schrauf, 2005). If only a 30% of the turbulent surfaces could maintain laminar flow, the total drag of the aircraft could be reduced by 12%.

The interest in boundary layer turbulent transition on aircraft surfaces increased in the late 1980s, when NASA, together with the U.S. Air Force Wright Laboratory and Boeing Commercial Airplane Group, initiated a cooperative program exploring the possibilities of the *hybrid laminar flow control*. This technology intended to

Figure 1.1. BLADE project A340 flight test with laminar aerofoils in the outer wing sections (Ramadier, 2017).

control and delay the initial transition to turbulence, using smooth wing surfaces and boundary layer suction. Flight tests on a B757 transport aeroplane reported excellent results, with a 6% of total drag reduction (Collier, 1994). Nowadays, most of the cutting edge research in the field is based on the development of passive techniques, enhancing the *natural laminar flow*. This concept basically consists in the use of accurate aerodynamic designs, especially conceived to control flow instabilities and mitigate the accidental disturbances that may trigger turbulence. For instance, this technique was recently tested within the BLADE project (Breakthrough Laminar Aircraft Demonstrator in Europe), where an A340 aircraft was equipped with especial outer wing sections using laminar aerofoils (see Fig. 1.1). By modifying such small portion of the aeroplane wet area, final tests reported a total fuel saving of 4.6% (IATA, 2019).

It is clear that understanding and predicting when flows become turbulent is of utmost importance in aeronautics. Such tailor-made aircraft designs, developed for delaying the appearance of turbulence, require a deep knowledge of the transitional mechanisms. Therefore, here we tackle this phenomena from a theoretical point of view, trying to comprehend the most common transitional routes as a first step towards effective control of turbulence.

1.2 Turbulence, dynamical systems and bifurcation theory

What is turbulence? Where does it come from? These two fundamental questions have and continue to raise interesting discussions within the scientific community. Although significant advances have been made during the last decade, no universal answers have yet been provided.

Early studies were basically statistical descriptions of turbulence, considering the fluid as an isotropic uniform entity. The law of the wall (Kármán, 1930), which describes the average velocity of the turbulent flow in the neighbourhood of a surface plate, and later Kolmogorov's scaling law (Kolmogorov, 1941), describing the energy distribution and dissipation across scales, are great examples of statistical descriptions providing valuable insights into the nature of turbulence. However, these approximations are not directly related to the governing equations, i.e., Navier-Stokes equations, so that the transition process can not be explained.

In order to successfully understand the transition, turbulence has to be addressed from a deterministic point of view. This alternative approach was initiated by Hopf (1942), who first reported a bifurcated time-periodic solution arising within a fluid dynamics context; although the concept of periodic orbit was first elucidated more than a century ago by H. Poincaré within the context of celestial mechanics (Poincaré, 2017). Later, Landau (1944) and Hopf (1948) stated the later so-called Landau-Hopf theory, suggesting that turbulence is the result of a deterministic route, where the flow sequentially incorporates new time frequencies as the Reynolds number is increased. This description of how a fluid flow becomes turbulent was widely accepted until the 1970s, when Ruelle & Takens (1971), Feigenbaum (1978) and later Pomeau & Manneville (1980) reported a rich variety of transition scenarios through successive bifurcations of nonlinear structures such as Hopf, period-doubling, or subcritical saddle-node, respectively.

Transition phenomena in shear flows has been successfully described by analysing the flow as a dynamical system driven by the governing equations. In this view the flow state evolves along the phase space, continuously approaching to and escaping from invariant sets. Fig. 1.2 illustrates this scenario by representing a finite portion of an hypothetical infinite-dimensional phase space projected in a two-dimensional plane, where the invariant sets (saddles in black bullets) are connected through

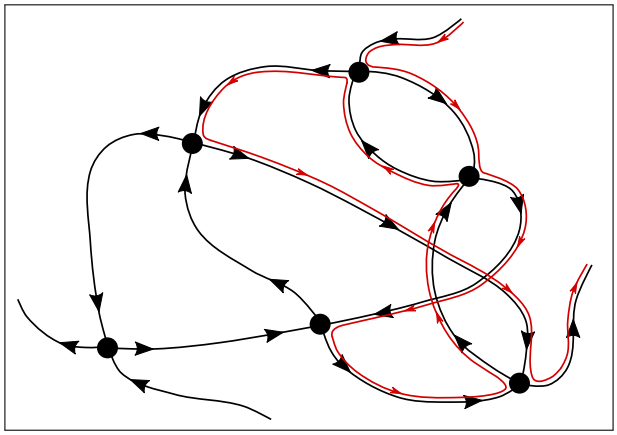

Figure 1.2. Finite portion of a phase space dominated by saddle solutions (black bullets), which are connected though different manifolds (black lines). Turbulence (red line) is the path visiting some of these invariant sets.

different manifolds (black lines). Turbulence is the path (red line) visiting several sets, where the dynamics in each rendezvous is locally dominated by the stable and unstable manifolds of the saddles.

It can be concluded that such invariant sets are, in fact, exact numerical solutions of the Navier-Stokes equations, usually referred to as *exact coherent structures* (ECS). When the flow approaches these states, simple spatio-temporal dependence is identified, resembling different kinds of coherent structures such as travelling (or rotating) waves and (relative) periodic orbits. ECS appear as a general feature of shear flows, being identified in such diverse flows as Plane Couette flow (Nagata, 1990; Viswanath, 2007; Schneider *et al.*, 2010; Kreilos & Eckhardt, 2012), Taylor-Couette flow (Meseguer *et al.*, 2009a; Deguchi & Altmeyer, 2013; Krygier *et al.*, 2021), Plane Poiseuille flow (Zammert & Eckhardt, 2014; Mellibovsky & Meseguer, 2015; Ayats *et al.*, 2020b), or pipe flow (Hof *et al.*, 2004; Wedin & Kerswell, 2004; Mellibovsky & Meseguer, 2009). Furthermore, recent studies show that ECS are a structural ingredient for the transition to turbulence (Kerswell, 2005; Schneider *et al.*, 2007; Eckhardt *et al.*, 2008; Kawahara *et al.*, 2012) and play a key role in the self-sustaining process (Waleffe, 1997, 2003).

In addition to the dynamical systems approach, bifurcation theory provides the perfect framework for understanding how the invariant sets are created or annihilated within the parameter space. In this theory, the flow complexity is described from topological changes in phase space due to successive bifurcation events. It is worth mentioning that, although bifurcation theory is originally formulated for

finite-dimensional systems, it can be applied for genuinely infinite-dimensional dynamical systems (Coullet & Spiegel, 1983) formulated in functional Hilbert spaces. In practice, however, we adapt the bifurcation methods to finite, but huge, dimensional systems, resulting from the spatial discretisation and truncation of the Navier-Stokes equations. In this sense, the use of Newton-Krylov solvers (Kelley, 2003) together with Arnoldi iteration method (Arnoldi, 1951) are crucial for the computation and stability analysis of ECS in such high-dimensional systems.

1.3 Supercritical and subcritical transition

Depending on the nature of the ECS branches, transition can be classified as *supercritical* or *subcritical*. In a supercritical scenario, flow complexity progressively increases with the sequence of bifurcations, typically starting with simple equilibria like travelling waves that eventually undergo a transition to time-space-modulated solutions. In fact, this transition is sometimes referred as *forward* or *safe* bifurcation scenario, as the amplitude of the emerging ECS progressively grows when going further into the instability region. In general, this process can be defined as fully reversible in the sense that, when moving along the parameter space, the observed flow structure is independent from the exploration path. Ruelle-Takens and Feigenbaum scenarios are some examples of classic supercritical paths towards chaotic dynamics (Eckmann, 1981).

More interesting are subcritical scenarios, which can experience transition in the absence of linear instability of the base flow. In this case, ECS emanate from saddle-node bifurcations, whose lower branches normally dictate the amplitude of the disturbances triggering transition, and the upper branches participate in the formation of chaotic attractors leading to turbulence (Mellibovsky & Eckhardt, 2012; Kreilos & Eckhardt, 2012). In the case of experiencing a base flow instability, the transition is completely abrupt. Just slightly above the neutral stability curve, perturbations exponentially grow towards the stable ECS, which possess a great amplitude from its onset. In contrast to the supercritical scenario, subcritical transitions are history- or path-dependent, typically exhibiting hysteretic cycles and bistability. As a result of this, localised turbulence patterns surrounded by large laminar fractions are frequently observed in the first steps of transition, for the lowest Reynolds numbers (Barkley & Tuckerman, 2005; Meseguer *et al.*, 2009b; Paranjape *et al.*, 2020). This

kind of subcritical scenarios are precisely object of study in this research, specially in the first publication shown in §2.3.

1.4 Methodology

As explained in previous sections, dynamical systems and bifurcation theory provide the suitable framework to understand hydrodynamic instabilities and transition to turbulence from a deterministic point of view. In particular, we aim for the identification of stable and unstable invariant sets within the infinite-dimensional Navier-Stokes phase space. These invariant sets, such as equilibria, relative equilibria (i.e., steady patterns in suitable co-moving reference frames), or periodic orbits, are in fact steady flows, travelling waves or pulsating waves, respectively.

In the three articles included, the incompressible Navier-Stokes equations are spatially discretised using spectral methods, as they are particularly convenient for the simple geometries of the canonical flows here studied and allow for exponential convergence of the discretised solutions. For Plane Poiseuille flow (chapter 2) and flows between stretching parallel plates (chapter 4), a Galerkin formulation together with Fourier and Legendre spectral expansions are implemented. By contrast, due to the particularity of the annular geometry, for the Taylor-Couette flow (chapter 3) we adapt the alternative solenoidal Petrov-Galerkin scheme, which uses Fourier-Fourier-Chebyshev spectral expansions, described in Meseguer *et al.* (2007). In this case, the use of solenoidal spectral basis is particularly convenient to satisfy incompressibility and remove pressure from the weak formulation.

When computing stable and unstable equilibria, travelling waves or relative periodic orbits, the resulting system of nonlinear equations must be solved by using *Jacobian-free* Newton–Krylov methods (Kelley, 2003), requiring just the action of the Jacobian operator and avoiding the computation of the full matrix as in the classical Newton-Raphson methods. This technique is especially suitable for solving large algebraic systems of equations, in our case enforced by the choice of high spectral resolutions to satisfy the desired convergence. Then, the computed exact solutions are tracked along the parameter space by means of pseudo-arclength continuation methods (Kuznetsov, 2004).

Linear stability analyses are also necessary to uncover the role of the computed ECS branches and fully understand the transition scenario. However, to monitor ECS stability properties, the computation of the whole spectrum of eigenvalues is unnecessary and, most of the times, unfeasible. Therefore, Arnoldi iteration method combined with the appropriate Cayley transformations allows for the computation of the leading eigenvalues, necessary to identify potential bifurcations (Trefethen & Bau, 1997).

Finally, for the time discretisation we implement a fourth-order IMEX method, using fourth-order implicit backward-differences for the linear stiff terms and a fourth order explicit polynomial extrapolation for the nonlinear terms (Cox & Matthews, 2002). In addition, all computations are initialised by means of a fourth-order Runge-Kutta method (Meseguer, 2020) to ensure sufficient temporal accuracy.

1.5 Outline

This dissertation is composed of three publications indexed by the JCR (*Journal Citations Report*), each one exploring the transitional scenario of a different canonical flow. Chapter 2 introduces the Tollmien-Schlichting wave instability and its participation in the transition of two-dimensional Plane Poiseuille flow. Chapter 3 is devoted to Taylor-Couette flow and the computation of fully nonlinear spiral mode interactions. Chapter 4 presents the computation and analysis of the steady ECS appearing in the generalisation of flows between orthogonally stretching planes. Finally, the general conclusions are discussed in chapter 5.

Chapter 2

Symmetry-breaking waves and localisation mechanisms in plane Poiseuille flow

The flows in pipes and channels, which are characterised by a mean current going from upstream to downstream, are of special interest for their applications in engineering. It is well known that most of these flows become turbulent when increasing the speed of the mean current, i.e., the Reynolds number, leading to a significant increase of energy consumption and other undesired effects. Therefore, studying the primary instabilities and mechanisms that may trigger turbulence is of utmost importance to delay or even control the transition.

2.1 Introduction

A natural question when analysing the transition is the role of viscosity. Flows involved in many engineering applications such as pipes and channels are inviscidly stable according to *Rayleigh's* criterion, due to the absence of inflectional flow profiles (Rayleigh, 1879). Although these flows do not exhibit inviscid instabilities, like the *Kelvin-Helmholtz* instability, they still undergo a transition to turbulence under certain conditions. In general, laminar viscous flows may exhibit transition to turbulent flows in two distinct scenarios. The most basic case is in the presence of a base flow instability, where viscous effects are responsible for the modal growth of

infinitesimal disturbances that, after a natural selection of the wavelengths, eventually grow, nonlinearly saturate, and lead to a new flow, typically in the form of wavetrains like *Tollmien-Schlichting* waves. By contrast, in the second scenario the transition is produced in absence of base flow instability. In this case, viscous effects are responsible for a transient non-modal growth of small finite-amplitude perturbations, eventually amplified by nonlinear mechanisms such as the *lift-up effect* (Brandt, 2014), and saturated by the usually known as the *self-sustaining process* (Waleffe, 1997).

2.1.1 Tollmien-Schlichting waves

The classical example for starting with the analysis of transition to turbulence is to consider a steady, incompressible and two-dimensional uniform stream flowing on top of a semi-infinite flat plate. The basic laminar solution for this flow was formally derived by Blasius (1908) following the hypotheses of Prandtl (1904). It is based on a self-similar solution whose characteristic two-dimensional velocity profile $U(y)$ is shown in Fig. 2.1. Although observable in experiments and numerical simulations, in practice the Blasius' solution is limited to the vicinity of the leading edge and cannot explain the transition phenomena.

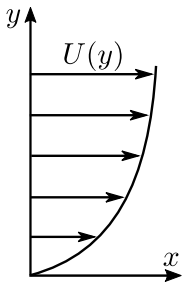

Figure 2.1. Blasius velocity profile.

For this flow, the streamwise Reynolds number is usually defined as

$$\mathrm{Re} = \frac{U_\infty \, \delta_1}{\nu}, \tag{2.1}$$

where U_∞ is the free-streamwise velocity, ν is the kinematic viscosity and δ_1 is the displacement thickness of the boundary layer

$$\delta_1 = 1.7208 \sqrt{\frac{\nu \, x}{U_\infty}}, \tag{2.2}$$

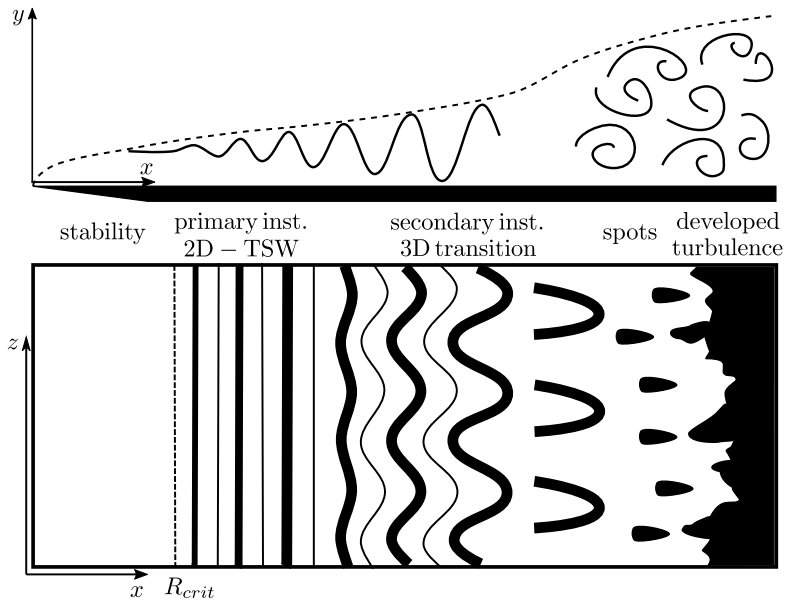

Figure 2.2. Schematic transition to turbulence over a flat plate via TSW instability. (Following Manneville (2010, figure 6.19)).

with x being the position in the free-stream direction. Near the leading edge, corresponding to low values of Re, the Blasius velocity profile is linearly *stable*. When introducing small disturbances to the flow, after some transients the perturbation decays and the characteristic laminar velocity profile is recovered. However, by going further along the plate and increasing Re above a critical value $\mathrm{Re}_{crit} = 519.4$ (Schmid & Henningson, 2001), the perturbation no longer decays but a very specific set of wavelengths are linearly amplified. These particular disturbances grow until nonlinear effects become relevant and saturate in two-dimensional finite amplitude steady states. The first attempt to explain this effect was undertaken by Tollmien (1928) and Schlichting (1933), who performed linear stability analysis of the flow and obtained the fundamental two-dimensional disturbing modes responsible for the emergence of travelling waves, known as Tollmien-Schlichting waves (TSW). This transition scenario is depicted in Fig. 2.2 by showing schematic cross-sections of the boundary layer over a flat plate.

When further increasing Re, two-dimensional solutions progressively grow and eventually exhibit secondary spanwise instabilities leading to three-dimensional modulated TSW. This secondary stage of the transition develops much faster than the primary instability and, after a relatively short Re interval, the three-dimensional

coherent structures experience a general breakdown. Nonlinearities and a high number of instabilities suddenly increase flow complexity, initially leading to turbulent spots and later on to developed turbulence, continuously spreading to smaller scales (Schubauer & Skramstad, 1947; Schmid & Henningson, 2001).

Although there are many different transitional scenarios, the TSW instability mechanism is one of the most common routes by which a laminar shear flow becomes turbulent. Thus, it is of crucial importance for many engineering applications involving fluid motion. For instance, streamwise TSW together with attachment line, centrifugal, and crossflow are the fundamental instability mechanisms causing transition in aeroplanes' wings (Saric *et al.*, 2003). More surprisingly, TSW are not only present in industrial applications, but also in nature itself. Some animal species, such as *Tursiops truncatus* dolphins, have developed a very special epidermis capable of suppressing TSW, thus maintaining laminar flow and drastically reducing the frictional forces (Babenko & Surkina, 1969; Carpenter *et al.*, 2000). This natural evolution clearly shows the importance of TSW for such animals and their need to cope with this transition mechanism.

2.1.2 Plane Poiseuille flow

In fact, TSW are two-dimensional streamwise unstable waves arising in all sorts of wall-bounded shear flows such as *Plane Poiseuille* flow (PPF), not only limited to boundary layers. In its fundamental form, PPF is defined as a steady, pressure-driven, incompressible Newtonian fluid confined in between two infinite parallel plates. Its basic laminar solution is the well known streamwise-independent parabolic velocity profile

$$u(y) = \frac{K}{2\,\nu\rho}\,(h^2 - y^2)\,\hat{x}, \tag{2.3}$$

where u is the streamwise velocity, K the pressure drop, ν the kinematic viscosity, ρ the density, h the half distance between plates and y the wall normal coordinate. Fig. 2.3 depicts a sketch of this particular solution.

For its simplicity, PPF is the ideal canonical flow to study in depth the TSW transitional mechanism. Even its two-dimensional simplification, although without spanwise modulations and the final breakdown, can still provide valuable information about how the first instabilities develop. In this sense, Squire (1933) analysed the effect of two- and three-dimensional disturbances by performing a normal

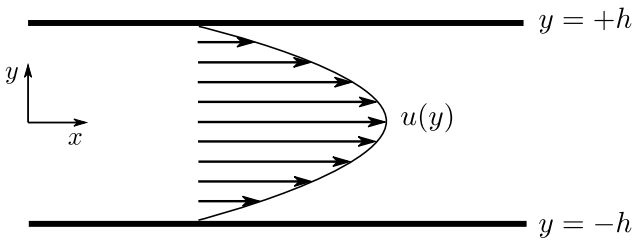

Figure 2.3. PPF streamwise-independent laminar parabolic velocity profile.

mode analysis with periodic boundary conditions in streamwise-spanwise directions. Squire concluded that the first instability experienced by the laminar base flow is two-dimensional, with oblique instabilities occurring always at higher Reynolds numbers. Thus, to obtain the Re_{crit} it is sufficient to consider exclusively two-dimensional disturbances (Drazin & Reid, 1981). It is certainly true that Squire's theorem is only valid for unidirectional open base flows and does not apply to more complex flows. However, two-dimensional analyses are still active as it is interesting to fully understand the underlying transition mechanism in order to shed light on three-dimensional flows; see Page *et al.* (2020) for a recent two-dimensional work in viscoelastic channel flows. For this reason, we choose to study two-dimensional PPF by computing and analysing in-depth the first nonlinear structures.

Linear stability analysis of PPF leads to the Orr-Sommerfeld equation, which formally consists in a normal mode analysis of streamwise periodic perturbations in a linearised version of the Navier-Stokes equations (Orr, 1907; Sommerfeld, 1908). This equation remained unsolved until Thomas (1953) computed the first numerical solution using a finite differences scheme. Finally, Orszag (1971) significantly refined Thomas' solution and provided accurate values for the PPF critical parameters: $\mathrm{Re}_{crit} = 5772.22$ and $k_{crit} = 1.02056$, being k the streamwise wavenumber of the perturbation. Therefore, driving the flow above the critical Reynolds number, $\mathrm{Re} > \mathrm{Re}_{crit}$, small disturbances linearly grow and eventually saturate in the form of nonlinear TSW. In contrast to the Blasius boundary layer, for most values of k the TSW are highly subcritical and coexist with the stable laminar base flow, extending down to as far as $(k_{\mathrm{SN}}, \mathrm{Re}_{\mathrm{SN}}) \approx (1.35, 2608)$ at onset.

Following Mellibovsky & Meseguer (2015), the flow is driven at *constant mass flux* to better reproduce experimental setups such as in Pugh & Saffman (1988) and Hof *et al.* (2003). Former studies considered an alternative driving mechanism by enforcing a constant pressure gradient (Rozhdestvensky & Simakin, 1984; Ehren-

stein & Koch, 1991), reporting the TSW onset at $\mathrm{Re}^{\mathrm{p}}_{\mathrm{SN}} \approx 2939$. Both formulations are broadly qualitatively equivalent as they exhibit similar global bifurcation scenarios. However, dynamics significantly differ when analysing in detail the emerged nonlinear structures, being usually richer for the constant mass flux assumption (for a detailed dynamics comparison see Casas & Jorba (2004, 2012)).

Sub and superharmonic bifurcations of Tollmien-Schlichting waves

We solve PPF by imposing no-slip boundary conditions at the walls and periodic boundary conditions in the streamwise direction. Our computational domain is $(x, y) \in [0, \Lambda] \times [-h, h]$, where Λ is the streamwise length of the channel, initially being $\lambda_0 = 2\pi/k_0$, where k_0 is the TSW characteristic wavenumber obtained from the linear stability analysis of the PPF. Within this domain, TSW can be captured and tracked along the parameter space, and represented as a three-dimensional surface such as the one depicted in §2.3 Fig. 1a of the paper.

We first analyse the spatial superharmonic stability of the emerged solutions by considering periodic perturbations of characteristic wavelength $\lambda = 2\pi/k$, where $k = m\,k_0$ ($m \in \mathbb{N}$), fitting m times within the domain. Time-periodic pulsating TSW (PTSW) emerge from a superharmonic Hopf bifurcation of the TSW when Re is increased. In addition, in the present research we have identified a new pitchfork bifurcation, located in the lower branch of the TSW surface, that breaks the half-shift & reflect symmetry of the TSW; see this classical symmetry in Fig. 2.4a. The new *asymmetric* TSW branches (ATSW) experience a bias towards one of the channel walls, exhibiting an asymmetry between the upper and lower vortex, which is schematically depicted in Fig. 2.4b.

Furthermore, it is even more interesting to analyse the stability of TSW to spatially subharmonic disturbances, which are perturbations of a longer wavelength than the fundamental TSW domain, $k = k_0/m$ with $m \in \mathbb{N}$. To do this, for $n \in \mathbb{N}$ and $m = 1, ..., n$, we consider a wave train of n replicas of the original TSW (R_n), filling a domain of length $\Lambda = n\lambda_0$, and formally compute the superharmonic stability analysis to perturbations fitting m times in the new replicated domain (Prat *et al.*, 1998; Melnikov *et al.*, 2014); for further details see §2.3 App.B of the paper. TSW typically undergo subharmonic Hopf bifurcations leading to *time-periodic space-modulated* solutions (MTSW). Depending on the domain length, i.e., the replica number, these relative periodic orbits exhibit different behaviours. For low values

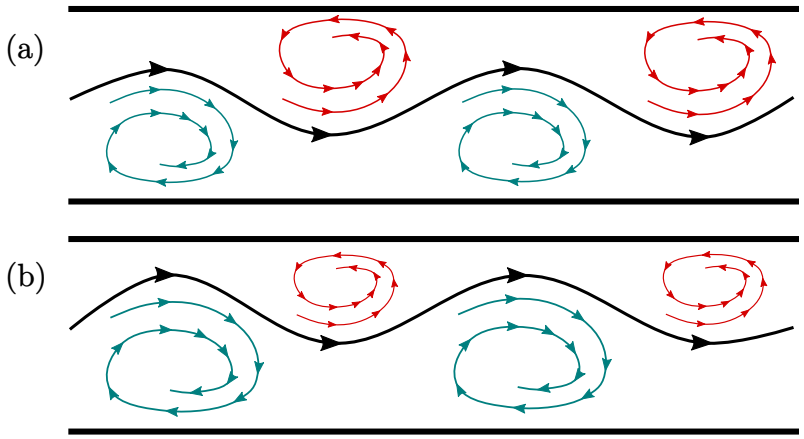

Figure 2.4. (a) Usual half-shift & reflect symmetry of the TSW. (b) Bias towards one of the channel walls of the new ATSW due to the pitchfork symmetry-breaking.

of n, MTSW appear as domain-filling self-replica connections of time-pulsating travelling waves. For intermediate values of n, these relative periodic orbits typically bridge consecutive TSW replicas $\mathrm{R}_n - \mathrm{R}_{n+1}$, with a spatial modulation allowing for the accommodation of the extra pair of vortices. Finally for long enough domains, MTSW emerge and never reconnect with any subsequent replica, allowing for a clear localisation of the modulated wave surrounded by laminar flow (Mellibovsky & Meseguer, 2015). In addition, ATSW branches also undergo subharmonic Hopf bifurcations leading to asymmetric time-periodic solutions (MATSW).

2.2 Research objectives

The main goal of this research is to continue the former study by Mellibovsky & Meseguer (2015) in two-dimensional PPF, investigating the fate of a novel MTSW family that had no participation in the localisation mechanism. These waves remained invariable, located on the right-hand side lower branch of the TSW paraboloid surface, as simply self-replica connections of time-pulsating relative periodic orbits. In the present study, we explore the connections between these MTSW and the existing branches, clarifying their role in the localisation mechanism.

In addition, we search for travelling and time-periodic solution branches breaking the usual half-shift and reflect symmetry of all Tollmien-Schlichting waves known until now, trying to shed light on the streamwise pseudo-homoclinic snaking mechanism investigated also in Mellibovsky & Meseguer (2015).

2.3 Indexed publication

This section reproduces a complete version of Ayats *et al.* (2020b), summarising all the performed research in PPF.

Symmetry-breaking waves and space-time modulation mechanisms in two-dimensional plane Poiseuille flow

Roger Ayats and Alvaro Meseguer*
Department of Physics, Universitat Politècnica de Catalunya, 08034 Barcelona, Spain

Fernando Mellibovsky
Department of Physics–Aerospace Engineering Division, Universitat Politècnica de Catalunya, 08034, Barcelona

(Received 2 April 2020; accepted 25 August 2020; published 18 September 2020)

We investigate two distinct scenarios of spatial modulation that are candidate mechanisms for streamwise localization of waves in two-dimensional plane Poiseuille flow. The first one stems from a symmetry-breaking bifurcation that disrupts the half-shift and reflect equivariance of *Tollmien-Schlichting waves* (TSW). A new state, an *asymmetric* TSW (ATSW), emerges from unstable lower-branch TSWs at subcritical Reynolds number and undergoes subharmonic Hopf bifurcations that lead to branches of asymmetric time-periodic space-*modulated* waves (MATSW). Streamwise modulation does not evolve into localization within the range of parameters explored. In breaking the last standing remnants of the reflectional symmetry about the channel midplane, ATSW and MATSW admit a bias toward either one of the channel walls, thus bearing a potential for explaining near-wall structures that are typical of developed turbulence. The second scenario follows the fate of a branch of time-periodic space-*modulated* TSWs (MTSW) initially discovered by Mellibovsky and Meseguer [J. Fluid Mech. **779**, R1 (2015)]. We find that these waves can lead to localization but the mechanism is not new, as they do so through their connection, by means of a codimension-2 bifurcation point, with other known localizing MTSWs. The codimension-2 point is, however, responsible for the appearance of MTSWs that exclusively bridge upper-branch TSW-trains of different number of replicas. In this respect, these MTSWs possess all required properties that single them out as possible constituents of the strange saddle that governs domain-filling turbulent dynamics at high Reynolds numbers.

DOI: 10.1103/PhysRevFluids.5.094401

I. INTRODUCTION

Subcritical transition and intermittency phenomena in wall-bounded shear flows remains one of the most intriguing and still unsolved conundrums in fluid dynamics [1,2]. Understanding and predicting when the flow in pipes and channels becomes unstable and eventually turbulent is of the utmost importance to many branches of science and technology, yet shear flow transition often occurs at moderate Reynolds numbers for which the underlying laminar base flow is linearly stable [3,4]. Nonlinear instabilities and transition in shear flows have been intensively studied over the last couple of decades, mainly following the identification of exact solutions to the Navier-Stokes equations in pipe flow [5–8], plane Couette flow [9–13], or plane Poiseuille flow [14,15], this latter henceforth referred to as PPF. These solutions are exact coherent flow states, traveling waves in the

*Corresponding author: alvaro.meseguer@upc.edu

case of PPF, that start appearing out of the blue at finite Reynolds number in saddle-node bifurcations. When increasing the Reynolds number, the *nodal* or *upper* branch typically exhibits secondary bifurcations that lead to increasingly complex flows featuring time-periodicity, quasi-periodicity and eventually chaotic and turbulent dynamics. Although bifurcated nodal solutions resulting from local bifurcations must in principle remain locally attracting, experiments and numerical simulations reveal that turbulent dynamics is transient [16,17] at low to moderate Reynolds numbers. The eventual relaminarization of turbulent flow is a consequence of a global bifurcation involving a *boundary crisis* [18], whereby the phase-space boundary of the chaotic attractor resulting from successive bifurcations of the nodal branch collides with the saddle or some solution branch bifurcated from it, thus puncturing the local attractor and morphing it into a strange saddle. This motivates a careful inspection of the bifurcations undergone by the unstable *saddle* or *lower* branch of traveling wave solutions, which is a challenging computational task. The main reason is that these traveling waves are highly unstable so they cannot be identified by simply time-stepping the Navier-Stokes equations. The analysis requires instead the use of continuation algorithms purposely designed to accurately compute and track the unstable traveling waves in parameter space. Relevant portions of their eigenspectrum can then be computed via linear stability analysis with matrix-free Arnoldi-iteration and monitored to detect secondary bifurcations.

One of the most common and intriguing features of shear-flow turbulence is its *localized* nature. For low or even moderate Reynolds numbers, turbulence typically appears in localized *patches* of a finite extent surrounded by laminar flow. Experiments and direct numerical simulations in pipe, channel, and annular flows have systematically reported localized turbulence in the form of *puffs* or *turbulent spots* [19–23]. The underlying mechanisms responsible for localization cannot be merely explained in terms of spatially periodic coherent states such as the aforementioned traveling waves. Pipe flow simulations [24] have identified exact Navier-Stokes solutions in the form of localized time-periodic traveling waves that govern the dynamics on the basin boundary that separates laminar steady flows from localized turbulence. In this sense, they constitute an *edge-state*, whose stable manifold separates, if only locally, laminar and turbulent dynamics. These solutions appear in saddle-node bifurcations, such that the nodal solution is an essential constituent of localized turbulent dynamics. The mechanism underlying pipe flow localization was first described by [25] in terms of subharmonic instabilities connecting traveling-wave solution branches of different wavelengths. Along the same lines, [14], MM15 for short, studied the localization mechanism in two-dimensional PPF, where stable/upper-branch TSWs become unstable to perturbations of wavelength longer than their own. Both time and space modulation arises from these subharmonic Hopf bifurcations, such that the resulting states include propagating wave dislocations. Continuation to larger fundamental wavelength of these new solutions often results in the eventual accommodation of an extra traveling wave replica that fills the gap generated by the dislocation and the branch lands anew on the family of TSWs at another subharmonic Hopf bifurcation of the lower/unstable branch. Occasionally, for low Reynolds numbers, the dislocation leaves a gap that widens indefinitely and the states become fully localized no matter how large the domain size grows. In this case, asymptotic analysis has recently shown that the upstream and downstream interfaces of the resulting localized patch decay exponentially towards the base parabolic flow [26].

MM15 carried the issue of localization further to test what was left of the so-called *snakes and ladders* scenario observed in plane Couette spanwise localization [11] among many other extended problems featuring a Z_2 symmetry, in a system, PPF, where this symmetry is completely broken. They concluded that a mechanism similar to streamwise snaking was still possible, although structurally unstable with respect to small variations in domain periodicity length.

We focus here on the systematic exploration of two phenomena conspicuously overlooked by MM15. On the one hand, we search for traveling and time-periodic-traveling solution branches breaking the half-shift and reflect symmetry of all known Tollmien-Schlichting waves (TSW) and the related half-period and reflect equivariance of bifurcating time-periodic space-*modulated* TSWs (MTSW). On the other hand, we investigate the fate of a family of MTSWs that allegedly had no bearing in the localization mechanism investigated there. To do so, we perform a comprehensive linear

stability analysis of the lower branch of TSWs with respect to disturbances of their same wavelength (*superharmonic*), but also, and most importantly, with respect to disturbances of wavelengths that are integer multiples of their own (*subharmonic*) in streamwise-replicated computational domains. This is systematically done for TSWs of all possible wavelengths and for a wide range of Reynolds numbers, with the aim of identifying and monitoring all subharmonic and symmetry-breaking bifurcations potentially leading to hitherto unknown branches of traveling or time-periodic-traveling waves.

The paper is structured as follows. In Sec. II we provide an accurate description of the mathematical formulation of the problem. Section III starts with a quick review of all known TSWs, along with an analysis of their stability and bifurcation, both subharmonic and superharmonic. Section IV then dives into the search, parametric continuation, and subharmonic stability analysis of asymmetric traveling wave solutions (ATSW) emerging from the lower branch of TSWs, and provides a full description of the pitchfork bifurcations whereby their half-shift and reflect symmetry is broken. Section V is devoted to a systematic exploration of the time-periodic space-modulated asymmetric waves (MATSW) that emerge from subharmonic Hopf bifurcations of ATSWs. In Sec. VI we track modulated-wave solution branches that had not been previously investigated and thoroughly unfold the codimension-2 bifurcation through which they are related to all other known branches of modulated waves. Finally, we outline the main results and summarize our conclusions in Sec. VII.

II. MATHEMATICAL FORMULATION

We consider an incompressible Newtonian fluid of kinematic viscosity ν and density ρ confined in between two infinite parallel plates $2h$ apart (h is the half-gap). The two-dimensional domain in cartesian coordinates is therefore $(x, y) \in (-\infty, \infty) \times [-h, h]$. Following MM15, the flow is driven at *constant mass flux* to better mimic the conditions found in experimental setups for extended systems such as pipes or channels [27,28].

The flow is governed by the Navier-Stokes equations

$$\partial_t \mathbf{u} + (\mathbf{u} \cdot \boldsymbol{\nabla})\mathbf{u} = -\frac{1}{\rho}\boldsymbol{\nabla} p + \nu \nabla^2 \mathbf{u} - \frac{\Pi}{\rho}\,\hat{\mathbf{x}}, \qquad \boldsymbol{\nabla} \cdot \mathbf{u} = 0, \tag{1}$$

where $\mathbf{u} = (u, v)$ and p are the velocity and pressure fields, respectively. In Eq. (1), Π is the streamwise driving pressure gradient, that is instantly adjusted to satisfy the prescribed constant mass flux. No-slip boundary conditions are imposed at the walls, $\mathbf{u}(x, \pm h; t) = (0, 0)$, while the flow is assumed periodic in the streamwise direction $[\mathbf{u}, p](x + 2\pi/k, y; t) = [\mathbf{u}, p](x, y; t)$, where k is the streamwise wave number.

All variables are rendered dimensionless using h and $3U/2$ as length and velocity scales, respectively, where U is the mean streamwise velocity. Accordingly, the Reynolds number is defined as $\mathrm{Re} = 3hU/2\nu$ and the basic laminar solution of PPF is the streamwise-independent parabolic velocity profile $\mathbf{u}_0 = (1 - y^2)\,\hat{\mathbf{x}}$. The constant mass flux constraint is straightforwardly implemented by formulating the problem in the streamfunction formalism, so that Eq. (1) reads

$$\partial_t \nabla^2 \Psi + (\partial_y \Psi)\partial_x(\nabla^2 \Psi) - (\partial_x \Psi)\partial_y(\nabla^2 \Psi) = \frac{1}{\mathrm{Re}}\nabla^4 \Psi, \tag{2}$$

where $\Psi(x, y; t)$ is the nondimensional streamfunction. Equation (2) is supplemented with no-slip boundary conditions at the walls, along with periodic boundary conditions in the streamwise coordinate

$$\partial_y \Psi(x, \pm 1; t) = \partial_x \Psi(x, \pm 1; t) = 0, \qquad \Psi\left(x + \frac{2\pi}{k}, y; t\right) = \Psi(x, y; t). \tag{3}$$

By arbitrarily choosing $\Psi(x, 1; t) = 2/3$ and $\Psi(x, -1; t) = -2/3$, the volumetric flow rate condition

$$\mathrm{Q} = \Psi(x, 1; t) - \Psi(x, -1; t) = 4/3 \tag{4}$$

ensures the constant nondimensional mean axial velocity is exactly and permanently 2/3. In this formulation, the basic laminar PPF solution is expressed as $\Psi_0(y) = y(1 - y^2/3)$.

We analyze the effect of finite amplitude perturbations $\widetilde{\Psi}(x, y; t)$ added to the basic PPF,

$$\Psi(x, y; t) = \Psi_0(y) + \widetilde{\Psi}(x, y; t), \tag{5}$$

where $\widetilde{\Psi}$ satisfies periodic boundary conditions in the streamwise coordinate, along with homogeneous *Neumann-Dirichlet* boundary conditions in the wall-normal direction:

$$\widetilde{\Psi}\left(x + \frac{2\pi}{k}, y; t\right) = \widetilde{\Psi}(x, y; t), \qquad \widetilde{\Psi}(x, \pm 1; t) = \partial_x \widetilde{\Psi}(x, \pm 1; t) = \partial_y \widetilde{\Psi}(x, \pm 1; t) = 0. \tag{6}$$

Formal substitution of the perturbed field Eq. (5) in Eq. (2) yields

$$\partial_t \nabla^2 \widetilde{\Psi} = \mathbf{L}_{\mathrm{Re}}(\widetilde{\Psi}) + \mathbf{N}(\widetilde{\Psi}), \tag{7}$$

where the linear biharmonic-advective and nonlinear convective terms are

$$\begin{cases} \mathbf{L}_{\mathrm{Re}}(\widetilde{\Psi}) &= \frac{1}{\mathrm{Re}} \nabla^4 \widetilde{\Psi} - (1 - y^2) \partial_x \nabla^2 \widetilde{\Psi} - 2 \partial_x \widetilde{\Psi}, \\ \mathbf{N}(\widetilde{\Psi}) &= (\partial_x \widetilde{\Psi}) \partial_y \nabla^2 \widetilde{\Psi} - (\partial_y \widetilde{\Psi}) \partial_x \nabla^2 \widetilde{\Psi}. \end{cases} \tag{8}$$

The streamfunction appearing in Eq. (7) is spatially discretized within the computational domain $\Omega = \{(x, y) \in [0, \Lambda] \times [-1, 1]\}$ using a truncated *Fourier-Legendre* spectral approximation in the x-y coordinates, respectively, of the form

$$\widetilde{\Psi}_{LM}(x, y; t) = \sum_{\ell=-L}^{L} \sum_{m=0}^{M} a_{\ell m}(t) \Psi_{\ell m}(x, y), \tag{9}$$

where

$$\Psi_{\ell m}(x, y) = e^{i \ell k x} \Phi_m(y), \tag{10}$$

and

$$\Phi_m(y) = (1 - y^2)^2 \mathrm{L}_m(y), \tag{11}$$

with $\mathrm{L}_m(y)$ the m^{th} *Legendre* polynomial. In the Fourier-Legendre spectral expansion above, $k = 2\pi/\Lambda$ is the fundamental streamwise wave number. As a consequence $\widetilde{\Psi}_{LM}$ is Λ-periodic in the x-streamwise coordinate, that is,

$$\widetilde{\Psi}_{LM}(x + \Lambda, y; t) = \widetilde{\Psi}_{LM}(x, y; t) \qquad \forall x. \tag{12}$$

Since $\widetilde{\Psi}_{LM} \in \mathbb{R}$, the set of Fourier-Legendre coefficients $\mathbf{a} = \{a_{\ell m}\}$ satisfy $a_{-\ell m} = a^*_{\ell m}$, where $*$ denotes complex conjugation. In addition, the spectral expansion Eq. (9) identically satisfies the homogeneous Dirichlet-Neumann boundary conditions Eq. (6) since

$$\Phi_m(\pm 1) = \Phi'_m(\pm 1) = 0, \tag{13}$$

the prime expressing derivation with respect to the wall-normal coordinate d/dy. Further detail on the spatiotemporal numerical discretization of Eq. (7) may be found in Appendix A.

We have used the 2-norm of the expansion coefficients vector $\mathbf{a}$, as defined by

$$\|\mathbf{a}\| = \left[\sum_{\ell=-L}^{L} \sum_{m=0}^{M} |a_{\ell m}|^2 \right]^{1/2}, \tag{14}$$

to graphically represent the amplitude of solutions. Traveling wave solutions have a constant amplitude, while the instantaneous amplitude of time-dependent waves varies with time. In this latter case we have chosen to represent the maximum amplitude unless otherwise specified.

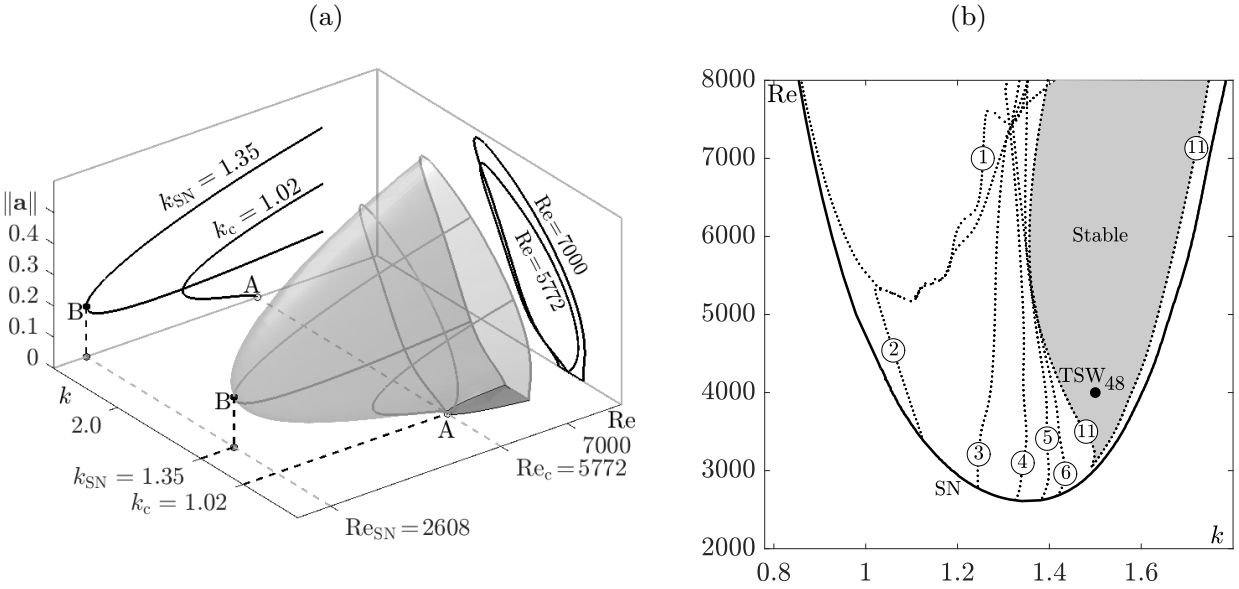

FIG. 1. (a) Tollmien-Schlichting waves (TSW) in parameter space for constant mass flow PPF. The projection depicts the norm $\|\mathbf{a}\|$ as a function of (k, Re). (b) Subharmonic linear stability analysis of upper-branch TSWs. The gray area denotes linear stability of TSWs to all infinitesimal perturbations, both super- (①) and subharmonic (ⓝ, $n > 1$).

III. SUB- AND SUPERHARMONIC BIFURCATIONS OF TOLLMIEN-SCHLICHTING WAVES

For sufficiently high Reynolds numbers, plane Poiseuille flow admits a multiplicity of solutions that coexist with the basic parabolic profile. The simplest such solutions arise directly from linear instability of the PPF base flow [29,30]. They are relative equilibria, i.e. rigid structures that travel in the streamwise direction, and go by the name of Tollmien-Schlichting waves (TSW for short) [31,32]. They are characterized by a clear-cut streamwise periodicity of wavelength $\lambda_0 = 2\pi/k_0$ (where k_0 is the fundamental wave number) and a traveling or *phase speed* c. For this particular type of solution, the Fourier coefficients in Eq. (9) read

$$a_{\ell m}(t) = a^{\mathrm{TW}}_{\ell m} e^{-i\ell k_0 c t}, \tag{15}$$

where $a^{\mathrm{TW}}_{\ell m}$ are time-independent Fourier-Legendre coefficients uniquely describing, except for an arbitrary initial phase, the wave solid-body structure. See Appendix B for a detailed descripton of the numerical methods employed in the computation and continuation of TSW.

Figure 1(a) shows a three-dimensional projection of the amplitude of TSWs, represented by the norm $\|\mathbf{a}\|$ introduced in Eq. (14), as a function of the streamwise wave number k and the Reynolds number Re. This figure is to be compared with Fig. 4 in Ref. [33] for the constant pressure gradient formulation of the problem. Since in the present formulation all solutions are represented by their departure from the reference PPF parabolic base flow, this latter is uniquely represented by the $\|\mathbf{a}\| = 0$ plane. The neutral stability curve of the PPF base flow is the parabola on this plane, whence the TSW family of solutions branches off. The minimum Reynolds number point on the linear stability curve (labeled A), sets the well-known critical pair $(k_{\mathrm{C}}, \mathrm{Re}_{\mathrm{C}}) = (1.02, 5772.22)$, first computed in [30] in 1971. The area bound by the neutral curve (dark gray shadowed region) delimits the region of parameter space where PPF is linearly unstable. The bifurcation of TSWs is subcritical [31] for a certain range of wave numbers around the critical k_{C}, as clearly visible from the shape of the surface, which extends towards Reynolds numbers lower than Re_{C}. The existence of TSWs reaches as low as $(k_{\mathrm{SN}}, \mathrm{Re}_{\mathrm{SN}}) \approx (1.35, 2608)$, where TSWs first arise at a saddle-node or fold bifurcation (labeled B). Subcriticality is remarkable in that $\mathrm{Re}_{\mathrm{SN}}$ is significantly lower than Re_{C}, and also well below its pressure-driven counterpart $\mathrm{Re}^{\mathrm{P}}_{\mathrm{SN}} \approx 2939.03$ as reported in former studies [33,34]. To guide the eye, Fig. 1(a) also depicts cross-sections of the three-dimensional surface

representing the TSWs family for a couple of Re and k values (gray curves on the TSW surface) along with corresponding orthogonal projections on the cartesian planes (black solid curves). In the subcritical region around the saddle-node point $(k_{\mathrm{SN}}, \mathrm{Re}_{\mathrm{SN}})$, two distinct TSW solutions simultaneously coexist with the base flow for the same values of the parameters. We call them the lower- and upper-branch solutions according to the compared value of their respective amplitudes. Lower-branch solutions are unstable, their unstable manifold pointing toward the base flow on one side and towards the upper-branch solution on the other. Upper-branch solutions are instead initially stable in a sufficiently close neighbourhood of the saddle-node point.

Numerous recent numerical studies have focused their attention on identifying spatially modulated waves that arise in open shear flows [15,24,25]. Linear stability analyzes of constant pressure-gradient and constant mass-flux PPF reveal that upper-branch TSWs typically exhibit *superharmonic* Hopf bifurcations for Re moderately larger than $\mathrm{Re}_{\mathrm{SN}}$ [14,27,34,35]. By superharmonic we mean that the TSW becomes unstable with respect to perturbations of their same wavelength or shorter. This instability leads to branches of locally *stable* time-*periodic* TSWs, hereafter called PTSW, that share wavelength with the TSW they bifurcate from. These coherent states are relative periodic orbits, since the emerged Hopf frequency bestows the wave a genuine time periodicity.

Systematic *subharmonic* linear stability analysis of PPF has been performed in the past [36] and more recently [14] in an attempt to cast light on streamwise localization mechanisms of propagating waves. The stability of a wave train consisting of n replicas of the same TSW (R_n) to perturbations of a wavelength that fits m times in the replicated domain is taken into consideration. See Appendix B for technical details on the numerical implementation of the Arnoldi stability analysis tool. Figure 1(b) shows the regions in (k, Re) parameter space where, according to Arnoldi linear stability analysis Eq. (B6), a TSW of wavelength $\lambda = 2\pi/k$ exhibits subharmonic Hopf bifurcations with respect to perturbations of wavelength $n\lambda$, considering all values of $n \in \mathbb{N}$ up to 11. The first superharmonic Hopf bifurcation occurs along the line labeled ① in Fig. 1(b), such that TSWs are superharmonically unstable beyond this line. A train consisting of two TSWs (R_2) becomes unstable to time-dependent perturbations to the left of curve ② which, simply put, means that the train R_2 is unstable in this region with respect to perturbations of length $\Lambda = 2\lambda_0$. The same goes for a train of three TSWs to the left of curve ③, and so on and so forth. The stability region of upper-branch TSWs shrinks as longer and longer perturbations are taken into consideration. However, the stability boundaries quickly saturate as n increases, such that very little progression is observed for $n > 11$ and beyond. Computations suggest that upper-branch TSWs may be linearly stable to all infinitesimal perturbations within a finite region of parameter space, liberally approximated here by the shaded area in Fig. 1(b). As a test, time-stepping at $\mathrm{Re} = 4000$ of a $k = 1.5$ TSW replicated $n = 48$ times (indicated by a bullet labeled TSW_{48}) within a domain of length $\Lambda \approx 200h$ did not result in destabilisation.

The subharmonic Hopf bifurcations described above were used by MM15 as the starting point for the study of localization mechanisms of waves in long domains. In the case of the Swift-Hohenberg amplitude equation, the mechanism underlying the appearance of localized steady states follows the homoclinic snaking scenario [37,38]. Homoclinic snaking has successfully provided an explanation for spanwise localization of exact solutions in doubly extended shear flows such as plane Couette flow [11,13]. However, snaking is not the only possible mechanism leading to spanwise localization. Alternative bifurcations, such as that exhibited by a spanwise-extended model of plane Couette flow [39], might also be at play. Homoclinic snaking, with modifications resulting from the broken Z_2 symmetry, was also explored by MM15 as a potential mechanism for localization in the streamwise direction. Parametric continuation of localized traveling waves in both Reynolds number and domain wavelength concluded that although a mechanism analogous to snaking was possible, it is structurally unstable and very sensitive to small changes in wavelength. In addition, no evidence was found of ladder solutions, a constituent ingredient of homoclinic snaking, or of connections to the equivalent of antisymmetric solutions, which cannot exist in a system that does not possess the required symmetry.

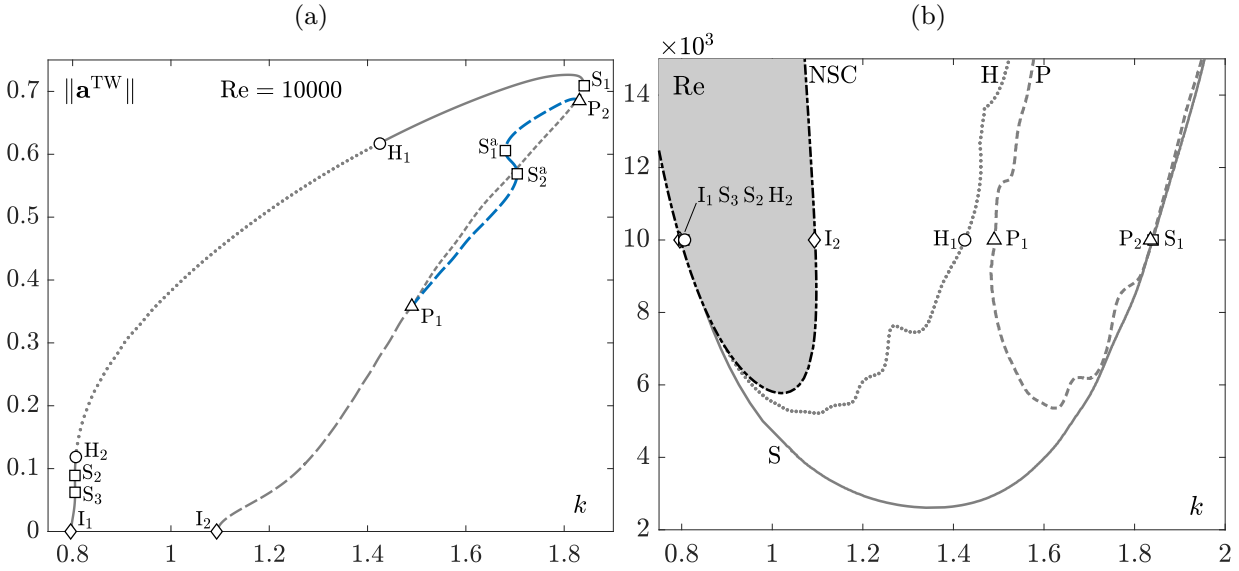

FIG. 2. (a) Pseudoarclength wavelength k-continuation of TSW (gray) and ATSW (blue) Tollmien-Schlichting waves for $\mathrm{Re} = 10^4$. Symbols indicate saddle-node (squares, S), Hopf (circles, H), and pitchfork (triangles, P) bifurcations. Also shown are the streamwise-invariance-breaking bifurcation points (diamonds, I) whence TSWs branch off the base flow. Line styles denote branches with different stability properties: stable (solid), one unstable complex pair (dotted), one unstable real (long-dashed) or two unstable real (short-dashed) eigenmodes. (b) Bifurcation diagram of TSWs. Shown are saddle-node (S, solid gray line), superharmonic Hopf (H, dotted) and pitchfork (P, dashed) bifurcation curves. The gray shaded area indicates the region where PPF is linearly unstable, bound by the neutral stability curve (NSC, I, dash-dotted).

IV. ASYMMETRIC TOLLMIEN-SCHLICHTING WAVES

All streamwise-periodic solutions in PPF known so far preserve a remnant of the original streamwise–wall-normal $SO(2) \times Z_2$ symmetry of the problem in the form of a half-wavelength-streamwise-shift and wall-normal-reflect symmetry,

$$\mathcal{S}\colon\ [u, -v; p](x + \pi/k, -y; t) = [u, v; p](x, y; t). \tag{16}$$

Solutions breaking this symmetry might well lead to alternative localization mechanisms biased to either one of the channel walls. We have set out to explore the eigenspectrum of $\mathcal{S}$-symmetric TSWs, obtained via Arnoldi linear stability analysis, in the search for $\mathcal{S}$-breaking pitchfork bifurcations. Eigenmodes have been systematically tracked and monitored for the TSW family of solutions throughout two-dimensional parameter space (k, Re). Figure 2(a) shows two such pitchfork bifurcations (P_1 and P_2, indicated with triangles) on a continuation curve of TSWs (gray line) at $\mathrm{Re} = 10^4$. At this Reynolds number, TSWs are linearly stable (solid) in three separate regions, respectively bounded by points S_1–H_1, H_2–S_2, and S_3–I_1. In between Hopf bifurcation points H_1 and H_2, TSWs possess one unstable complex pair (dotted) that leads to PTSWs as described by MM15. The branch sector delimited at either end by saddle-node points S_2 and S_3 is unstable with one positive real eigenvalue (long-dashed), as also are TSWs in the segments I_2–P_1 and P_2–S_1. The associated eigenmode is $\mathcal{S}$-preserving and the unstable manifold of these lower-branch TSWs lead either toward upper-branch TSWs to one side and either base flow or another upper-branch of TSWs to the other. TSWs incorporate a second positive real eigenvalue with $\mathcal{S}$-breaking associated eigenmode along the segment P_1–P_2 (short-dashed). The two pitchfork bifurcation points, which happen to be supercritical, are connected by a bridging branch of asymmetric TSWs, or ATSWs (blue line), that inherits the unstable real eigenmode from lower-branch TSWs. The presence of a pair of saddle-node bifurcations along the branch stabilizes the unstable eigenmode, if only briefly, thus leaving a small region of stability (solid) between S_1^a and S_2^a. The bifurcation points

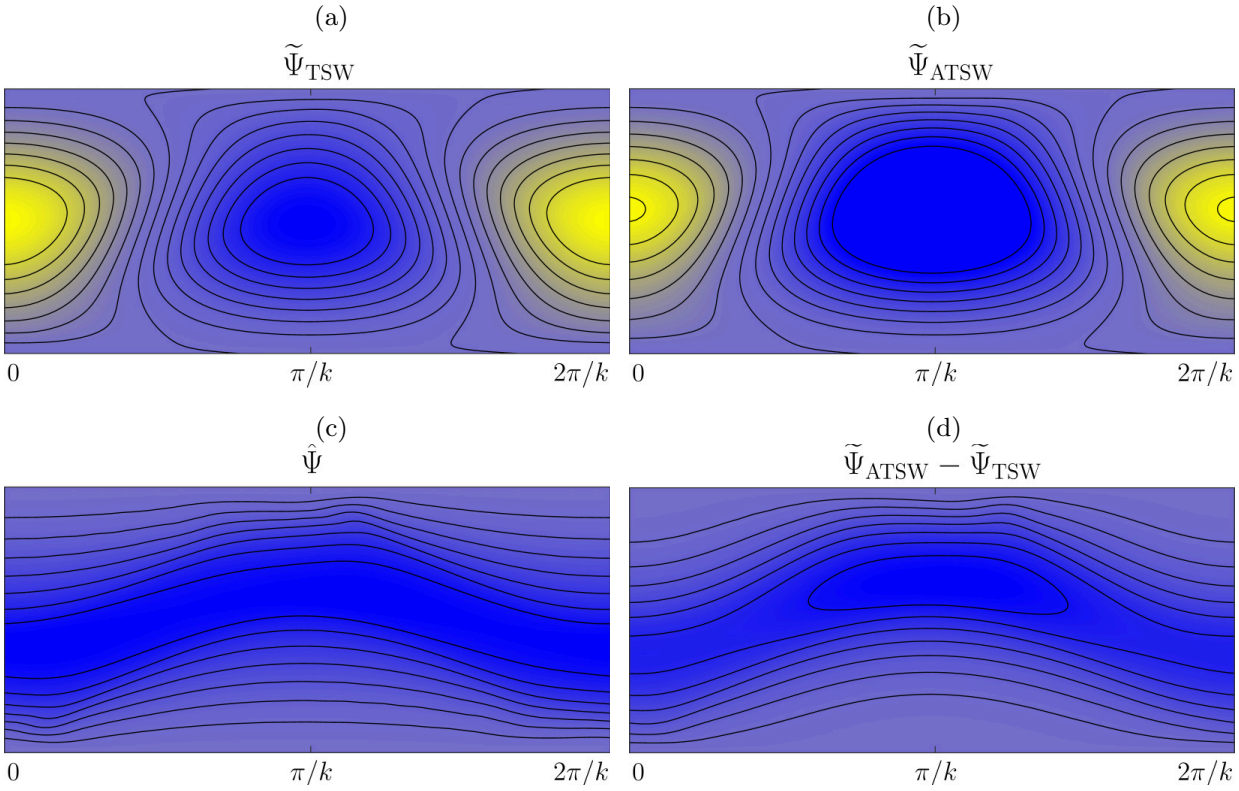

FIG. 3. Streamfunction perturbation $\tilde{\Psi}$ of traveling wave solutions in the vicinity of the pitchfork bifurcation point P_1 of Fig. 2 for $(k, \mathrm{Re}) = (1.7, 10^4)$. (a) TSW and (b) ATSW. Contour levels are equispaced in the interval $\tilde{\Psi} \in [-0.14, 0.14]$ with step $\Delta\tilde{\Psi} = 0.02$. (c) Bifurcating eigenmode $\hat{\Psi}$. (d) Difference $\tilde{\Psi}_{\mathrm{ATSW}} - \tilde{\Psi}_{\mathrm{TSW}}$ between TSW and ATSW.

of Fig. 2(a) unfold into bifurcation curves when tracked in (k, Re) parameter space. Figure 2(b) depicts the loci of pitchfork bifurcations of lower-branch TSWs (P, gray dashed line), along with the upper-branch Hopf [H, dotted, ① in Fig. 1(b)] and the saddle-node (S, solid) bifurcation curves. The lower-k portion of the saddle-node bifurcation curve has split in two by the time it reaches $\mathrm{Re} = 10000$, but this is barely noticeable in the figure. The pitchfork bifurcation curve reaches as low as $\mathrm{Re} \approx 5350 < \mathrm{Re}_c$ which renders ATSWs slightly subcritical in the sense that they coexist with the stable base flow, whose linear instability region is shaded with gray (bound by the neutral stability curve NSC—black solid—corresponding to an axial-invariance-breaking I of the base flow) in Fig. 2(b).

Figures 3(a) and 3(b) show streamfunction perturbation color maps of the lower-branch TSW and the ATSW, respectively, at $(k, \mathrm{Re}) = (1.7, 10^4)$, in a close neighbourhood of the pitchfork bifurcation point P_1. The color range has been set equispaced, symmetric and equal for both waves to adequately convey the effects of the $\mathcal{S}$-symmetry-breaking. In terms of streamfunction perturbation, the $\mathcal{S}$ symmetry reads

$$\mathcal{S}\colon\ \widetilde{\Psi}_{\mathrm{TSW}}(x, y; t) = -\widetilde{\Psi}_{\mathrm{TSW}}\left(x + \frac{\pi}{k}, -y; t\right), \tag{17}$$

so that $\mathcal{S}$-symmetric solutions change sign of $\tilde{\Psi}$ under a half-wavelength shift followed by reflection across the horizontal midplane. While the TSW clearly preserves the $\mathcal{S}$ symmetry, the ATSW has slightly but obviously disrupted it. The symmetry-breaking has been qualitatively assessed by subtracting one wave from the other in Fig. 3(d). Given that the waves are close to the bifurcation point, the difference between the two is closely aligned with the bifurcating eigenmode, which is shown in Fig. 3(c).

The effects of $\mathcal{S}$ on the Fourier-Legendre spectrum of solutions and eigenmodes allows straightforward detection of the symmetry. Formal substitution of the spectral expansion Eq. (9) into identity Eq. (17) leads to

$$\sum_{\ell,m}^{L,M} a_{\ell m} e^{i\ell kx} \Phi_m(y) = \sum_{\ell,m}^{L,M} (-1)^{\ell+m+1} a_{\ell m} e^{i\ell kx} \Phi_m(y), \tag{18}$$

where we have used the parity rule of Legendre polynomials $\mathrm{L}_m(-y) = (-1)^m \mathrm{L}_m(y)$. According to Eq. (18), nonvanishing Fourier-Legendre spectral coefficients corresponding to a TSW must have (ℓ, m) pairs satisfying the selection rule

$$\ell + m = 2n + 1, \tag{19}$$

for $n \in \mathbb{Z}$. The presence of the $\mathcal{S}$ symmetry can therefore be ascertained by verifying that all coefficients not following (19) vanish exactly.

Arnoldi stability analysis applied to the eigenproblem Eq. (B6) provides the unstable expansion-coefficients-*eigenvector* associated with the pitchfork bifurcation $\{\varepsilon_{\ell m}\}$. The corresponding *eigenmode* streamfunction perturbation fields are given by

$$\hat{\Psi}(x, y) = \sum_{\ell=-L}^{L} \sum_{m=0}^{M} \varepsilon_{\ell m} \Phi_m(y). \tag{20}$$

Eigenmodes breaking the $\mathcal{S}$ symmetry ought to be $\mathcal{S}$-antisymmetric

$$\mathcal{A}\colon\ \hat{\Psi}(x, y) = \hat{\Psi}\left(x + \frac{\pi}{k}, -y\right), \tag{21}$$

as a visual inspection of the eigenmode in Fig. 3(c) clearly illustrates. By virtue of Eq. (21), the eigenmode expansion Eq. (20) must satisfy

$$\sum_{\ell,m}^{L,M} \varepsilon_{\ell m} e^{i\ell kx} \Phi_m(y) = \sum_{\ell,m}^{L,M} (-1)^{\ell+m} \varepsilon_{\ell m} e^{i\ell kx} \Phi_m(y), \tag{22}$$

so that nonvanishing (ℓ, m) Fourier-Legendre pairs of an $\mathcal{S}$-symmetry-breaking eigenmode follow instead an *even* selection rule of the form

$$\ell + m = 2n, \tag{23}$$

with $n \in \mathbb{Z}$. All coefficients other than those in accordance with Eq. (23) must be identically zero. Selection rules Eqs. (19) and (23) have been confirmed numerically by direct examination of the sparsity structure of the coefficients $a_{\ell m}$ of TSWs and $\varepsilon_{\ell m}$ of $\mathcal{S}$-symmetry-breaking eigenmodes.

To clearly identify symmetry-broken solutions and to properly quantify the degree to which the symmetry has been disrupted we have defined an appropriate *symmetry parameter* as

$$S = \sum_{j=0}^{L-1} \omega(\Lambda j/L, 0), \tag{24}$$

where $\omega(x, 0)$ is the flow vorticity evaluated at any point $(x, 0)$ along the channel mid line $y = 0$. The parameter S is therefore obtained as the sum along the channel mid plane of the vorticity values at the equispaced Fourier streamwise nodes $x_j = \Lambda j/L$, for $j = 0, 1, \ldots, L-1$. Since a TSW respects the half-period-shift and reflect symmetry, vorticity exactly changes sign between two points on the center line located exactly half a wavelength apart, so that the sum along the center line yields $S = 0$. In the meantime, an ATSW breaks the symmetry, which leads to an imbalance between vortices in the upper and lower half of the domain that generally produces instead a net sum $S \neq 0$. As is the case for any pitchfork bifurcation, the ATSWs appear in conjugate-symmetric pairs, such that two solution branches exist simultaneously which are mutually related by the $\mathcal{S}$ symmetry.

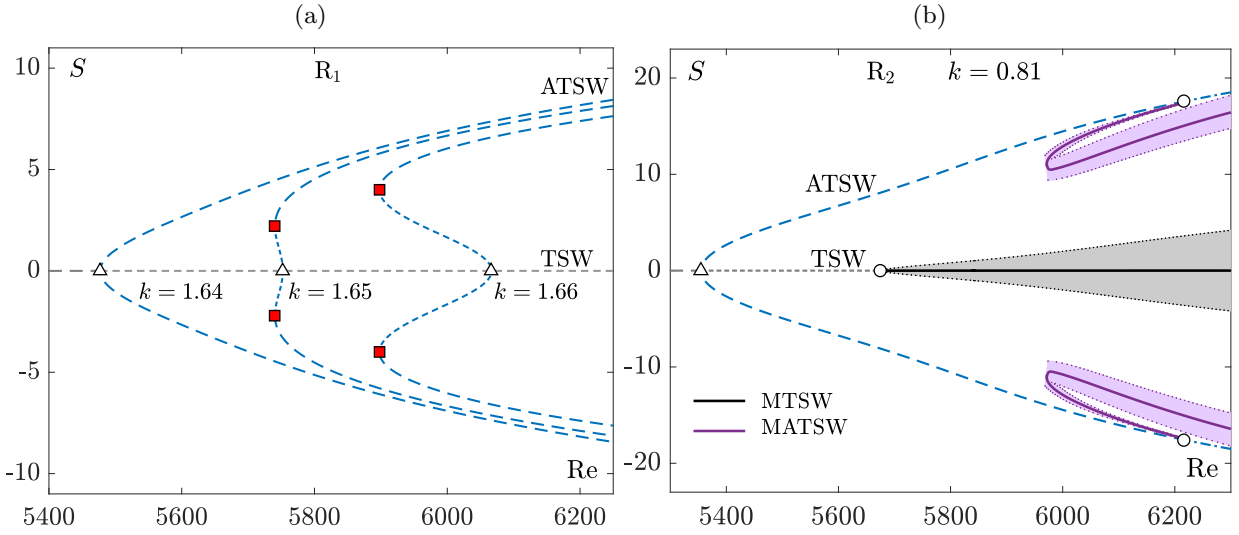

FIG. 4. Symmetry parameter S of TSW and ATSW solution branches as a function of Re for (a) small domains of fundamental wave number $k = 1.64$, 1.65, and 1.66 (see labels) fitting a single wavelength, and (b) a larger domain of wave number $k = 0.81$ accommodating an R_2-replicated wave. Symbols mark pitchfork (triangles), saddle-node [squares, red to indicate correspondence to the subcritical saddle-nodes in Fig. 5(a)] and subharmonic Hopf bifurcations (circles). TSW and ATSW linestyles as for Fig. 2. The time-average (solid line) and oscillation amplitude (delimited by the shaded region) of MTSWs (black) and MATSWs (violet) are also indicated.

The symmetry parameter S associated with the TSW and the bifurcated ATSW is represented in Fig. 4(a) as a function of the Reynolds number, for three different values of k. The pitchfork bifurcation (triangle) is supercritical for most k but becomes slightly *subcritical* within certain ranges of k. Nevertheless, the subcritical branches turn in a saddle-node bifurcation (red squares), such that they always finally extend towards increasing values of Re. Figure 5(a), which zooms in

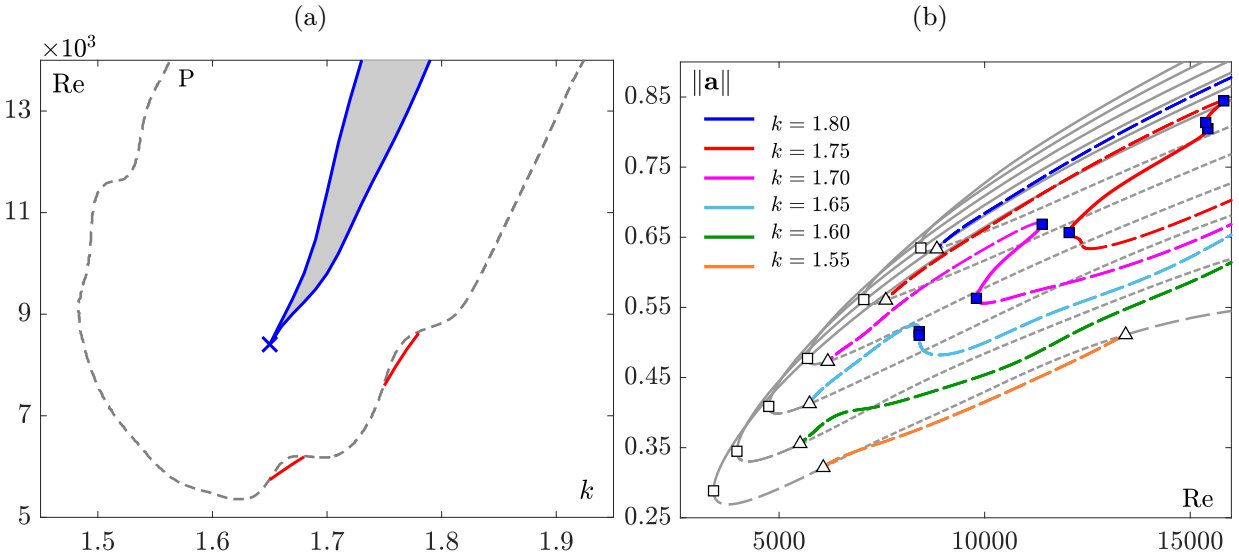

FIG. 5. (a) Lower-branch TSWs bifurcation diagram in (k, Re) parameter space. Shown are the pitchfork bifurcation curve for TSWs (dashed gray), the occasional saddle-node bifurcation curve of subcritical ATSWs (red) and the two saddle-node bifurcation curves of ATSWs (blue) that produce a region of linear stability (shaded area). The cross sign indicates a *cusp* bifurcation point at $(k, \mathrm{Re}) \simeq (1.65, 8406)$. (b) $\|\mathbf{a}\|$ of TSWs (gray lines) and ATSWs (color lines) as a function of Re and k. Line styles and symbols as for Fig. 2(a).

(k, Re) parameter space on the pitchfork bifurcation curve of Fig. 2(b), shows the loci of ATSWs saddle-node bifurcations (red line). There exist two separate parameter regions where ATSWs are subcritical, and then only very mildly.

All ATSWs identified in our explorations have been found to emerge from the lower branch of ordinary TSWs, and within a range of streamwise wave numbers k for which the latter do not bifurcate from the base Poiseuille flow. We have no explanation as to why all symmetry-breaking pitchfork bifurcations should occur on the lower branch of TSWs but, as it happens, upper branch solutions seem to require the onset of temporal chaos to fully disrupt the last remnants of the reflectional symmetry about the channel center-line. Figure 5(b) summarizes the comprehensive exploration performed in the present study by depicting the bifurcated ATSWs (color lines) emerging from the lower branch of TSWs (gray). The continuations have been performed for streamwise wave numbers ranging within the interval $k \in [1.55, 1.80]$. Although ATSWs are initially linearly unstable at bifurcation, they eventually—yet briefly—become *stable* at sufficiently large values of k and Re. As an example, the ATSW branch at $k = 1.7$ inherits the unstable real eigenvalue as it bifurcates supercritically from TSWs at Re ≈ 6430 (triangle). The branch becomes stable, however, in a saddle-node bifurcation (blue square) at Re ≈ 11388 and extends towards decreasing Reynolds number until undergoing a second saddle-node bifurcation at Re ≈ 9800 that destabilises it anew. From this point on, the branch progresses again, unstable, in the direction of increasing Reynolds numbers. The double saddle-node bounds a region in (k, Re) parameter space [gray shaded area in Fig. 5(a) bound by blue lines] where ATSWs are stable. The lowest Re at which stable ATSWs may be found is given by the cusp point (cross symbol) where the two saddle-node bifurcation curves (blue) intersect.

V. SPACE-MODULATED ASYMMETRIC TOLLMIEN-SCHLICHTING WAVES

Hopf bifurcations (super or subharmonic) of TSWs introduce a time-periodicity on top of the mere traveling motion. This modulation can be understood as a genuine periodic orbit on the comoving reference frame of the TSW. In this sense, the resulting Navier-Stokes solution is a time-*periodic* traveling wave (a *relative periodic orbit*). Solutions of this type are often unstable so they cannot be computed by simply time-stepping the system Eq. (A7) using the scheme Eq. (A8). These solutions can instead be computed and tracked in parameter space, regardless of their stability, by means of a Newton-Krylov-Poincaré method as that described in Appendix C.

The presence of subharmonic Hopf bifurcations on the lower branch of TSWs was already explored in detail by MM15. In some cases, this type of bifurcation leads to a time-periodic space-modulated Tollmien-Schlichting wave or MTSW that does not produce streamwise localization. Figure 4(b) shows a branch of MTSWs (black solid) bifurcated subharmonically in a domain with fundamental wave number $k = 0.81$ accommodating an R_2-replicated TSW. The MTSW clearly preserves, on average, the $\mathcal{S}$-symmetry as the identically zero value of the time-averaged S parameter (solid line) reveals. The amplitude of the oscillation (gray shaded region), though, clearly shows that the symmetry is instantaneously broken. As a matter of fact, the $\mathcal{S}$-symmetry is traded for an equivalent space-time symmetry that renders the solution invariant under half a period evolution followed by reflection about the mid plane and an appropriate streamwise shift. Wavelength continuation confirms that these solution branches are created and annihilated at either end without the incorporation (or suppression) of an additional TSW replica. This is illustrated in Fig. 6(a) for Re $= 8000$, where a branch of modulated solutions (solid black curve) connects the two subharmonic Hopf points H_{21} and H_{22} (circles) on the lower branch of a twice-replicated R_2 TSW branch. The role of these self-connecting nonlocalized modulated waves was not satisfactorily addressed by MM15. This will be the object of next section. Here we set out to clarify whether space-modulation may also arise from ATSWs and, if so, whether the resulting space-modulated ATSWs (MATSWs) may bear some connection with known MTSWs or evolve instead into localization following a different mechanism.

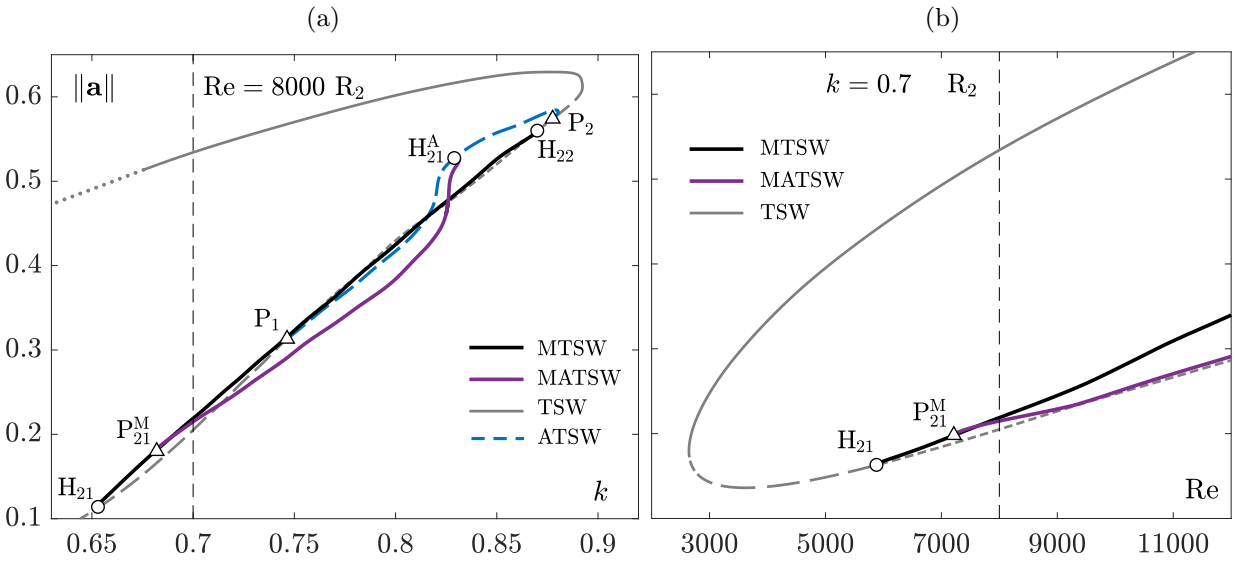

FIG. 6. (a) Wavelength k- (at Re = 8000) and (b) Re-continuation (at $k = 0.7$) of R_2-replicated TSWs. Shown are TSWs (gray lines) along with bifurcating ATSW (blue), MTSW (black) and MATSW (violet). Hopf (circles, H_{2i}) and pitchfork (triangles, P_{2i}) R_2-subharmonic bifurcation points are duly marked. Superscripts M and A denote bifurcation points on MTSW and ATSW branches, respectively. TSW linestyles as for Fig. 2.

Figure 4(b) shows how two mutually symmetric branches of MATSWs (violet) do indeed bifurcate from either branch of ATSWs at subcritical subharmonic Hopf points. In this case, both the time-averaged value of the S parameter (violet solid line) and the instantaneous value as expressed by the amplitude (pink shaded region) are different from zero, but the two separate branches are clearly symmetric to one another. We have performed a comprehensive subharmonic stability analysis along the continuation branches of ATSWs and found out that they also exhibit subharmonic Hopf bifurcations that generate branches of MATSWs, even in short domains fitting just two fundamental wavelengths of the ATSW. Figure 6(a) shows a wavelength continuation of an ATSW (blue line) bifurcated from lower-branch TSWs (gray line) at Re = 8000. The ATSW branch connects two pitchfork bifurcation points (P_1 and P_2, triangles) on the TSW branch. The branch undergoes a subharmonic Hopf bifurcation (H_{21}^A, circle), whence a new family of time-periodic space-modulated asymmetric waves MATSW (violet line) is issued. This MATSW branch is unstable, although stable MATSW have also been identified at much higher Reynolds numbers. Wavelength continuation of the MATSW branch reveals that it reconnects with the branch of MTSWs (black line), presumably at a pitchfork-of-cycles (P_{21}^M, triangle). Floquet-Arnoldi linear stability analysis of the Poincaré first return map Eq. (C1) corresponding to the relative periodic orbits associated with time-periodic waves has been employed to confirm the existence of this pitchfork bifurcation. Eigenvalues of the Poincaré map (Floquet exponents of the associated periodic orbit) have been accurately computed and monitored along the modulated solution branches. Analogous to the emergence of ATSWs from TSW, the Floquet stability analysis confirms that the MATSW branch is the result of a pitchfork bifurcation along the MTSW branch. Figure 6(b) shows the Reynolds continuation of both symmetric and asymmetric time-periodic modulated waves for $k = 0.7$. Within the explored range of parameters, the MATSW branch emerges always from a supercritical pitchfork bifurcation on the MTSW branch and does in no case reconnect with any other know solution branch. This is consistent with the exploration of ATSWs as summarized in Fig. 5(a), where these waves are shown nonexistent for $k < 1.48$ and Re < 14000. Consequently, since the MATSW solutions shown in Fig. 6(b) have $k = 0.7$, which corresponds to R_2-subharmonic bifurcation from an original ATSW with $k = 1.4$, reconnection cannot occur for this wavelength.

We have undertaken subharmonic stability analysis for R_3, R_4, and R_5 replicated ATSWs. Within the explored ranges of Reynolds numbers and wavelengths, we have not identified any remarkable

bifurcation qualitatively different from the one that is already observed for R_2. Floquet stability analysis of the bifurcated MATSWs has also been carried out in replicated domains. In this case, subharmonic bifurcations have only been detected for fourfold R_4-replicated MATSWs and beyond. Tracking MATSW branches in the long streamwise domains required for effective localization poses an insurmountable challenge to available numerical resources on account of the large amount of unstable eigenmodes present. Besides, the relevance of highly unstable waves, however localized, to actual flow dynamics is at the very least questionable on the same grounds.

VI. INTERACTIONS AMONG THE VARIOUS MTSW SOLUTION BRANCHES

In sufficiently long domains, stable localized time-periodic waves may exist in PPF for Reynolds numbers as low as Re = 2330 [40]. This type of solutions appear as a result of saddle-node bifurcations of relative periodic orbits upon increasing the Reynolds number, as parametric continuations by MM15 show [[14], Fig. 2(a)]. Upper-branch states are stable within the range Re $\in$ [2330, 2608], and are the only localized stable solutions of the two-dimensional Navier-Stokes equations in extended domains known to date. For Re $>$ 2608, and sufficiently long channels, localized solutions start interacting with the classical TSWs. As a matter of fact, upper-branch localized states ultimately originate from subharmonic Hopf bifurcations occurring along the superharmonically stable upper branch of R_n-replicated TSWs, for $n \geqslant 3$. Within the range of Reynolds numbers explored in MM15, continuation to larger domains of MTSWs emerging from upper-branch R_n TSWs results in three different branch types. For sufficiently low Re, the MTSW branch bifurcated from R_n extends to arbitrarily long domains as the solutions become strongly localized and exhibit exponential decay at both the trailing and leading fronts [26]. Coexisting with this branch at the same Re, another branch of MTSWs connects subharmonic Hopf bifurcations on the upper and lower branch of R_{n+1} TSWs. At somewhat higher Re, wavelength continuation of the MTSW branch bifurcated from upper-branch R_n TSWs results in the development of a wave defect, becomes unstable in a saddle-node, and eventually reconnects with the unstable lower branch of R_{n+1} TSWs having added a new wave replica along the way. This latter branch is in fact the result of a codimension-2 bifurcation of the former two solution branches. At the double-critical point, another branch of the localizing type, but this time starting from R_{n+1} upper-branch TSWs is created. At still higher Re and starting from long-wavelength subharmonic Hopf bifurcations, k-continuation of MTSWs occasionally produces exceedingly convoluted branches, so much so that neither extension to long domains nor reconnection to TSW branches has been found [[14], Fig. 4(a)]. The role and fate of these never-ending, intricate, MTSW branches remains an open question.

A completely different type of MTSW branch was also found by MM15 that uneventfully connects pairs of subharmonic Hopf bifurcation points on the higher-k end of the same branch of R_n-replicated TSWs. These other MTSW solutions did not seem to interact with any of the aforementioned MTSW branches, these latter all interrelated by the bicritical point and intimately associated to the streamwise localization mechanism under scrutiny, and where therefore deliberately overlooked by MM15.

We focus here on these seemingly unrelated MTSW branches and explore whether they may lead to a localization mechanism different from the one already described. We have systematically monitored all subharmonic bifurcations undergone by lower-branch TSWs and tracked the MTSW branches issued from them for increasing values of the Reynolds number. Figure 7(a) shows the two MTSW solution branches (black lines) emerged from the only two subharmonic Hopf bifurcations (circles, H_{41} and H_{42}) of lower-branch TSWs that exist in an R_4-replicated domain at Re = 3290. A few vorticity color maps of snapshots taken along the continuation branches (black circles with labels) have been represented in Fig. 7(b) for illustration purposes. The branch starting at the Hopf bifurcation H_{41} closely resembles an R_4 train of lower-branch TSWs at point A. By the time the branch reaches point Z_1, the spatial modulation is clear and a defect in the TSW pattern has emerged. The branch goes in a loop as the solution trades one TSW replica for a laminar gap (B) and finally extends to higher k progressively closing the gap through C to D, where something close to an R_3

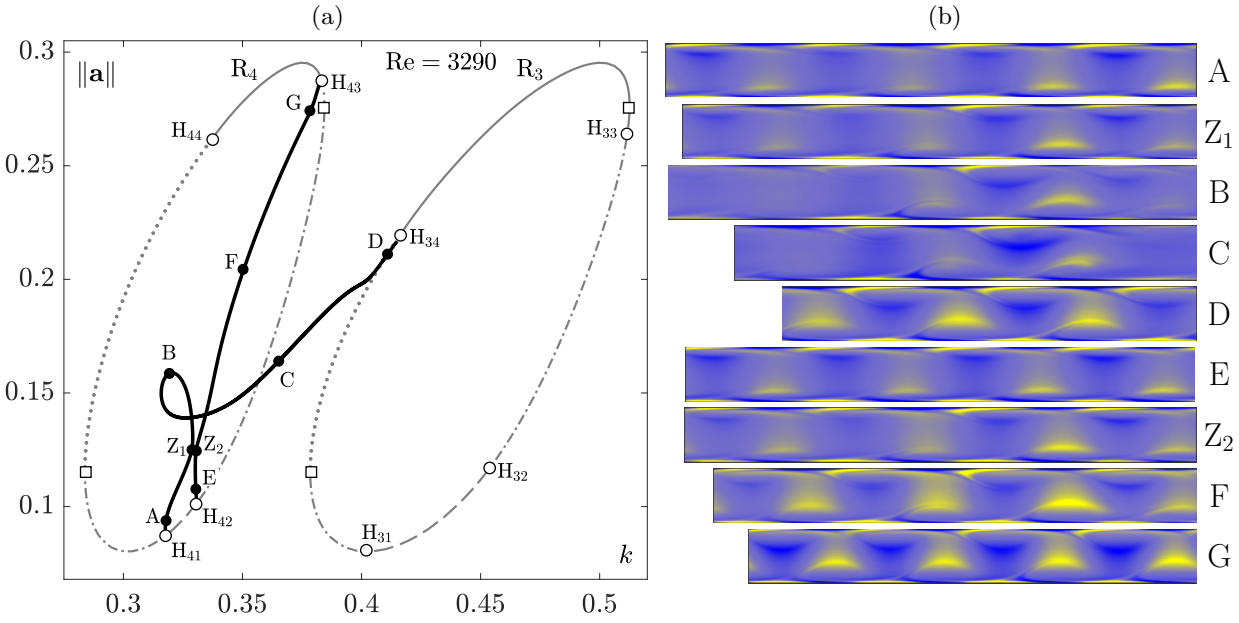

FIG. 7. MTSW branches (black lines) issued from R_4-subharmonic Hopf bifurcations of lower-branch TSWs (gray lines) at Re = 3290. (a) Amplitude $\|\mathbf{a}\|$ vs wave number k. Symbols denote saddle-node (squares) and Hopf (white circles, H_{4i}) bifurcations. Instability to one real and one complex pair of eigenmodes is indicated with a dash-dotted line. Rest TSW-related line styles as for Fig. 2. (b) Vorticity ω color maps of selected MTSW solutions duly marked (black circles) and labeled in (a).

TSW train fills the fundamental periodic domain before landing on the upper branch of TSWs at Hopf point H_{34}. Meanwhile, the MTSW family branching off TSWs at the Hopf point H_{42} is one of these hitherto apparently irrelevant branches uneventfully bridging subharmonic Hopf bifurcations on the same R_n-replicated TSW branch, this time ending at Hopf point H_{43}. Vorticity color maps show a barely imperceptibly imperfect R_4 train of lower-branch TSWs close to H_{42} at point E. The solution has clearly developed a defect by the time it reaches point Z_2 that persists through point F but is later gradually attenuated until recovering the R_4 train of—this time upper-branch—TSWs at point G, close to H_{43}.

The two branches get very close to one another in the two-dimensional projection of Fig. 7(a), the closest approach corresponding to points Z_1 and Z_2 on either continuation curve. The possibility that the apparent close approach is an artifact of the low-dimensional projection cannot be discarded altogether, but the hypothesis is clearly supported by the virtually identical, to the bare eye, Z_1 and Z_2 vorticity color maps in Fig. 7(b).

As a matter of fact, tracking the two families of MTSW solutions to slightly higher Re entails a completely different layout of the continuation branches that can only be explained through a codimension-2 bifurcation. Figure 8(a) depicts the arrangement of MTSW branches at Re = 3300. Both branches seem to have split in two at approximately Z_1 and Z_2, respectively, and each of the two resulting segments of each original branch have been glued at Z_3 and Z_4 to the homologous portion of the other branch. In this way, two new cross-branches, one joining Hopf points H_{41} and H_{42} and the other linking H_{43} and H_{34}, have emerged. The labeled points on Fig. 8(b) are indistinguishable from the analogous points in Fig. 7(b) and the snapshots corresponding to Z_i, $i = \{1, 2, 3, 4\}$ represent perturbations of a bicritical point at $(\mathrm{Re}, k) \in ([3290, 3300], [0.329, 0.330])$.

To better pinpoint the location of the bicritical point at which the two families of MTSWs connect, Fig. 9 shows a detailed continuation of solution branches within the interval $3280 \leqslant \mathrm{Re} \leqslant 3300$, in the immediate neighbourhood of the pinch point Z. From $\mathrm{Re} \gtrsim 3295$ on, purely upper-branch MTSWs exist in the sense that they are issued at either end from subharmonic Hopf points of upper-branch TSWs. This renders them good candidates as structural constituents of the strange

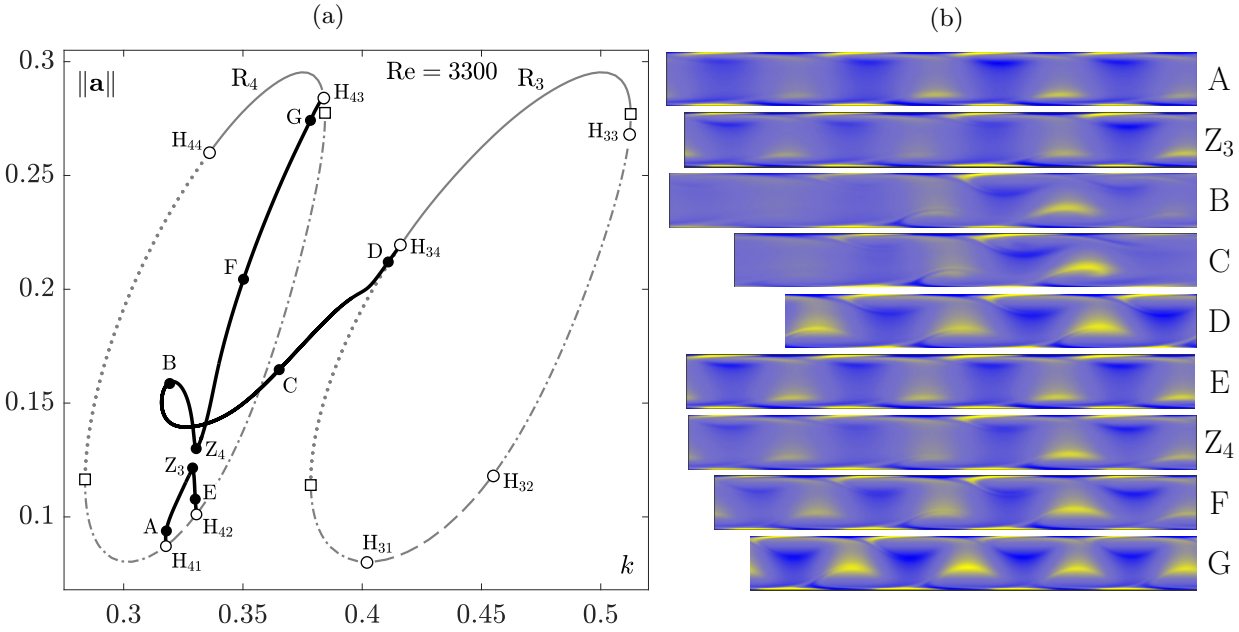

FIG. 8. MTSW branches issued from R_4-subharmonic Hopf bifurcations of lower-branch TSWs at Re = 3300. (a) Amplitude $\|\mathbf{a}\|$ vs. wave number k. (b) Vorticity ω color maps of selected MTSW solutions. Symbols and line styles as for Fig. 7.

saddle that governs domain-filling turbulent dynamics at sufficiently high Reynolds numbers. As such, the drifting gap that characterizes them may be responsible for the wave dislocations that are typical of turbulent channel flow.

VII. CONCLUSIONS

We have addressed in this study various unexplored aspects of symmetry-breaking and streamwise modulation of propagating waves in plane Poiseuille flow. Comprehensive linear stability analysis along the upper and lower branches of TSWs has allowed identification of pitchfork bifurcations that lead to a new family of ATSW solutions that break the classical half-shift and reflect equivariance. These new coherent states emerge from the unstable lower branch of TSWs at subcritical Reynolds numbers. Parametric continuation in Reynolds number Re and in streamwise

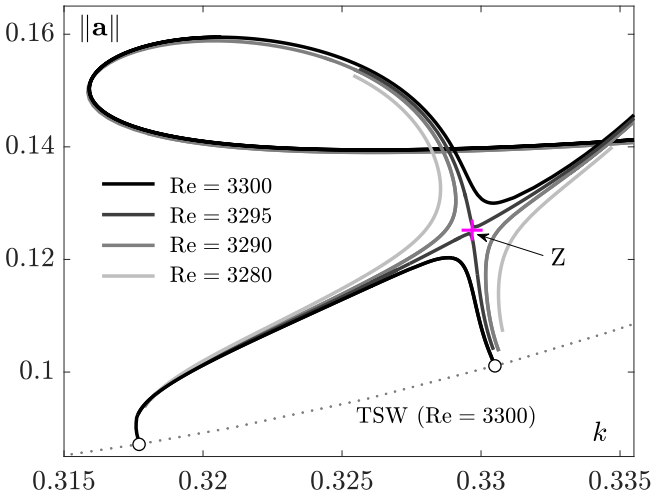

FIG. 9. Detail of codimension-2 bifurcation point Z (pink plus sign) relating all know types of MTSWs.

wave number k confirm that these ATSWs become linearly stable within some regions of parameter space. A subharmonic Arnoldi stability analysis of the new ATSW solutions has revealed that these waves exhibit Hopf bifurcations that lead to space-modulation. The resulting time-periodic streamwise-modulated asymmetric waves (MATSW) have also been continued in parameter space, although no streamwise localization has been identified within the (k, Re)-range explored. They have been shown, instead, to branch off already known MTSWs bifurcated subharmonically from TSWs. While MTSWs break the TSW shift and reflect symmetry at any given time but preserve it in the form of a space-time symmetry (they are invariant under evolution over half a period followed by a reflection about the midplane and an appropriate streamwise shift), MATSWs have completely broken all remnants of the reflection symmetry about the channel midplane. A thorough scrutiny of the potential relevance of ATSWs (and MATSWs) to the fully three-dimensional channel flow problem is far beyond the scope of the present study, yet worthwhile of a detailed exploration in future work. It is only through the disrupture of all prevailing reflectional symmetry about the channel midplane that solutions may experience a bias towards one of the walls, thereby bearing the potential for casting some light on near-wall structures observed in wall-bounded turbulent shear flows.

We have also tracked in our analysis MTSW branches emanating from lower branch TSWs through subharmonic Hopf bifurcation in the search for alternative mechanisms of streamwise localization of traveling waves. Although no such new mechanism has been found, we have shown that these solutions are in fact related to an already known family of localizing MTSWs through the occurrence of a codimension-two bifurcation point. Following this bifurcation, MTSWs exclusively interconnecting subharmonic Hopf points of upper-branch TSWs arise. These purely upper-branch solutions hold a potential for enacting wave dislocations within the strange saddle upon which domain-filling turbulent dynamics are sustained at high Reynolds numbers.

ACKNOWLEDGMENTS

This research was supported by the Spanish MINECO Grants No. FIS2016-77849-R and No. FIS2017-85794-P and the Generalitat de Catalunya Grant No. 2017-SGR-785.

APPENDIX A: NUMERICAL DISCRETIZATION

The Galerkin formulation of the problem consists in formally substituting expansion Eq. (9) in Eq. (7) and projecting back onto the set of Fourier-Legendre functions Eq. (10) by means of the hermitian inner product between two arbitrary fields $F(x, y)$ and $G(x, y)$ defined within the domain $\Omega = [0, \Lambda] \times [-1, 1]$ by

$$(F, G)_\Omega \doteq \int_0^\Lambda \int_{-1}^1 F^* G \, dy \, dx. \tag{A1}$$

This inner product is numerically approximated using spectrally accurate de-aliased fast Fourier transform in the streamwise direction x, along with Gauss-Legendre quadrature formulas in the wall-normal coordinate y. The aforementioned projection is therefore

$$(\Psi_{pq}, \partial_t \nabla^2 \widetilde{\Psi}_{LM})_\Omega = [\Psi_{pq}, \mathbf{L}_{\mathrm{Re}}(\widetilde{\Psi}_{LM}) + \mathbf{N}(\widetilde{\Psi}_{LM})]_\Omega, \tag{A2}$$

for $0 \leqslant p \leqslant L$ and $0 \leqslant q \leqslant M$, which leads to a system of nonlinear ordinary differential equations for the Fourier-Legendre coefficients of the form

$$\mathbb{A}^{\ell m}_{pq} \dot{a}_{\ell m} = \mathbb{B}^{\ell m}_{pq} a_{\ell m} + \mathbb{N}(\mathbf{a}), \tag{A3}$$

where we have used the convention of summation with respect to repeated indices, the dot in $\dot{a}_{\ell m}$ denotes a time derivative, and $\mathbb{A}^{\ell m}_{pq}$, $\mathbb{B}^{\ell m}_{pq}$ and $\mathbb{N}_{pq}$ are the inner products

$$\mathbb{A}^{\ell m}_{pq} = (\Psi_{pq}, \nabla^2 \Psi_{\ell m})_\Omega, \tag{A4}$$

$$\mathbb{B}^{\ell m}_{pq} = [\Psi_{pq}, \mathbf{L}_{\mathrm{Re}}(\Psi_{\ell m})]_\Omega, \tag{A5}$$

$$\mathbb{N}_{pq} = [\Psi_{pq}, \mathbf{N}(\widetilde{\Psi}_{LM})]_\Omega, \tag{A6}$$

for $0 \leqslant p, l \leqslant L$ and $0 \leqslant q, m \leqslant M$. The inner product in Eq. (A6) is evaluated pseudospectrally using a de-aliased grid in the streamwise direction. For simplicity, we write Eq. (A3) as

$$\mathbb{A}\dot{\mathbf{a}} = \mathbb{B}\mathbf{a} + \mathbb{N}(\mathbf{a}). \tag{A7}$$

Equation (A7) constitutes an $(L+1)\times(M+1)$-dimensional nonlinear dynamical system for the Fourier-Legendre amplitudes of the disturbance. The time integration is carried out using a fourth-order IMEX method (BDF4 backward-differences linearly implicit method for the linear biharmonic term and fourth-order explicit extrapolation of the nonlinear term) with associated linear multistep formula

$$\begin{aligned}(25\mathbb{A} - 12\Delta t\mathbb{B})\mathbf{a}^{(j+1)} &\\ = \mathbb{A}(48\mathbf{a}^{(j)} - 36\mathbf{a}^{(j-1)} + 16\mathbf{a}^{(j-2)} - 3\mathbf{a}^{(j-3)}) &\\ + \Delta t(48\mathbb{N}^{(j)} - 72\mathbb{N}^{(j-1)} + 48\mathbb{N}^{(j-2)} - 12\mathbb{N}^{(j-3)}),&\end{aligned} \tag{A8}$$

duly initialized by means of a fourth-order Runge-Kutta method.

A time step $\Delta t = 10^{-2}$ has been found to provide sufficient accuracy for the most numerically demanding integrations herein and therefore used throughout all parametric explorations. For the spatial discretization, a minimum of $M = 50$ Legendre polynomials along with $L = 19 \times n$ Fourier modes (n is the number of Tollmien-Schlichting waves that can be fitted in the periodic domain) in the wall-normal and streamwise directions have been used, respectively. Neither increasing the wall-normal or streamwise spatial resolutions nor decreasing the time-step has resulted in any quantitatively significant impact on the dynamical properties of any of the flow regimes studied in this work.

APPENDIX B: COMPUTATION AND STABILITY ANALYSIS OF TRAVELING WAVES

After introducing Eq. (15) in Eq. (9), the Galerkin projection Eq. (A2) leads to a time-independent nonlinear algebraic system of equations for the unknown speed c and complex state vector $\mathbf{a}^{\mathrm{TW}} = \{a^{\mathrm{TW}}_{\ell m}\}$

$$\left(\mathbb{B}^{\ell m}_{pq} + ik_0\ell c\mathbb{A}^{\ell m}_{pq}\right)a^{\mathrm{TW}}_{\ell m} + \mathbb{N}_{pq}(\mathbf{a}^{\mathrm{TW}}) = 0, \tag{B1}$$

for $0 \leqslant p \leqslant L$ and $0 \leqslant q \leqslant M$. System Eq. (B1) must be completed with an extra condition on the phase of the solution to remove streamwise degeneracy, leading to an algebraic system of nonlinear equations that we simply write as

$$\mathbf{F}(\mathbf{a}^{\mathrm{TW}}, c; \mathrm{Re}, k_0) = \mathbf{0}. \tag{B2}$$

The previous system implicitly determines the sought-after coefficient vector $\mathbf{a}^{\mathrm{TW}}$ of the wave and its corresponding traveling speed c as functions of the two parameters, namely, the Reynolds number Re and the streamwise periodic length $\Lambda = 2\pi/k_0$ of the computational domain as dictated by the fundamental wave number k_0, that is

$$\mathbf{a}^{\mathrm{TW}} = \mathbf{a}^{\mathrm{TW}}(\mathrm{Re}, k_0), \quad c = c(\mathrm{Re}, k_0). \tag{B3}$$

We solve Eq. (B2) by means of *Jacobian-free* Newton-Krylov methods [41] and track solution branches through (Re, k_0) parameter space using pseudoarclength continuation schemes [42].

A spatially periodic traveling wave may become unstable through many different mechanisms. If the wave preserves some symmetry of the PPF problem, a steady pitchfork bifurcation in the moving reference frame of the wave may lead to symmetry-conjugate traveling-wave solution

branches that break the symmetry. Alternatively, a Hopf bifurcation, be it symmetry-breaking or symmetry-preserving, may introduce a time-periodic modulation of the wave amplitude. Spatially periodic waves may become unstable to perturbations of their same wavelength following a so-called *superharmonic* bifurcation, but perturbations of wavelengths longer than that of the original wave must also be considered in general, as instabilities can also be spatially *modulational* as a result of a *subharmonic* instability.

In the most general case, the linear stability analysis of a traveling-wave solution of wavelength $\lambda_0 = 2\pi/k_0$ must consider infinitesimal perturbations of wavelength $\lambda = 2\pi/k$, where in principle k can take any positive real value in the interval $[0, k_0]$. For $k/k_0 = m/n, n \in \mathbb{N}$ and $m = 1, ..., n$, the instability of a traveling wave of wave number k_0 can be understood as the superharmonic instability of a train of n replicas of the traveling wave (R_n), filling a periodic domain of length $\Lambda = n\lambda_0$, to periodic perturbations that fit m times in the domain [43,44]. Floquet theory analysis shows that modes with $m = j$ and $m = n - j$ are related by conjugation, so that only half the possible wavelengths need to be explored. Furthermore, an analysis for a given k/k_0 can be performed on the minimal domain nk_0, such that n/m expresses an irreducible fraction. Instability to irrational k/k_0 can only be interpreted in an infinitely long domain.

The representation of $a^{\mathrm{TW}}_{\ell' m}$ in the n-fold replicated domain $\Omega_n = [-1, 1] \times [0, n\lambda_0],\ n \in \mathbb{N}$ is given by

$$a_{\ell m}(t) = a^{\mathrm{TW}_n}_{\ell m} e^{-i\ell k_n c t}, \tag{B4}$$

where $k_n = k_0/n$ and $a^{\mathrm{TW}_n}_{\ell m} = a^{\mathrm{TW}}_{\ell' m}$ for $\ell = n\ell'$ and 0 otherwise. Linear stability is then analyzed by considering infinitesimal disturbances to the traveling wave:

$$a_{\ell m}(t) = \left(a^{\mathrm{TW}_n}_{\ell m} + \varepsilon_{\ell m} e^{\sigma t}\right) e^{-i\ell k_n c t}. \tag{B5}$$

Substituting Eq. (B5) in Eq. (A3) and neglecting $O(\varepsilon^2_{\ell m})$ terms leads to a generalized eigenvalue problem of the form

$$(\sigma - ik_n \ell\, c)\mathbb{A}^{\ell m}_{pq}\varepsilon_{\ell m} = \mathbb{B}^{\ell m}_{pq}\varepsilon_{\ell m} + D_{\mathbf{a}}\mathbb{N}^{\ell m}_{pq}(\mathbf{a}^{\mathrm{TW}_n})\varepsilon_{\ell m}, \tag{B6}$$

where $D_{\mathbf{a}}\mathbb{N}^{\ell m}_{pq}(\mathbf{a}^{\mathrm{TW}_n})$ is the linearization of $\mathbb{N}$ in a neighbourhood of $\mathbf{a}^{\mathrm{TW}_n}$ and $(p, q) = [0, nL] \times [0, M]$. For small or moderate values of n, the spectrum of eigenvalues $\sigma^{(j)}$ and associated eigenvectors $\boldsymbol{\varepsilon}^{(j)} = \{\varepsilon^{(j)}_{\ell m}\}$ can be solved using direct eigenvalue methods such as QZ. However, for large values of n, producing the full spectrum becomes unfeasible. As a matter of fact, the computation of the whole spectrum is generally unnecessary, as only the largest real part (leading) eigenvalues need to be monitored to identify potential bifurcations. Then, Arnoldi iteration combined with suitable Cayley transformations in the complex plane can be employed instead [45]. A comprehensive subharmonic linear stability analysis to all possible perturbation wavelengths would still incur unaffordable computational time-scales. Following MM15, we have limited the exploration to a range of wave numbers k that can be analysed in domains of length up to $11\lambda_0$. This streamwise periodic domain is sufficiently long to initiate a streamwise modulation that effectively localizes when continued to longer domains.

APPENDIX C: COMPUTATION OF TIME-PERIODIC TRAVELING WAVES

To accurately compute time-periodic traveling-wave solutions (PTW) to any desired accuracy, we look for *fixed points* of the *Poincaré map* $\mathbb{P}$,

$$\mathbf{a} \mapsto \tilde{\mathbf{a}} = \mathbb{P}(\mathbf{a}) = \mathbb{T}(\Delta x)\, \Phi^T(\mathbf{a}), \tag{C1}$$

where Φ^t is the *flow* generated by Eq. (A7) and

$$[\mathbb{T}(\Delta x)\mathbf{a}]_{\ell m} = e^{-i\ell k \Delta x} a_{\ell m} \tag{C2}$$

is the streamwise-shift operator that deals with the degeneracy in the x coordinate. The time-period T of the orbit and the streamwise drift Δx must satisfy

$$\begin{array}{rcl} [\mathbb{P}(\mathbf{a}) - \mathbf{a}] \cdot \widehat{\mathbb{T}}(\mathbf{a}) & = & 0, \\ [\mathbb{P}(\mathbf{a}) - \mathbf{a}] \cdot \dot{\mathbf{a}} & = & 0, \end{array} \tag{C3}$$

where

$$[\widehat{\mathbb{T}}(\mathbf{a})]_{\ell m} = -i\ell k a_{\ell m} \tag{C4}$$

is the group orbit tangent and

$$\dot{\mathbf{a}} = \mathbb{A}^{-1}[\mathbb{B}\mathbf{a} + \mathbb{N}(\mathbf{a})] \tag{C5}$$

is the rate of change of the state vector. The orthogonality conditions Eq. (C3) simultaneously define the Poincaré section and remove the drift degeneracy along the group orbit. Once this degeneracy has been removed, a time-periodic traveling wave $\mathbf{a}^{\mathrm{PTW}}$ is a fixed point of the Poincaré map Eq. (C1) or, equivalently, a solution to

$$\mathbb{P}(\mathbf{a}^{\mathrm{PTW}}, T; \mathrm{Re}, k_0) - \mathbf{a}^{\mathrm{PTW}} = 0, \tag{C6}$$

where the map $\mathbb{P}$ depends on Re and k_0 through the operator $\mathbb{B}$ involved in Φ^t through the time integration of Eq. (A7). Nonlinear system Eq. (C6) implicitly determines the sought PTW and its period as implicit functions of Re and k_0, that is

$$\mathbf{a}^{\mathrm{PTW}} = \mathbf{a}^{\mathrm{PTW}}(\mathrm{Re}, k_0), \quad T = T(\mathrm{Re}, k_0). \tag{C7}$$

We solve system Eq. (C6) by means of a Newton-Krylov-Poincaré method already successfully applied by MM15. Branches of PTWs can then be tracked in the (Re, k_0) parameter space using pseudoarclength continuation schemes.

[1] P. J. Schmid and D. Henningson, *Stability and Transition in Shear Flows* (Springer, Berlin, 2001).

[2] L. S. Tuckerman, M. Chantry, and D. Barkley, Patterns in wall-bounded shear flows, Ann. Rev. Fluid Mech. **52**, 343 (2020).

[3] V. Romanov, Stability of plane-parallel Couette flow, Funct. Anal. Its Appl. **7**, 137 (1973).

[4] A. Meseguer and L. N. Trefethen, Linearized pipe flow to Reynolds number 10^7, J. Comput. Phys. **186**, 178 (2003).

[5] B. Hof, C. W. H. van Doorne, J. Westerweel, N. F. T. M., H. Holger Faisst, B. Eckhardt, H. Wedin, R. R. Kerswell, and F. Waleffe, Experimental observation of nonlinear traveling waves in turbulent pipe flow, Science **305**, 1594 (2004).

[6] H. Faisst and B. Eckhardt, Transition from the Couette-Taylor system to the plane Couette system, Phys. Rev. E **61**, 7227 (2000).

[7] H. Wedin and R. R. Kerswell, Exact coherent structures in pipe flow: Traveling wave solutions, J. Fluid Mech. **508**, 333 (2004).

[8] F. Mellibovsky and A. Meseguer, Critical threshold in pipe flow transition, Phil. Trans. Roy. Soc. Lond. A **367**, 449 (2009).

[9] M. Nagata, Three-dimensional finite-amplitude solutions in plane Couette flow: Bifurcation from infinity, J. Fluid Mech. **217**, 519 (1990).

[10] D. Viswanath, Recurrent motions within plane Couette turbulence, J. Fluid Mech. **580**, 339 (2007).

[11] T. Schneider, J. Gibson, and J. Burke, Snakes and Ladders: Localized Solutions of Plane Couette Flow, Phys. Rev. Lett. **104**, 104501 (2010).

[12] T. Kreilos and B. Eckhardt, Periodic orbits near onset of chaos in plane Couette flow, Chaos **22**, 047505 (2012).

[13] J. F. Gibson and T. M. Schneider, Homoclinic snaking in plane Couette flow: Bending, skewing and finite-size effects, J. Fluid Mech. **794**, 530 (2016).

[14] F. Mellibovsky and A. Meseguer, A mechanism for streamwise localisation of nonlinear waves in shear flows, J. Fluid Mech. **779**, R1 (2015).
[15] S. Zammert and B. Eckhardt, Streamwise and doubly localised periodic orbits in plane Poiseuille flow, J. Fluid Mech. **761**, 348 (2014).
[16] K. Avila, D. Moxey, A. de Lozar, M. Avila, D. Barkley, and B. Hof, The onset of turbulence in pipe flow, Science **333**, 192 (2011).
[17] D. Borrero-Echeverry, M. F. Schatz, and R. Tagg, Transient turbulence in Taylor-Couette flow, Phys. Rev. E **81**, 025301 (2010).
[18] P. Ritter, F. Mellibovsky, and M. Avila, Emergence of spatiotemporal dynamics from exact coherent solutions in pipe flow, New J. Phys. **18**, 083031 (2016).
[19] D. Barkley and L. S. Tuckerman, Computational Study of Turbulent Laminar Patterns in Couette Flow, Phys. Rev. Lett. **94**, 014502 (2005).
[20] A. Meseguer, F. Mellibovsky, M. Avila, and F. Marques, Instability mechanisms and transition scenarios of spiral turbulence in Taylor-Couette flow, Phys. Rev. E **80**, 046315 (2009).
[21] D. Samanta, A. de Lozar, and B. Hof, Experimental investigation of laminar turbulent intermittency in pipe flow, J. Fluid Mech. **681**, 193 (2011).
[22] F. Dauchot and O. Daviaud, Finite amplitude perturbation and spots growth mechanism in plane Couette flow, Phys. Fluids **7**, 335 (1995).
[23] F. Mellibovsky, A. Meseguer, T. M. Schneider, and B. Eckhardt, Transition in Localized Pipe Flow Turbulence, Phys. Rev. Lett. **103**, 054502 (2009).
[24] M. Avila, F. Mellibovsky, N. Roland, and B. Hof, Streamwise-Localized Solutions at the Onset of Turbulence in Pipe Flow, Phys. Rev. Lett. **110**, 224502 (2013).
[25] M. Chantry, A. Willis, and R. R. Kerswell, Genesis of Streamwise-Localized Solutions from Globally Periodic Traveling Waves in Pipe Flow, Phys. Rev. Lett. **112**, 164501 (2014).
[26] J. Barnett, D. R. Gurevich, and R. O. Grigoriev, Streamwise localization of traveling wave solutions in channel flow, Phys. Rev. E **95**, 033124 (2017).
[27] J. Pugh and P. Saffman, Two-dimensional superharmonic stability of finite-amplitude waves in plane Poiseuille flow, J. Fluid Mech. **194**, 295 (1988).
[28] B. Hof, A. Juel, and T. Mullin, Scaling of the Turbulence Transition Threshold in a Pipe, Phys. Rev. Lett. **91**, 244502 (2003).
[29] L. H. Thomas, The stability of plane Poiseuille flow, Phys. Rev. **91**, 780 (1953).
[30] S. A. Orszag, Numerical simulation of incompressible flows within simple boundaries: Accuracy, J. Fluid Mech. **49**, 75 (1971).
[31] T. S. Chen and D. D. Joseph, Subcritical bifurcation of plane Poiseuille flow, J. Fluid Mech. **58**, 337 (1973).
[32] J. P. Zahn, J. Toomre, E. Spiegel, and D. Gough, Nonlinear cellular motions in Poiseuille channel flow, J. Fluid Mech. **64**, 319 (1974).
[33] U. Ehrenstein and W. Koch, Three-dimensional wavelike equilibrium states in plane Poiseuille flow, J. Fluid Mech. **228**, 111 (1991).
[34] P. Casas and A. Jorba, Hopf bifurcations to quasiperiodic solutions for the two-dimensional plane Poiseuille flow, Commun. Nonlinear Sci. Num. Simul. **17**, 2864 (2012).
[35] I. Soibelman and D. I. Meiron, Finite-amplitude bifurcations in plane Poiseuille flow: Two-dimensional Hopf bifurcation, J. Fluid Mech. **229**, 389 (1991).
[36] A. Drissi, M. Net, and I. Mercader, Subharmonic instabilities of Tollmien-Schlichting waves in two-dimensional Poiseuille flow, Phys. Rev. E **60**, 1781 (1999).
[37] J. Burke and E. Knobloch, Localized states in the generalized Swift-Hohenberg equation, Phys. Rev. E **73**, 056211 (2006).
[38] J. Burke and E. Knobloch, Snakes and ladders: Localized states in the Swift-Hohenberg equation, Phys. Lett. A **360**, 681 (2007).
[39] M. Chantry and R. R. Kerswell, Localization in a spanwise-extended model of plane Couette flow, Phys. Rev. E **91**, 043005 (2015).

[40] T. Price and Y. Brachet, M. Pomeau, Numerical characterization of localized solutions in plane Poiseuille flow, Phys. Fluids A **5**, 762 (1993).
[41] C. Kelley, *Solving Nonlinear Equations with Newton's Method* (SIAM, Philadelphia, PA, 2003).
[42] Y. A. Kuznetsov, *Elements of Applied Bifurcation Theory*, 3rd ed. (Springer, Berlin, 2004).
[43] J. Prat, I. Mercader, and E. Knobloch, Resonant mode interactions in Rayleigh-Bénard convection, Phys. Rev. E **58**, 3145 (1998).
[44] K. Melnikov, T. Kreilos, and B. Eckhardt, Long-wavelength instability of coherent structures in plane Couette flow, Phys. Rev. E **89**, 043008 (2014).
[45] L. N. Trefethen and D. Bau, *Numerical Linear Algebra*, 1st ed. (SIAM, Philadelphia, PA, 1997).

2.4 Further research

One of the main questions after finding the novel MTSW connections, bridging stable upper-upper branches of consecutive replicas, was their role in the streamwise localisation mechanism previously investigated by Mellibovsky & Meseguer (2015). The main hypothesis was that these branches, together with the asymmetric MATSW counterparts, may complement the scenario reported by previous works. To shed light on this, we began by performing systematic continuations of these branches in both k and Re parameters. Fig. 2.5a shows the continuation in wavenumber k of the MTSW (solid black) bridging replicas $R_3 - R_4$, for a constant $Re = 4450$. Homotopies in k for moderate Re exhibit qualitatively equivalent scenarios with relatively simple connections. Unfortunately, when extending the analysis to slightly higher Re, the bridging connections significantly increase in complexity, experiencing further saddle-nodes bifurcations leading to cluttered branches with several solutions coexisting in a relatively small region of the parameter space; see Fig. 2.5b showing MTSW continuations in Re for $k = 0.32$ (solid blue) and $k = 0.30$ (solid black).

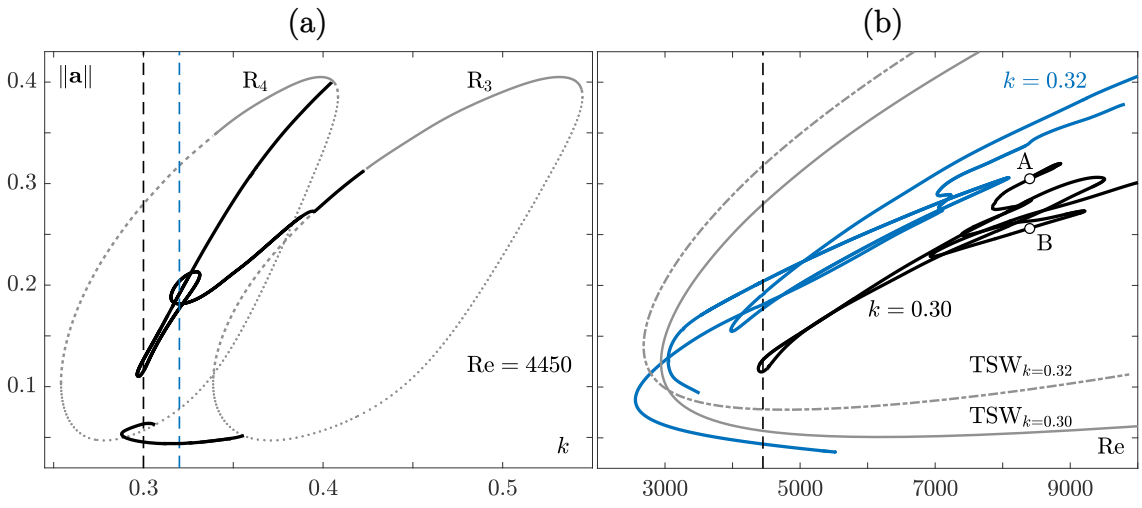

Figure 2.5. (a) MTSW continuation branch (solid black) bridging $R_3 - R_4$ replicas for a constant $Re = 4450$. (b) Continuations in Re of the same MTSW branch for $k = 0.32$ (solid blue) and $k = 0.30$ (solid black). Gray lines correspond to indicated TSW.

What is more interesting is how solutions evolve when progressing along these branches. Fig. 2.6 shows the flow for solution points A and B in Fig. 2.5b. In this particular case, solutions belonging to lower stage branches exhibit simpler flows

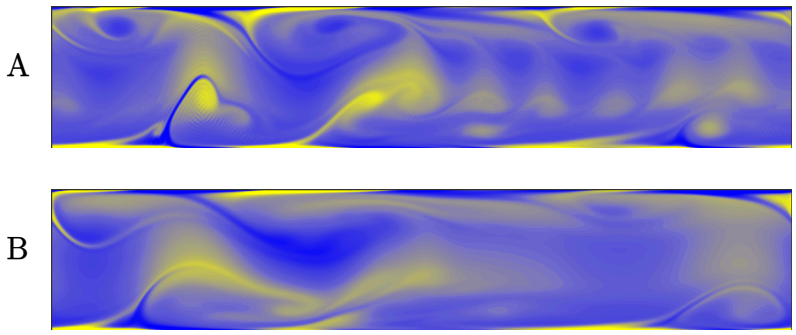

Figure 2.6. Flows corresponding to solution points A and B of Fig. 2.5b. Positive (yellow) and negative (blue) values of vorticity contours correspond to $\omega_\theta = \pm 2.38$ and $\omega_\theta = \pm 1.86$ for solutions A and B, respectively.

dominated by strong big vortex that, even though the short length of the domain, start to localise (point B). Then, MTSW branches evolve and experience several saddle-node bifurcations, progressively increasing the flow complexity. For the highest branch (point A), a novel interesting flow feature becomes apparent: a secondary vortex street detaching from the principal vortex develops streamwise. Unfortunately, these explorations could not be further extended to subsequent replicas due to the high number of unstable directions of the branches under study.

2.5 Concluding remarks

In spite of the fact that PPF has been intensively studied during decades, new symmetry-breaking solutions have been found as a result of a superharmonic pitchfork bifurcation that breaks the usual half-shift and reflect symmetry. Although initially these ATSW are unstable travelling waves emerging from the lower branch of the characteristic TSW surface, stable asymmetric solutions are found when increasing Re due to a codimension-2 cusp bifurcation. When analysing their linear stability for longer domains, time-periodic space-modulated asymmetric solutions arise from subharmonic Hopf bifurcations and interact with the classical MTSW branches.

At the end of this research, the dynamical relevance of the new solutions remained unclear, in part due to the difficulty of tracking MATSW branches in parameter space. The main hypothesis was that, as many lower branch solutions in other canonical problems, these asymmetric branches could play an effective role in the phenomenon

of an eventual boundary crisis (Ritter *et al.*, 2016), participating in the global bifurcation scenario as part of a strange repellor. However, in a very recent work by Markeviciute & Kerswell (2021) in two-dimensional turbulent PPF, systematic visits to stable *asymmetric* and symmetric turbulent states for $\mathrm{Re} \in [21000, 42000]$ were reported. This suggests that the ATSW initially reported by Ayats *et al.* (2020b) become dynamically relevant when increasing Re.

The role of the lower branch right-hand side MTSW family, missing in Mellibovsky & Meseguer (2015) exploration, has been clarified. Although these solutions do not exhibit a localisation mechanism for the analysed domain lengths, they actively interact with other MTSW families by means of codimension-2 bifurcation points, bridging stable upper-upper branches of consecutive TSW replicas. Accordingly, this suggests that, for sufficiently long domains, these solutions may also follow similar mechanisms to the other branches and completely detach from the TSW surface, experiencing a clear localisation.

Chapter 3

Fully nonlinear mode competitions in Taylor-Couette flow

Rotating flows occur in a vast range of situations such as in astronomical accretion disks or in industrial applications involving fluid mixing. In this sense, the Taylor-Couette flow (TCF), namely the flow of a viscous fluid confined between independently rotating coaxial cylinders, is often an appropriate setup for understanding the transition to turbulence in such situations, where shear instabilities compete with centrifugal instabilities. In particular, in this chapter we address the mode competition between different spiral modes in the counter-rotation region of TCF.

3.1 Introduction

The TCF has long served as a canonical prototype for analysing the transition from laminar to turbulent flow by means of hydrodynamic stability theory. The combination of centrifugal and shear instabilities result in an innumerable set of nonlinear patterns whose sequence, progressively increasing the spatio-temporal complexity, successfully describes the transition process (Coles, 1965; Andereck *et al.*, 1986; Chossat & Iooss, 1994; Tagg, 1994). Fig. 3.1a shows a schematic representation of a classical TCF apparatus, where r_i, r_o, Ω_i and Ω_o are inner and outer radii and angular velocity, respectively. In this set, the trivial analytical solution of the Navier-Stokes

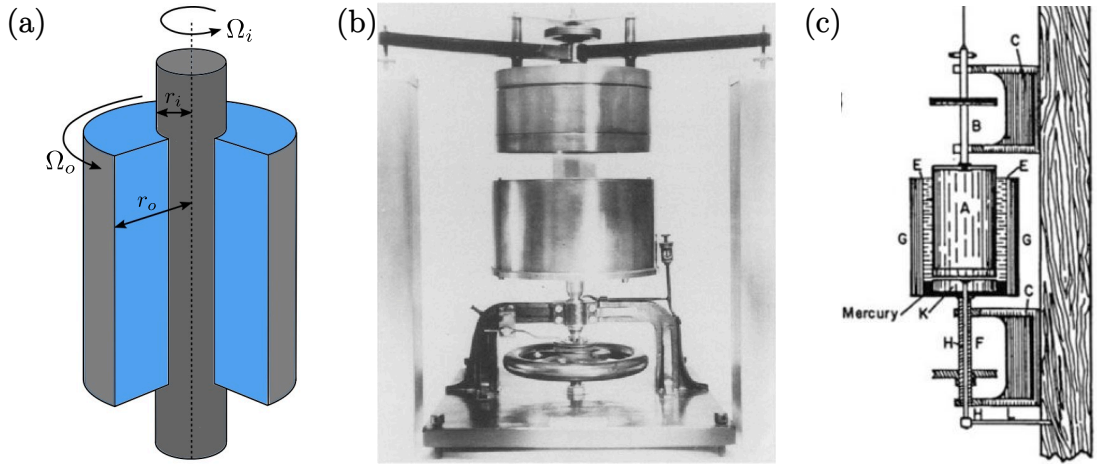

Figure 3.1. (a) Sketch of the classical TCF setup. (b) Original Couette (1888) apparatus (reproduced from Piau *et al.*, 1994). (c) Sketch of Mallock's apparatus (reproduced from Andereck & Hayot, 2012).

equations, i.e., the basic laminar flow, is the well known Circular Couette flow (CCF), derived later in §3.3 (see Eq. 2.5).

This particular apparatus was initially designed by Couette (1888) as an experimental device to estimate the viscosity of different fluids. In the original setup, showed in Fig. 3.1b, the outer cylinder was forced to rotate at a constant angular velocity Ω_o, while the inner cylinder moved freely, exclusively driven due to the friction exerted by the fluid. For moderate values of Ω_o, the CCF was stable and the viscosity could be estimated from the inner cylinder torque. However, if Ω_o was further increased to very high values, CCF was no longer observed and the flow became turbulent. In parallel to Couette experiments, Mallock (1889) worked with an improved rotating cylinder viscosimeter whose inner and outer cylinders were both independently driven at constant angular speeds. For the case of the outer cylinder at rest, Mallock never observed the CCF and reported that this basic solution was always unstable, independently of the Ω_i parameter choice. In fact, CCF was only observed for low Ω_o rotation speeds, always with $\Omega_i = 0$. The apparent contradiction between both studies was finally clarified by Taylor (1923), who accurately computed the base flow instability responsible for the appearance of the first nonlinear structure. Taylor calculated with a significant accuracy the critical angular velocity Ω_{i-crit} above which CCF becomes unstable to stationary infinitesimal axisymmetric disturbances, leading to the so-called *Taylor vortex flow* (TVF). From Taylor's computations it can be now concluded that Mallock's experiments were

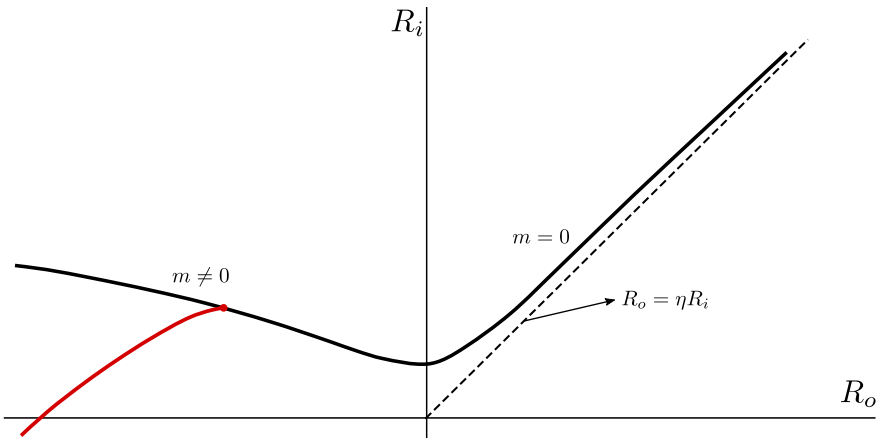

Figure 3.2. General scheme of the CCF classical neutral stability curve (solid black) in the R_i-R_o parameter space. The new instability reported by Deguchi (2017) and Rayleigh's stability criterion are depicted in red and dashed lines, respectively.

carried out by setting inner angular speeds above the critical threshold for which the TVF instability occurs, that is $\Omega_i^{Mallock} > \Omega_{i-crit}$ (Andereck & Hayot, 2012).

3.1.1 Base flow instabilities

Lord Rayleigh (1917) established the first stability criterion for rotating fluids by considering centrifugal inviscid instability to axisymmetric disturbances. According to this criterion, the rotating inviscid flow is stable whenever the modulus of the angular momentum increases outwards. Considering the conventional inner and outer Reynolds number definitions $R_i = (r_o - r_i)r_i\Omega_i/\nu$ and $R_o = (r_o - r_i)r_o\Omega_o/\nu$, where ν is the kinematic viscosity of the fluid, the basic laminar CCF is stable within the region bounded by the Rayleigh's line $R_o = \eta R_i$, with $\eta = r_i/r_o$ being the radius ratio of the cylinders, and the axis $R_i = 0$; see Fig. 3.2. However, as Taylor (1923) initially reported, the region of stability of CCF is further extended above the Rayleigh's boundary due to viscous stabilisation effects. Fig. 3.2 schematically depicts the neutral stability curve (in black) bounding the stable CCF region.

The stability of CCF can be accurately computed by means of a normal mode analysis, considering the effect of small disturbances that are periodic in azimuthal and axial directions. The total velocity field $\mathbf{v}$ to be analysed is

$$\mathbf{v}(r, \theta, z, t) = v_b(r)\hat{\theta} + \tilde{\mathbf{v}}(r)e^{i(m\theta + kz) + \lambda t}, \tag{3.1}$$

being $v_b(r)$ the azimuthal CCF, $\tilde{\mathbf{v}}(r)$ the perturbation velocity field, and $m \in \mathbb{Z}$, $k \in \mathbb{R}$, $\lambda \in \mathbb{C}$ the azimuthal and axial wavenumbers and the eigenvalues, respectively. Introducing this expression in the governing equations, neglecting the nonlinear terms and discretising the boundary value problem by a solenoidal Petrov-Galerkin spectral method, leads to a classical eigenvalue problem, where the linear stability is then reduced to the computation of the spectrum of eigenvalues for each pair of (m, k) azimuthal-axial modes (see Meseguer (2002) for further details).

Computations of the CCF stability show that in the co-rotating region, i.e., $R_i R_o \geq 0$, the first instability occurs through a single real eigenvalue crossing the imaginary axis, corresponding to an axisymmetric mode of azimuthal wavenumber $m = 0$ leading to TVF. Although the same scenario extends slightly in the region of counter-rotation, $R_i R_o < 0$, soon the axisymmetric instability is surpassed by non-axisymmetric modes with $m \neq 0$. The origin of these instabilities is a pair of complex conjugated eigenvalues crossing the imaginary axis, usually leading to spiral modes. It is worth mentioning that when progressing in the counter-rotation region, the neutral curve depicted in Fig. 3.2 is a continuous but not differentiable line, as it is conformed by the sequence of critical spiral modes instabilities with progressively increasing azimuthal wavenumber.

In addition, a new CCF instability, corresponding to a spiral mode of low azimuthal wavenumber, has been recently reported by Deguchi (2017); see Fig. 3.2 red line. This instability occurs for very high R_o and appears far below the classical neutral stability curve, even reaching into the co-rotating Rayleigh stable region.

3.1.2 Nonlinear structures in TCF

Since Taylor (1923) investigated both theoretically and experimentally the first nonlinear structure emerging from CCF, a large amount of studies have been devoted to explore TCF and its rich nonlinear patterns. In particular, we emphasise the vast explorations carried out by Coles (1965) reporting up to 26 novel stable flows, including intermittency and the hysteretical spiral turbulence, which was later characterised by Van Atta (1966) and Coles & Van Atta (1967). Following these explorations, Andereck *et al.* (1986) widely explored TCF parameter space, analysing the stable patterns for almost all possible combinations of R_i-R_o. Fig. 3.3 shows the celebrated Andereck's regime diagram, corresponding to an experimental setup with $\eta = 0.883$.

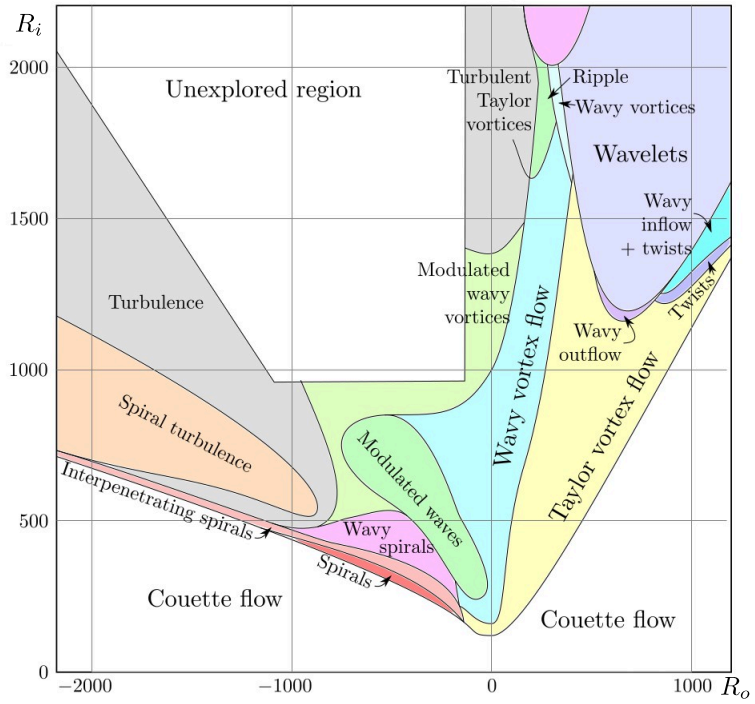

Figure 3.3. Stable TCF regime diagram in the parameter space R_i-R_o (Duda *et al.*, 2019, following Andereck *et al.* (1986)).

Starting with the outer cylinder at rest and progressively increasing R_i, the CCF is stable and observed up to a critical Reynolds number R_{i-crit}, past which point the steady axisymmetric TVF emerges supercritically. This nonlinear structure is axially periodic and consists in a vertical array of axisymmetric cells of counter-rotating vortex pairs (see Fig. 3.4a). Each pair of vortices has a well defined wavelength $\lambda = 2\pi/k$, where k is the axial wavenumber.

When increasing R_i, TVF soon becomes unstable by means of a Hopf bifurcation breaking the azimuthal invariance of the axisymmetric cells. Azimuthal rotating waves, known as *wavy vortex flow* (WVF), emerge travelling at a constant speed (King *et al.*, 1984). Fig. 3.4b shows azimuthal vorticity isosurfaces of a WVF with azimuthal wavenumber $m = 8$. Although these waves are time-periodic due to the azimuthal drift, WVF is reduced to a relative equilibrium when observed from an appropriately co-rotating reference frame. For slightly higher R_i, WVF exhibits yet another Hopf bifurcation adding an extra oscillation frequency, and leading to the quasi-periodic waves known as *modulated wavy vortices* (MWV). In turn, in a co-moving reference frame, MWV appear as relative periodic orbits oscillating around the WVF.

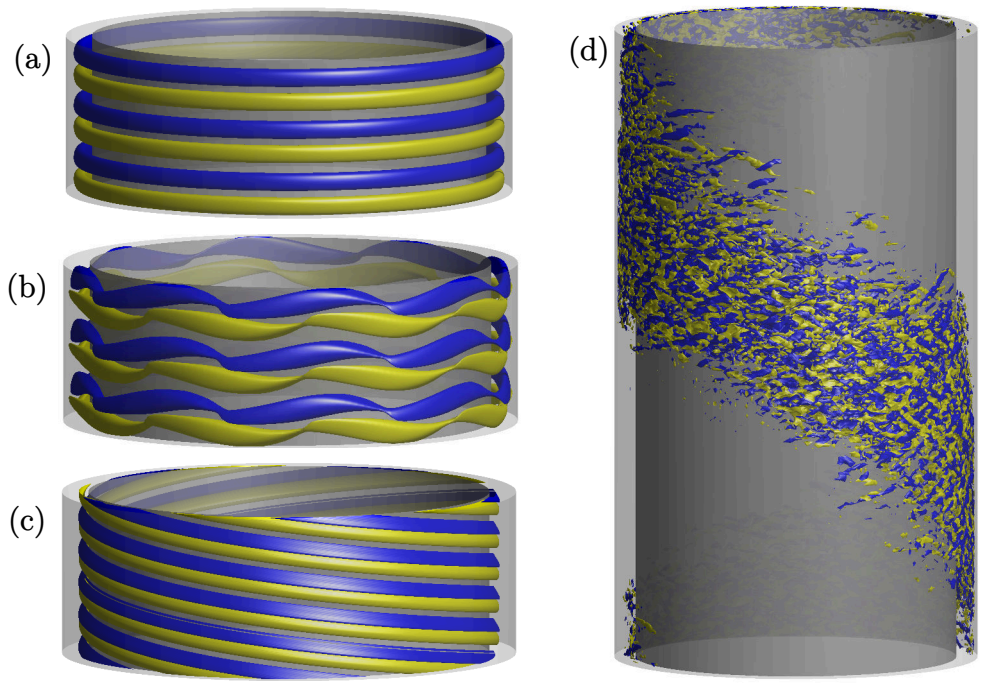

Figure 3.4. Azimuthal vorticity isosurfaces for stable ECS in TCF with $\eta = 0.883$. (a) TVF with $k = 3.13$ at $(R_i, R_o) = (125, 0)$. (b) WVF with $(k, m) = (3.13, 8)$ at $(R_i, R_o) = (200, 0)$. (c) Spiral S_5 with $(k, m) = (5.122, 5)$ at $(R_i, R_o) = (500, -1200)$. (d) SPT regime at $(R_i, R_o) = (600, -3000)$. Positive (yellow) and negative (blue) isosurfaces dimensionless values correspond to (a) $\omega_\theta = \pm 10$, (b) $\omega_\theta = \pm 80$, (c) $\omega_\theta = \pm 100$ and (d) $\omega_\theta = \pm 2000$.

By contrast, the first instabilities observed in most counter-rotation regimes are characterised by possessing azimuthal wavenumbers $m \neq 0$. In practice, these equilibria, i.e., *spiral vortices* (SPI), are nonlinear structures that coil around the apparatus gap with a predefined constant tilt (see Fig. 3.4c). The usual patterns observed when increasing R_o are not limited to such simple flows but also to nonlinear interactions between different spiral modes. That is the case of *interpenetrating spirals* (IPS) and *ribbons*, which are superpositions of a couple of spirals with different or exactly opposite azimuthal wavenumbers, respectively. Furthermore, in contrast to the aforementioned co-rotating flows, spirals and IPS have been found to be slightly subcritical and coexist with the stable CCF (Meseguer *et al.*, 2009a). In addition, the new spirals arising from the instability reported by Deguchi (2017) stand out from conventional modes by having significantly smaller azimuthal and axial wavenumbers, leading to long-wavelength spirals with a conspicuous high slope.

Intermittency, involving the coexistence of laminar and turbulent flow regions, is probably the most puzzling phenomenon observed in counter-rotating TCF. The resulting turbulent-laminar patterns usually arise in the form of localised spots, for lower R_i, or coherent stripes constituting a turbulent helix, for higher R_i. This characteristic helix, tilted in the direction of the main flow and rotating at nearly constant speed, is the so-called *spiral turbulence* (SPT) regime; see Fig. 3.4d. Another feature of this structure is its coexistence with the stable CCF, exhibiting highly subcritical hysteretical cycles (Andereck *et al.*, 1986; Meseguer *et al.*, 2009b; Crowley *et al.*, 2020). The bifurcation scenario or the nonlinear structures responsible for the appearance of SPT are still unknown, and most of the current analyses are focused on finding initial seeds or precursors of these enigmatic patterns, following similar successful explorations in Plane Couette (Barkley & Tuckerman, 2005; Reetz *et al.*, 2019) or Plane Poiseuille (Paranjape *et al.*, 2020).

3.1.3 Non-orthogonal computational domain

So far, most of numerical studies in TCF have used a classical orthogonal computational domain with periodic boundary conditions, whose axes were parallel to the azimuthal and axial directions. However, this definition is not efficient for computing spirals, ribbons, IPS or mixed modes, as large computational boxes are required to appropriately capture the periodic patterns. Especially for these purposes, Deguchi & Altmeyer (2013) proposed an alternative computational domain whose directional axes were arbitrary defined, thus allowing for tilted and skewed domains conveniently aligned with the directions of the spirals. Therefore, the required total size of the computational domain can be drastically reduced.

To better illustrate this concept, we present the following example based on Deguchi & Altmeyer (2013) explorations for a constant $R_o = -1200$ and $\eta = 0.883$. We first compute the spiral S_5, shown in Fig. 3.5a, defined with the wavenumbers $(m_5, k_5) = (5, 5.122)$. Separately, we compute the spiral S_{-4} characterised by the wavenumbers $(m_4, k_4) = (-4, 3.94)$; see Fig. 3.5b. The minimal orthogonal computational box to capture each of the structures separately is $(\theta, z) \in [0, 2\pi/m] \times [0, 2\pi/k]$. In order to capture the mixed mode resulting from the nonlinear interaction between spirals, S_{5-4}, the minimal orthogonal computational domain has to simultaneously reproduce both structures, fulfilling the periodic boundary conditions. This is accomplished within the domain $(\theta, z) \in [0, 2\pi] \times [0, 2\pi/k_{5-4}]$, where k_{5-4} is the re-

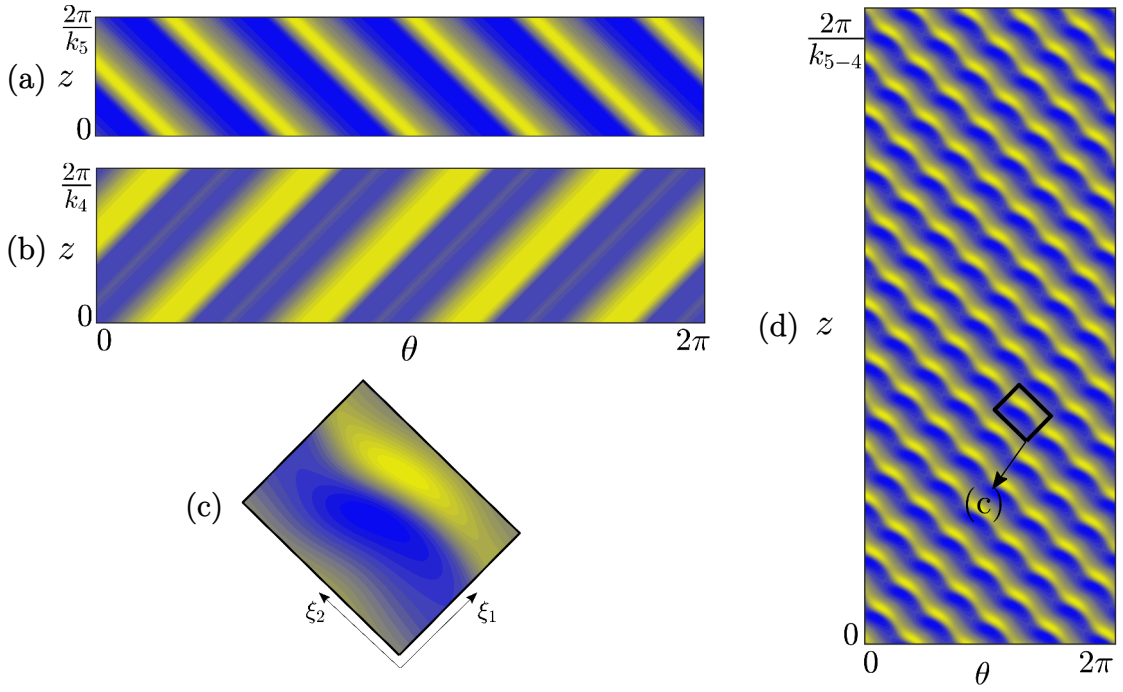

Figure 3.5. Radial vorticity contours on the unfolded cylinder surface at $r = r_i + (r_o - r_i)/4$, $R_o = -1200$ and $\eta = 0.883$. (a) Spiral S_5 with $(m_5, k_5) = (5, 5.122)$ at $R_i = 460$. (b) Spiral S_{-4} with $(m_4, k_4) = (-4, 3.94)$ at $R_i = 470$. (d) Mixed mode S_{5-4} in the classical orthogonal domain at $R_i = 450$. Small box in black represents the skewed minimal domain detailed in (c).

sulting axial wavenumber defined as $k_{5-4} = k_4/q = k_5/n$ with $n \in \mathbb{N}$ and $q \in \mathbb{N}$ derived from the irreducible fraction $n/q = k_5/k_4$. Fig. 3.5d shows a S_{5-4} mixed mode in this orthogonal domain.

Following the non-orthogonal domain definition, the new axes directions aligned with the wavefronts of the spirals will be $\xi_1 = m_5\theta + k_5 z$ and $\xi_2 = m_4\theta + k_4 z$ (see §3.3 Eq. 2.9 for further details). This computational domain, shown in Fig. 3.5c, is able to capture the same structure in a 1/100 part of the original orthogonal box area.

3.1.4 Magnetised Taylor-Couette flow

Magnetised Taylor-Couette flow has been widely used as a benchmark for magneto-hydrodynamic stability theory. Basically, it consists of a Taylor-Couette apparatus filled with an electrically conductive fluid, and subject to the action of an external

magnetic field. This magnetic field induces electric fields and currents on which magnetic forces are exerted, modifying the flow dynamics (Landau & Lifshitz, 1984). Therefore, the TCF parameter space depicted in Fig. 3.3 is altered by magneto-rotational instabilities (MRI) that overlap and interact with purely hydrodynamic instabilities.

The first MRI was reported by Velikhov (1959) and Chandrasekhar (1960) in the co-rotation region, between Rayleigh's and solid body rotation lines, by considering a uniform axial magnetic field. This type of hydromagnetic instability is usually referred to as *standard* MRI (SMRI). Following these initial works, several MRI have been found both in the co-rotation and counter-rotation regions when considering azimuthal or azimuthal-axial magnetic fields leading to *azimuthal* MRI (AMRI) and *helical* MRI (HMRI), respectively. For a detailed explanation of these instabilities we refer the reader to § 3.3 (Sec. 1).

The study of the magnetised TCF is crucial for understanding accretion disks, that is, flattened astronomical objects made of rapidly rotating gases. In spite of the hydrodynamic stability of these disks, the transport of angular momentum can only be explained by the presence of turbulence coming from an hydromagnetic instability (Balbus & Hawley, 1991). Hydromagnetic dynamos and the generation of turbulence in the Sun's tachocline (Masada, 2011; Kagan & Wheeler, 2014) are other examples where MRI are thought to play an important role.

3.2 Research objectives

The main goal of this research is to compute the purely hydrodynamical mixed modes resulting from the nonlinear interaction between the classical spiral instabilities and the new mode reported by Deguchi (2017). We apply the skewed domain definition and perform detailed explorations of the arising structures such as spirals, mixed modes and ribbons, in the neighbourhood of the bicritical instability point.

Due to the particular features of the new CCF instability, combining low azimuthal wavenumbers with higher tilts than the classical modes, extensive explorations of the emerging structures are performed in search of possible subcriticalities that might act as SPT precursors.

3.3 Indexed publication

This section is a reproduction of Ayats *et al.* (2020a), summarising the most relevant research performed in TCF.

J. Fluid Mech. (2020), *vol.* 897, A14.
Published by Cambridge University Press
doi:10.1017/jfm.2020.365

Fully nonlinear mode competition in magnetised Taylor–Couette flow

R. Ayats[1,†], K. Deguchi[2,†], F. Mellibovsky[1,†] and A. Meseguer[1,†]

[1]Departament de Física, Universitat Politècnica de Catalunya, 08034 Barcelona, Spain

[2]School of Mathematics, Monash University, VIC 3800, Australia

(Received 12 February 2020; revised 14 April 2020; accepted 2 May 2020)

We study the nonlinear mode competition of various spiral instabilities in magnetised Taylor–Couette flow. The resulting finite-amplitude mixed-mode solution branches are tracked using the annular-parallelogram periodic domain approach developed by Deguchi & Altmeyer (*Phys. Rev.* E, vol. 87, 2013, 043017). Mode competition phenomena are studied in both the anticyclonic and cyclonic Rayleigh-stable regimes. In the anticyclonic sub-rotation regime, with the inner cylinder rotating faster than the outer, Hollerbach *et al.* (*Phys. Rev. Lett.*, vol. 104, 2010, 044502) found competing axisymmetric and non-axisymmetric magneto-rotational linearly unstable modes within the parameter range where experimental investigation is feasible. Here we confirm the existence of mode competition and compute the nonlinear mixed-mode solutions that result from it. In the cyclonic super-rotating regime, with the inner cylinder rotating slower than the outer, Deguchi (*Phys. Rev.* E, vol. 95, 2017, 021102) recently found a non-axisymmetric purely hydrodynamic linear instability that coexists with the non-axisymmetric magneto-rotational instability discovered a little earlier by Rüdiger *et al.* (*Phys. Fluids*, vol. 28, 2016, 014105). We show that nonlinear interactions of these instabilities give rise to rich pattern-formation phenomena leading to drastic angular momentum transport enhancement/reduction.

Key words: Taylor–Couette flow, magnetohydrodynamics, bifurcation

1. Introduction

The objective of this study is the nonlinear interactions between various instability modes occurring in magnetised Taylor–Couette flow, i.e. the fluid flow between independently rotating concentric cylinders. The purely hydrodynamic Taylor–Couette flow, in the absence of a magnetic field, has long served as a theoretical, numerical and experimental test bench for the study of centrifugal and shear instability mechanisms. Keeping the outer cylinder stationary, Taylor (1923) observed that the flow is destabilised by purely hydrodynamic axisymmetric perturbations at a certain critical speed of the inner cylinder. The balance between rotational and shear effects can be modified by further introducing a rotation of the outer cylinder.

† Email addresses for correspondence: roger.ayats@upc.edu, kengo.deguchi@monash.edu, fernando.mellibovsky@upc.edu, alvaro.meseguer@upc.edu

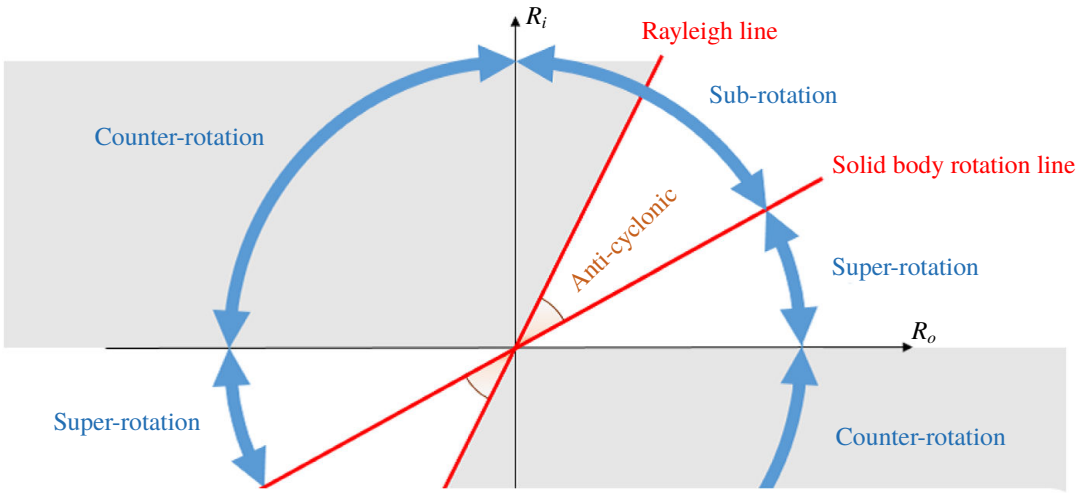

FIGURE 1. The R_i–R_o parameter space representation of Taylor–Couette flow. The plane is divided into the counter-rotation and the co-rotation regimes. This latter is further subdivided into sub-rotation and super-rotation by the solid-body rotation line defined by equal angular speeds of both cylinders. The shaded regions denote inviscid instability of circular Couette flow following the Rayleigh criterion. The portion of the sub-rotation regime between the Rayleigh and solid-body rotation lines goes by the name of anticyclonic regime (also called quasi-Keplerian), while the rest of the plane is called cyclonic.

The independent variation of the inner and outer cylinder speeds results in a rich diversity of secondary nonlinear flow patterns, as reported by Andereck, Liu & Swinney (1986). The stability and nonlinear states of Taylor–Couette flow are commonly studied in the R_i–R_o parameter space schematically depicted in figure 1, where R_i and R_o are the Reynolds numbers associated with the inner and outer cylinder speeds, respectively.

In accordance with the symmetries of the problem, the R_i–R_o parameter plane is invariant to π rotation about the origin, such that only the upper half-plane needs to be explored. The right/left of the half-plane corresponds to cylinders rotating in the same/opposite direction (i.e. co-rotation/counter-rotation). The first quadrant (co-rotation regime) is divided into sub-rotation and super-rotation by the solid-body rotation line (equal angular speed of the cylinders), depending on whether the outer cylinder rotates slower or faster than the inner. For any given speed of the outer cylinder, Rayleigh's inviscid stability criterion establishes that circular Couette flow remains centrifugally stable to infinitesimal axisymmetric perturbations as long as the inner cylinder is steady or in co-rotation up to a certain speed, delimited by the so-called Rayleigh line (the wedge-shaped white region in figure 1 between the Rayleigh line and the horizontal $R_i = 0$ line). Taking viscous effects and non-axisymmetric perturbations into account affects the stability boundaries, but it is widely accepted that the Rayleigh line acts as a fairly approximate threshold below which circular Couette flow remains the only stable state, given that no experimental or numerical evidence of nonlinear flow states has been found to date (see Ji *et al.* 2006; Edlund & Ji 2014; Lopez & Avila 2017). Note, however, that no first-principles theory has been advanced so far to support the nonlinear hydrodynamic stability in the quasi-Keplerian flow regime (see Balbus (2017), for a summary on the matter).

The Rayleigh-stable region is further subdivided into the anticyclonic and super-rotation cyclonic regimes by the solid-body rotation line, corresponding to both

cylinders rotating at the same angular speed. Immediately to the right of the Rayleigh line and all the way down to solid rotation, co-rotation and sub-rotation are said to be anticyclonic and laminar Couette flow is allegedly linearly stable. This region is of utmost astrophysical interest, since Keplerian rotational flow, a vastly used model for accretion disks, is precisely anticyclonic. The rate at which angular momentum is radially transported in observation of astrophysical accretion disks requires the flow to be turbulent. This has motivated a wealth of studies (see the review paper by Rüdiger *et al.* (2018*a*)) exploring magneto-rotational instabilities (henceforth referred to as MRI) as a possible alternative source for turbulence in a flow that appears otherwise to always revert back to laminar in the absence of magnetic fields. The pioneering works by Velikhov (1959) and Chandrasekhar (1960) showed that a uniform external magnetic field in the axial direction indeed destabilises the anticyclonic regime, while the importance of the instability in the astrophysical context was noted for the first time by Balbus & Hawley (1991). This type of MRI is nowadays called the standard type of MRI, SMRI for short.

A different approach was nevertheless taken in the first experimental observation of the MRI (Stefani *et al.* 2006). The SMRI is actually very difficult to reproduce in liquid-metal experiments where the magnetic Prandtl number P_m is very small, as magnetic induction is essential in this case. As shown by Goodman & Ji (2002), the critical Reynolds number of the SMRI is inversely proportional to the magnetic Prandtl number P_m for small P_m, meaning that the cylinders must rotate at an extremely fast rate to trigger the SMRI in the experimental apparatus. The crux in reproducing a MRI at relatively small Reynolds numbers was the numerical finding by Hollerbach & Rüdiger (2005) that, when both azimuthal and axial external magnetic fields are applied simultaneously, the critical Reynolds number saturates at a finite value even in the inductionless limit of $P_m \to 0$. Soon after the discovery of this helical MRI (henceforth referred to as HMRI), growth of axisymmetric perturbations was confirmed in the series of PROMISE experiments (Rüdiger *et al.* 2006; Stefani *et al.* 2006, 2007). Later on, Hollerbach, Teeluck & Rüdiger (2010) found that non-axisymmetric modes arise instead when purely azimuthal magnetic fields are considered in the sub-rotation regime just below the Rayleigh line. They further showed that these so-called azimuthal magneto-rotational instability (AMRI) modes persist when a small axial magnetic field is added to the predominantly azimuthal field, thus implying that they could potentially interact with the axisymmetric HMRI mode. In fact, when the strengths of the azimuthal and axial external magnetic fields are suitably adjusted, the critical Reynolds numbers for the axisymmetric and non-axisymmetric modes become comparable. The competition of these modes may yield rich nonlinear flow patterns at this particular HMRI regime. This nonlinear mode interaction is the first subject we will tackle in this study.

In the early years of the pattern-formation theoretical studies in purely hydrodynamic Taylor–Couette flow, weakly nonlinear analysis was employed to investigate mode interactions among multiple linear instability modes near criticality (e.g. Davey, DiPrima & Stuart 1968; Iooss 1986; Golubitsky, Stewart & Schaeffer 1988; Chossat & Iooss 1994). The simplest mode interaction occurs between two identical but mutually symmetric, with respect to an axial reflection, spiral modes. In this case, the fully nonlinear mixed-mode solution can be computed in numerical simulations using a periodic axial–azimuthal orthogonal domain (Tagg *et al.* 1989). However, when the interacting spirals are not mutually symmetric and have a different absolute pitch, as are indeed the two mode interactions studied here, the numerical computation of the fully nonlinear mixed mode is no longer straightforward. The periodic computational domain must fit an integer number of both constituent modes in order to faithfully reproduce the mixed mode, which may lead to unaffordably large

domains. This may be feasible on some occasions (Avila, Meseguer & Marques 2006; Pinter, Lücke & Hoffmann 2006; Altmeyer & Hoffmann 2010), but it is at the very least inefficient from a computational point of view, if not altogether prohibitive. A convenient methodology for the computation of general mixed-mode states was provided by Deguchi & Altmeyer (2013), who realised that the infinite annulus might be subdivided into a regular tiling of a suitable parallelogram-shaped periodic box that can be chosen optimally small for any flow pattern arising from nonlinear interaction of two modes, as we are considering here. Extension of the nonlinear code to magnetised problems might prove highly valuable to the study of MRI, as nonlinear simulations in cylindrical/annular domains have only recently been undertaken (Guseva *et al.* 2015, 2017).

In the second half of this paper we shall also study the nonlinear mode competition occurring in the other Rayleigh-stable regime, i.e. the super-rotation regime seen in figure 1. Recently, magnetohydrodynamic (MHD) instabilities in this regime have attracted much attention as they are thought to be relevant for turbulence generation in a part of the Sun's tachocline. In this second subject we shall investigate the nonlinear competition of two recently discovered linear instability modes.

For the purely hydrodynamic problem, non-laminar flow patterns in the inviscidly stable super-rotation regime were first reported several decades ago in Taylor–Couette experiments by Wendt (1933) and Coles (1965), but at the time it was not clear whether the instability was legitimate or an endwall effect induced by the cylinder lids. Advances in computational power eventually allowed numerical confirmation of the existence of subcritical spiral turbulence and intermittency found experimentally (Van Atta 1966; Hegseth *et al.* 1989; Prigent *et al.* 2002; Burin & Czarnocki 2012) in the counter-rotation regime in the absence of endwall effects (Dong 2009; Meseguer *et al.* 2009). Nonlinear coherent states have indeed been followed into the super-rotation regime, crossing the $R_i = 0$ boundary, as illustrated by the computation of the first rotating wave in cyclonic super-rotation (Deguchi, Meseguer & Mellibovsky 2014) and by direct numerical simulation (Ostilla-Monico, Verzicco & Lohse 2016). All non-trivial flow patterns hitherto observed in super-rotation are finite-amplitude and highly nonlinear, such that they by no means belie the widely assumed linear stability of super-rotating hydrodynamic Taylor–Couette flow, in view of countless numerical studies of the neutral curve (see the review article by Grossmann, Lohse & Sun (2016)). The recent unexpected discovery by Deguchi (2017) of a linear instability in the super-rotation regime therefore came as a big surprise. Considering non-axisymmetric perturbations and a relatively long axial wavelength were key ingredients to the finding. This instability mode of a purely hydrodynamic nature, hereafter called the D17 mode, is the first of the two modes we shall consider in our second mode competition study.

The other mode at play inherently originates from the MRI mechanism and is called the super-AMRI (Rüdiger *et al.* 2016, 2018*b*), where the prefix 'super' refers to the super-rotation regime. This mode belongs, along with the usual forms of HMRI and AMRI for sub-rotation, to the class of inductionless MRI. It has long been known that MRI is not easily triggered in the super-rotation regime for the axisymmetric case. For ideal fluids, Velikhov's condition states that the axial magnetic field cannot destabilise this regime (Velikhov 1959), while according to Michael's condition (Michael 1954), an azimuthal field can only be destabilising provided its modulus increases outwards at a sufficiently fast rate. Moreover, when the azimuthal magnetic field is current-free, it can be formally shown that axisymmetric MRI are impossible in spite of the diffusive effect (Herron & Soliman 2006). A breakthrough regarding instability in the cyclonic

super-rotation regime is due to Stefani & Kirillov (2015), who pointed out that for sufficiently narrow gaps the non-axisymmetric instability could be continued into the super-rotation regime using the so-called local approximation and the inductionless limit ($P_m \to 0$). However, the existence of the super-AMRI was not conclusive at this stage given that a local approximation does not always necessarily provide accurate insight into the global problem. Soon after, conclusive numerical evidence of the super-AMRI was reported by Rüdiger *et al.* (2016, 2018*b*), who concluded that the destabilisation seems to occur for fairly arbitrary magnetic field profiles as long as the flow is double-diffusive, i.e. $P_m \neq 1$.

The paper is organised as follows. Section 2 formulates the problem based on the inductionless limit of the MHD equations. The section addresses in detail the numerical discretisation of the equations in annular-parallelogram periodic domains and, in particular, describes the Newton solver for the computation of nonlinear mixed-mode travelling waves using the transformed coordinate system and a suitable co-moving reference frame. Section 3 is devoted to the anticyclonic regime. The helical magnetic field is imposed to find the nonlinear mixed-mode solutions that arise from the mode competition advanced by Hollerbach *et al.* (2010). The first part of § 4 deals with the interaction between the classical non-axisymmetric and the D17 modes in purely hydrodynamic counter-rotating Taylor–Couette flow. In the second half of § 4 we shall see how an imposed azimuthal magnetic field alters the nature of this interaction. Finally, in § 5, we briefly summarise the results and present concluding remarks.

2. Formulation of the problem

Consider an electrically conducting fluid of density ρ^*, kinematic viscosity ν^* and magnetic diffusivity η^*, confined between two concentric cylinders of inner and outer radii r_i^* and r_o^*, independently rotating at angular speeds Ω_i^* and Ω_o^*, respectively. In addition, the fluid is subject to the action of a magnetic field of typical strength B_0^*. Throughout the paper we use the length $d^* = r_o^* - r_i^*$, time d^{*2}/ν^*, velocity ν^*/d^* and magnetic field $\nu^*\sqrt{\rho^*\mu^*}/d^*$ scales for non-dimensionalisation, where μ^* is the magnetic permeability. As a consequence of using the viscous time scale, the Reynolds numbers are absorbed into the expression for the base-state flow fields and disappear from the non-dimensional equations for the perturbation. The key parameters of the flow are the radius ratio η, the inner R_i and outer R_o Reynolds numbers, along with the magnetic Prandtl number P_m and the Hartmann number H:

$$\eta = \frac{r_i^*}{r_o^*}, \quad R_i = \frac{\Omega_i^* r_i^* d^*}{\nu^*}, \quad R_o = \frac{\Omega_o^* r_o^* d^*}{\nu^*}, \quad P_m = \frac{\nu^*}{\eta^*}, \quad H = \frac{B_0^* d^*}{\sqrt{\rho^*\mu^*\eta^*\nu^*}}. \quad (2.1a\text{–}e)$$

The non-dimensional external magnetic field is proportional to $P_m^{-1/2}H$. The reason for using H is that we will consider the so-called inductionless limit $P_m \to 0$ where H is typically fixed as a constant.

Non-dimensionalisation of the velocity field $\boldsymbol{v} = u\boldsymbol{e}_r + v\boldsymbol{e}_\theta + w\boldsymbol{e}_z$ and magnetic field $\boldsymbol{B} = A\boldsymbol{e}_r + B\boldsymbol{e}_\theta + C\boldsymbol{e}_z$, expressed here in cylindrical coordinates (r, θ, z), yields the incompressible viscous–resistive MHD equations:

$$\partial_t \boldsymbol{v} + (\boldsymbol{v}\cdot\nabla)\boldsymbol{v} - (\boldsymbol{B}\cdot\nabla)\boldsymbol{B} = -\nabla p + \nabla^2\boldsymbol{v}, \quad (2.2a)$$

$$\partial_t \boldsymbol{B} + (\boldsymbol{v}\cdot\nabla)\boldsymbol{B} - (\boldsymbol{B}\cdot\nabla)\boldsymbol{v} = P_m^{-1}\nabla^2\boldsymbol{B}, \quad (2.2b)$$

$$\nabla\cdot\boldsymbol{v} = \nabla\cdot\boldsymbol{B} = 0, \quad (2.2c)$$

where p is the total pressure and t is time. Equation (2.2*a*) expresses momentum conservation, while equation (2.2*b*) is the induction equation. Equation (2.2*c*) corresponds to continuity and Gauss' law. Along the cylinder walls at radii

$$r_i = \frac{\eta}{1-\eta}, \quad r_o = \frac{1}{1-\eta}, \tag{2.3a,b}$$

we assume no-slip and perfectly insulating boundary conditions. In our formulation, the velocity and magnetic fields are decomposed into the base and the perturbation flows following

$$\boldsymbol{v} = v_b(r)\boldsymbol{e}_\theta + Gw_p(r)\boldsymbol{e}_z + \widetilde{\boldsymbol{v}}(r,\theta,z,t), \tag{2.4a}$$

$$\boldsymbol{B} = P_m^{-1/2} H\{B_b(r)\boldsymbol{e}_\theta + C_b(r)\boldsymbol{e}_z\} + \widetilde{\boldsymbol{B}}(r,\theta,z,t), \tag{2.4b}$$

where the tilde denotes perturbation quantities. The pressure perturbation is therefore written as $\widetilde{p}$. Here $v_b(r) = R_s r + R_p r^{-1}$ is the laminar Couette flow solution, with coefficients

$$R_s = \frac{R_o - \eta R_i}{1+\eta}, \quad R_p = \frac{\eta^{-1}R_i - R_o}{1+\eta} r_i^2, \tag{2.5a,b}$$

where the subscripts denote the solid-body rotation (s) and the potential (p) components of the flow. External magnetic mechanisms induce the base magnetic fields $B_b(r)$ and $C_b(r)$, which will be duly introduced in (3.1) and (4.1) for the two types of predominantly azimuthal fields that will be considered throughout the paper.

We will assume further that there is no axial net mass flux. This is accomplished by imposing an external instantaneously adjustable axial pressure gradient that induces the well-known base annular Poiseuille flow profile:

$$w_p(r) = (r^2 - r_i^2)\ln r_o + (r_o^2 - r^2)\ln r_i - (r_o^2 - r_i^2)\ln r. \tag{2.6}$$

The product Gw_p in (2.4*a*) represents the axial flow induced by the external pressure gradient, whose strength is measured by the coefficient G. That coefficient is a time-dependent additional unknown in the constant-mass flux problem. For travelling wave states G is merely a constant. Moreover, it is easy to show that, when the flow possesses some symmetry in z, G must vanish.

For liquid metals used in laboratory experiments P_m is very small (10^{-5}–10^{-7}). It is therefore reasonable to apply the inductionless limit approximation $P_m \to 0$ to the governing equations (see e.g. Davidson 2017). The magnetic field perturbation is rescaled as $\widetilde{\boldsymbol{b}} = P_m^{-1/2} H^{-1} \widetilde{\boldsymbol{B}}$ and the size of the variables $\widetilde{\boldsymbol{v}}$, $\widetilde{\boldsymbol{b}}$, $\widetilde{p}$ and R_i, R_o, H are fixed as $O(P_m^0)$ quantities during the limiting process. The resulting leading-order equations are

$$\begin{bmatrix} (\partial_t + r^{-1}v_b\partial_\theta + R_p w_p \partial_z)\widetilde{u} - 2r^{-1}v_b\widetilde{v} \\ (\partial_t + r^{-1}v_b\partial_\theta + R_p w_p \partial_z)\widetilde{v} + r^{-1}(rv_b)'\widetilde{u} \\ (\partial_t + r^{-1}v_b\partial_\theta + R_p w_p \partial_z)\widetilde{w} \end{bmatrix} - H^2 \begin{bmatrix} (r^{-1}B_b\partial_\theta + C_b\partial_z)\widetilde{a} - 2r^{-1}B_b\widetilde{b} \\ (r^{-1}B_b\partial_\theta + C_b\partial_z)\widetilde{b} + r^{-1}(rB_b)'\widetilde{a} \\ (r^{-1}B_b\partial_\theta + C_b\partial_z)\widetilde{c} \end{bmatrix} + (\widetilde{\boldsymbol{v}}\cdot\boldsymbol{\nabla})\widetilde{\boldsymbol{v}} = -\boldsymbol{\nabla}\widetilde{p} + \nabla^2\widetilde{\boldsymbol{v}}, \tag{2.7a}$$

and

$$-\begin{bmatrix}(r^{-1}B_b\partial_\theta + C_b\partial_z)\widetilde{u}\\ (r^{-1}B_b\partial_\theta + C_b\partial_z)\widetilde{v} - r(r^{-1}B_b)'\widetilde{u}\\ (r^{-1}B_b\partial_\theta + C_b\partial_z)\widetilde{w}\end{bmatrix} = \nabla^2\widetilde{\boldsymbol{b}}, \tag{2.7b}$$

along with the solenoidal conditions $\boldsymbol{\nabla}\cdot\widetilde{\boldsymbol{v}} = \boldsymbol{\nabla}\cdot\widetilde{\boldsymbol{b}} = 0$. The time derivative drops out from the induction equations on account of applying the inductionless limit, and (2.7*b*) becomes a mere linear system linking the velocity and the magnetic field. It can thus be used, as will be shown shortly, to eliminate the magnetic perturbation from the momentum equation (2.7*a*).

2.1. *Spectral discretisation on a parallelogram domain*

We shall be looking here for nonlinear travelling wave solutions of the above resulting equations. The hydrodynamic and magnetic perturbation fields $\widetilde{\boldsymbol{v}}$ and $\widetilde{\boldsymbol{b}}$ are both solenoidal, so they admit a toroidal–poloidal decomposition of the form

$$\widetilde{\boldsymbol{v}}(r,\theta,z,t) = \boldsymbol{e}_\theta\overline{v}(r) + \boldsymbol{e}_z\overline{w}(r) + \boldsymbol{\nabla}\times\boldsymbol{\nabla}\times\{\boldsymbol{e}_r\phi(r,\theta,z,t)\} + \boldsymbol{\nabla}\times\{\boldsymbol{e}_r\psi(r,\theta,z,t)\}, \tag{2.8a}$$

$$\widetilde{\boldsymbol{b}}(r,\theta,z,t) = \boldsymbol{\nabla}\times\boldsymbol{\nabla}\times\{\boldsymbol{e}_r f(r,\theta,z,t)\} + \boldsymbol{\nabla}\times\{\boldsymbol{e}_r g(r,\theta,z,t)\}, \tag{2.8b}$$

where $\overline{v}(r)$ and $\overline{w}(r)$ are the azimuthal and axial components, respectively, of the mean velocity field. It can be easily shown that no mean magnetic field can be generated in the inductionless limit. The poloidal and toroidal potentials ϕ, f and ψ, g introduced in (2.8*a*) and (2.8*b*) uniquely determine the physical hydrodynamic and magnetic perturbation fields $\widetilde{\boldsymbol{v}}$ and $\widetilde{\boldsymbol{b}}$, except for the obvious gauge freedom (addition of a constant).

The coherent flows addressed in this work are mixed modes resulting from the nonlinear interaction of pairs of spiral waves propagating in the θ–z plane. Following Deguchi & Altmeyer (2013), we introduce the two phase variables

$$\xi_1 = m_1\theta + k_1 z - c_1 t, \quad \xi_2 = m_2\theta + k_2 z - c_2 t, \tag{2.9a,b}$$

describing the wavefronts of the two interacting spirals, which propagate at speeds c_1 and c_2, and whose azimuthal and axial wavenumbers are the integer (m_1, m_2) and real (k_1, k_2) constant pairs, respectively. Travelling mixed modes resulting from the nonlinear interaction of spiral modes of the form given by (2.9) are naturally represented on doubly 2π-periodic parallelogram domains of the form

$$(r,\xi_1,\xi_2) \in [r_i, r_o]\times[0,2\pi]\times[0,2\pi], \tag{2.10}$$

unwrapped and outlined in figure 2 for any given value of the radial coordinate. Straightforward algebraic manipulation shows that any function of ξ_1 and ξ_2 can also be written in terms of $\theta - c_\theta t$ and $z - c_z t$ with

$$c_\theta = \frac{k_2c_1 - k_1c_2}{m_2k_1 - m_1k_2}, \quad c_z = \frac{m_2c_1 - m_1c_2}{m_2k_1 - m_1k_2}. \tag{2.11}$$

The solutions sought are therefore travelling waves propagating both azimuthally and axially with the phase speeds c_θ and c_z just given, respectively.

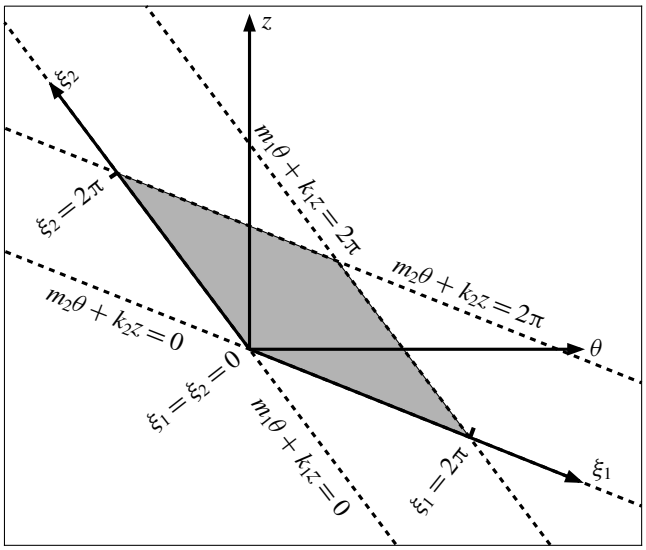

FIGURE 2. Sketch of the parallelogram domain introducing the new variables (ξ_1, ξ_2) that replace the usual azimuthal and axial coordinates (θ, z).

The initial–boundary value problem (2.7*a*)–(2.7*b*) is reformulated in the new phase variables assuming 2π-periodicity of the toroidal and poloidal potentials introduced in (2.8*a*)–(2.8*b*):

$$[\phi, \psi, f, g](r, \xi_1 + 2\pi, \xi_2) = [\phi, \psi, f, g](r, \xi_1, \xi_2 + 2\pi) = [\phi, \psi, f, g](r, \xi_1, \xi_2). \quad (2.12)$$

The potentials are then discretised using spectral Fourier expansions of the form

$$\phi(r, \xi_1, \xi_2) = \sum_{n_1, n_2} \widehat{\phi}_{n_1 n_2}(r) \mathrm{e}^{\mathrm{i}(n_1 \xi_1 + n_2 \xi_2)}, \quad \psi(r, \xi_1, \xi_2) = \sum_{n_1, n_2} \widehat{\psi}_{n_1 n_2}(r) \mathrm{e}^{\mathrm{i}(n_1 \xi_1 + n_2 \xi_2)}, \quad (2.13a)$$

$$f(r, \xi_1, \xi_2) = \sum_{n_1, n_2} \widehat{f}_{n_1 n_2}(r) \mathrm{e}^{\mathrm{i}(n_1 \xi_1 + n_2 \xi_2)}, \quad g(r, \xi_1, \xi_2) = \sum_{n_1, n_2} \widehat{g}_{n_1 n_2}(r) \mathrm{e}^{\mathrm{i}(n_1 \xi_1 + n_2 \xi_2)}, \quad (2.13b)$$

where the Fourier radial functions $\widehat{\phi}_{n_1 n_2}(r)$, $\widehat{\psi}_{n_1 n_2}(r)$, $\widehat{f}_{n_1 n_2}(r)$ and $\widehat{g}_{n_1 n_2}(r)$ are identically zero for $n_1 = n_2 = 0$. For $n_1 \neq 0$ or $n_2 \neq 0$, these radial functions are suitable expansions of modified Chebyshev polynomials satisfying homogeneous no-slip boundary conditions at the inner and outer cylinder walls:

$$\phi = \partial_r \phi = \psi = \overline{v} = \overline{w} = 0. \quad (2.14)$$

The hydrodynamic radial functions are thus

$$\widehat{\phi}_{n_1 n_2}(r) = \sum_l X^{(1)}_{l n_1 n_2} (1 - y^2)^2 T_l(y), \quad \widehat{\psi}_{n_1 n_2}(r) = \sum_l X^{(2)}_{l n_1 n_2} (1 - y^2) T_l(y), \quad (2.15a)$$

$$\overline{v}(r) = \sum_l X^{(1)}_{l 00} (1 - y^2) T_l(y), \quad \overline{w}(r) = \sum_l X^{(2)}_{l 00} (1 - y^2) T_l(y), \quad (2.15b)$$

where $T_l(y)$ is the lth Chebyshev polynomial and $y \equiv 2(r - r_i) - 1 \in [-1, 1]$ is the rescaled radial coordinate. Similarly, the magnetic radial functions are expanded

employing Chebyshev polynomials modified to satisfy perfectly insulating conditions:

$$\widehat{f}_{n_1n_2}(r) = \sum_l X^{(3)}_{ln_1n_2}\{(1-y^2)T_l(y) + \alpha_{ln_1n_2} + \beta_{ln_1n_2}y\}, \tag{2.16a}$$

$$\widehat{g}_{n_1n_2}(r) = \gamma_{n_1n_2}(r)\widehat{f}_{n_1n_2}(r) + \sum_l X^{(4)}_{ln_1n_2}(1-y^2)T_l(y). \tag{2.16b}$$

A detailed description of the coefficients $\alpha_{ln_1n_2}$ and $\beta_{ln_1n_2}$ and of the function $\gamma_{n_1n_2}(r)$ can be found in appendix A.

For computational purposes, the Fourier–Chebyshev expansions (2.15*a*)–(2.16*b*) are truncated at $l = L$, $|n_1| = N_1$ and $|n_2| = N_2$. After substituting the truncated expansions into system (2.7*a*)–(2.7*b*), these are then evaluated at the Chebyshev nodes

$$y = \cos\left(\frac{l+1}{L+2}\pi\right), \quad l = 1, \ldots, L. \tag{2.17}$$

This procedure leads to a system of nonlinear algebraic equations of the form

$$0 = \boldsymbol{L}_1 \begin{bmatrix} X^{(1)}_{ln_1n_2} \\ X^{(2)}_{ln_1n_2} \end{bmatrix} + H^2 \boldsymbol{L}_2 \begin{bmatrix} X^{(3)}_{ln_1n_2} \\ X^{(4)}_{ln_1n_2} \end{bmatrix} + [X^{(1)}_{ln_1n_2}, X^{(2)}_{ln_1n_2}]\boldsymbol{N} \begin{bmatrix} X^{(1)}_{ln_1n_2} \\ X^{(2)}_{ln_1n_2} \end{bmatrix}, \tag{2.18a}$$

$$\boldsymbol{L}_3 \begin{bmatrix} X^{(1)}_{ln_1n_2} \\ X^{(2)}_{ln_1n_2} \end{bmatrix} = \boldsymbol{L}_4 \begin{bmatrix} X^{(3)}_{ln_1n_2} \\ X^{(4)}_{ln_1n_2} \end{bmatrix}. \tag{2.18b}$$

Here $\boldsymbol{L}_1$, $\boldsymbol{L}_2$, $\boldsymbol{L}_3$ and $\boldsymbol{L}_4$ are matrices, and $\boldsymbol{N}$ is a third-order tensor, whose form is unchanged from the purely hydrodynamic case. Isolating the magnetic unknowns by solving the linear system (2.18*b*) and substituting into (2.18*a*) yields a nonlinear system of equations for the hydrodynamic unknowns $X^{(1)}_{ln_1n_2}$ and $X^{(2)}_{ln_1n_2}$:

$$0 = (\boldsymbol{L}_1 + H^2\boldsymbol{L}_2\boldsymbol{L}_4^{-1}\boldsymbol{L}_3) \begin{bmatrix} X^{(1)}_{ln_1n_2} \\ X^{(2)}_{ln_1n_2} \end{bmatrix} + [X^{(1)}_{ln_1n_2}, X^{(2)}_{ln_1n_2}]\boldsymbol{N} \begin{bmatrix} X^{(1)}_{ln_1n_2} \\ X^{(2)}_{ln_1n_2} \end{bmatrix}. \tag{2.19}$$

Matrix $\boldsymbol{L}_1$ depends implicitly on the unknown speeds c_1 and c_2 appearing in (2.9), which correspond to the co-moving reference frame in which the mixed mode remains a steady solution. Since these two speeds are also unknown, two additional phase-locking conditions are required to lift the rotational/travelling degeneracy of solutions from the system of equations. Similarly, system (2.19) must also be complemented with an additional constraint to allow determination of the unknown axial pressure gradient G required to ensure the zero-mass-flux condition. The nonlinear system (2.19), along with the aforementioned constraints, is solved numerically using Newton's method. The hydrodynamic part of the code is identical to that used in Deguchi & Altmeyer (2013), and more detailed documentation of the computational methodology can be found in Deguchi & Nagata (2011).

For the purely hydrodynamic problem, we have also computed and continued in parameter space the bifurcating mixed modes using an independent numerical formulation. This alternative methodology is based on a solenoidal Petrov–Galerkin scheme described in Meseguer *et al.* (2007), suitably adapted to the annular parallelogram domain (2.10). In this formulation, the solenoidal velocity perturbation

$\widetilde{\boldsymbol{v}}$ is approximated by means of a spectral expansion $\widetilde{\boldsymbol{v}}_s$ of order N in $\xi_1 = m_1\theta + k_1 z$, order L in $\xi_2 = m_2\theta + k_2 z$, and order M in r:

$$\widetilde{\boldsymbol{v}}_s(r, \xi_1, \xi_2, t) = \sum_{n_1,\, n_2,\, m} a_{n_1 n_2 m}(t)\, \boldsymbol{\Phi}_{n_1 n_2 m}(r, \xi_1, \xi_2). \tag{2.20}$$

The $\boldsymbol{\Phi}_{n_1 n_2 m}$ are trial bases of solenoidal vector fields of the form

$$\boldsymbol{\Phi}_{n_1 n_2 m}(r, \xi_1, \xi_2) = \mathrm{e}^{\mathrm{i}(n_1\xi_1 + n_2\xi_2)}\boldsymbol{v}_{n_1 n_2 m}(r), \tag{2.21}$$

where the radial fields $\boldsymbol{v}_{n_1 n_2 m}(r)$ are suitably constructed to satisfy $\boldsymbol{\nabla}\cdot\boldsymbol{\Phi}_{n_1 n_2 m} = 0$. Since $\widetilde{\boldsymbol{v}}_s$ represents the perturbation of the velocity field, it must therefore vanish at the inner ($r = r_i$) and outer ($r = r_o$) walls of the cylinders. Therefore, $\boldsymbol{v}_{n_1 n_2 m}$ must also satisfy homogeneous boundary conditions:

$$\boldsymbol{v}_{n_1 n_2 m}(r_i) = \boldsymbol{v}_{n_1 n_2 m}(r_o) = \boldsymbol{0}. \tag{2.22}$$

These radial fields are built from suitable expansions of modified Chebyshev polynomials. After introducing the expansion

$$\widetilde{\boldsymbol{v}}_s(r, \xi_1, \xi_2, t) = \sum_{n_1,\, n_2,\, m} a^{TW}_{n_1 n_2 m}\mathrm{e}^{\mathrm{i}n_1(\xi_1 - c_1 t)}\mathrm{e}^{\mathrm{i}n_2(\xi_2 - c_2 t)}\boldsymbol{v}_{n_1 n_2 m}(r) \tag{2.23}$$

into the hydrodynamic equations, the weak formulation described in Meseguer *et al.* (2007) leads to a system of nonlinear algebraic equations for the unknown coefficients $a^{TW}_{n_1 n_2 m}$, similar to (2.19), to which the zero-mass-flux constraint is also imposed. The resulting system of equations were solved using a matrix-free Newton–Krylov method (Kelley 2003). The converged nonlinear solutions were then continued in parameter space using pseudo-arclength continuation schemes (Kuznetsov 2004). To avoid cluttering the paper with unnecessary detail and because of the intricacies that are inherent to the numerical approach undertaken, a detailed description of the method will be published separately.

In the classic rectangular domain, the Petrov–Galerkin solenoidal discretisation has been successfully used in the numerical approximation of transitional flows in cylindrical geometries (Mellibovsky & Meseguer 2006) and in the computation of subcritical rotating waves in annular domains (Deguchi *et al.* 2014). In the latter study, the code was cross-checked against the codes used in the aforementioned Deguchi & Nagata (2011) and Deguchi & Altmeyer (2013). In § 4, the favourable comparison of the nonlinear results produced by the annular-parallelogram extension of the two independent codes based on completely different formulations serves as an unbeatable procedure for code validation. The results for the linear magnetic part of (2.19) has instead been checked against the linear results by Hollerbach *et al.* (2010) in the next section.

For a travelling wave solution, the absolute values of torque on the inner and outer cylinders are always equal and represent the angular momentum transport. The torque on the inner cylinder can be computed indistinctly as

$$T \equiv \{-r^3\partial_r(r^{-1}\overline{v})\}|_{r=r_i} = -\{r^3\partial_r(r^{-1}\overline{v})\}|_{r=r_o}, \tag{2.24}$$

while the torque on the outer cylinder is $-T$ to keep the inner and outer cylinders rotating at constant speeds. We have characterised all Newton-converged nonlinear solutions throughout by their torque normalised by the corresponding base-flow torque $T_b = \{-r^3\partial_r(r^{-1}v_b)\}|_{r=r_i} = -\{r^3\partial_r(r^{-1}v_b)\}|_{r=r_o}$:

$$\tau = \frac{T}{T_b} = \left.\frac{\partial_r(r^{-1}\overline{v})}{\partial_r(r^{-1}v_b)}\right|_{r=r_i,r_o}, \tag{2.25}$$

such that the normalised torque τ is unity for laminar circular Couette flow.

3. The anticyclonic regime

Let us consider the normalised base magnetic fields

$$B_b(r) = \frac{r_i}{r}, \quad C_b(r) = \delta, \tag{3.1a,b}$$

to reproduce both the axisymmetric HMRI and non-axisymmetric AMRI modes found in the anticyclonic regime by Hollerbach *et al.* (2010). The constant δ represents the strength of the axial magnetic field relative to the azimuthal field, which is induced by a current running through the inner cylinder, parallel to its axis.

Following Hollerbach *et al.* (2010), we fix the rotation ratio to $\widehat{\mu} = \Omega_o^*/\Omega_i^* = R_o\eta/R_i = 0.26$. Note that for the anticyclonic regime $\widehat{\mu}$ must remain in the interval [0.25, 1], where the lower bound corresponds to the Rayleigh line $\widehat{\mu} = \eta^2 = 0.25$, while the upper bound embodies solid-body rotation. The quasi-Keplerian rotation regime frequently used in astrophysical studies on accretion disks is characterised by $\widehat{\mu} = \eta^{3/2} \approx 0.35$. This rotation law results from applying Kepler's law to both the inner and outer cylinder angular velocities, which results in a fair approximation of a strictly Keplerian flow across the gap. The choice $\widehat{\mu} = 0.26$, used in the experimental demonstration of AMRI by Seilmayer *et al.* (2014), places the flow in the anticyclonic regime but very close to the boundary set by the Rayleigh line. Liu *et al.* (2006) used a locally periodic approach to show that there is a limiting value $\widehat{\mu} \approx 0.3$ above which HMRI halts, and the analysis was later extended by Kirillov, Stefani & Fukumoto (2012) to AMRI. To what extent this limit is actually relevant to fully cylindrical flows is, however, still under debate (see Rüdiger & Hollerbach 2007; Child, Kersalé & Hollerbach 2015). The radius ratio of the cylinders is set to $\eta = 0.5$. For this particular value of η, our definitions of R_i and H become identical to the hydrodynamic Reynolds number and the Hartmann number, respectively, used by Hollerbach *et al.* (2010). Most importantly, the parameter range studied there is feasible in the PROMISE experiments, where both axisymmetric (Rüdiger *et al.* 2006; Stefani *et al.* 2006, 2007) and non-axisymmetric (Seilmayer *et al.* 2014) modes were actually realised. Travelling waves similar to those predicted in the numerical studies were indeed observed. These waves originate from absolute instability (even global), rather than mere convective, as shown by the comprehensive experimental study on HMRI by Stefani *et al.* (2009).

Having fixed $\widehat{\mu}$ and η, we have performed a linear stability analysis of the base flow by exploring the eigenspectrum of the linearised hydromagnetic equations for combinations of R_i, H, δ and azimuthal–axial pairs (m, k) of the associated spiral eigenfunctions. We started by reproducing the neutral curves in the H–R_i plane for $\delta = 0$, 0.02, 0.03, 0.04, 0.05, and for the optimal axial wavenumber $k > 0$ that maximises the growth rate. For $\delta = 0$, the instability originates from the symmetric spirals with opposite tilt ($m = \pm 1$). The primal effect of finite δ is the breaking of that reflection symmetry. Moreover, the axisymmetric mode ($m = 0$) emerges and for sufficiently large $\delta \approx 0.05$ it dominates over the non-axisymmetric modes. The non-axisymmetric modes are of AMRI origin, while the axisymmetric mode only becomes dominant for distinctly helical fields, which leaves a finite range of δ where all three modes compete. The neutral curves we have computed are in perfect agreement with figure 3 of Hollerbach *et al.* (2010), where it was already pointed out that, for $\delta \approx 0.04$, the critical Reynolds numbers of all three modes become comparable. Here we have identified that at $\delta = 0.0413$ there is a point where all three modes become neutral simultaneously, as clearly shown in figure 3.

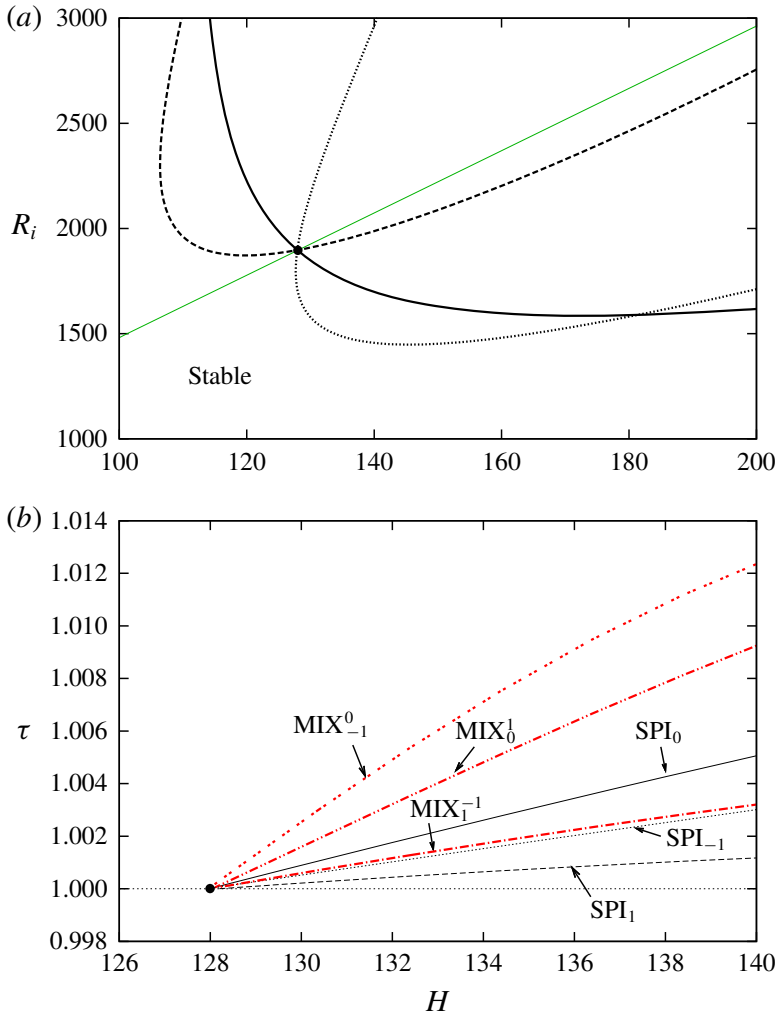

FIGURE 3. Linear stability analysis and continuation of bifurcated nonlinear solution branches in the anticyclonic regime for $(\delta, \eta) = (0.0413, 0.5)$. (*a*) Neutral stability curves along the line $R_o = 0.26R_i/\eta$ (black curves) for modes $m = 0$ (solid) and $m = \pm 1$ (dashed for $+1$, dotted for -1). Wavenumber k is the one that maximises growth rate. The black circle indicates the triple critical point at $(H, R_i) = (128, 1896)$. (*b*) Bifurcation diagram along $R_i = (1896/128)H$ (green line in panel *a*). The black circle corresponds again to the triple-critical point, whence three spiral (SPI_0, $\mathrm{SPI}_{\pm 1}$; solid, dashed and dotted black lines) and three mixed (MIX^{-1}_1, MIX^0_1, MIX^{-1}_0; solid, dashed and dotted red lines) modes are issued.

For the sake of clarity, we shall focus on the computation and continuation of nonlinear solutions along the straight line across parameter space $R_i = (1896/128)H$ (green solid line in figure 3*a*) that passes through the triple critical point at $(H, R_i) = (128, 1896)$. Figure 3(*b*) depicts the bifurcation diagram corresponding to the six different nonlinear solution branches, as characterised by torque as a function of the Hartmann number. At the triple critical point, the three eigenmodes, $(m, k) = (0, 5.672)$, $(m, k) = (1, 4.672)$ and $(m, k) = (-1, 2.818)$, become neutral simultaneously. As anticipated by weakly nonlinear analysis, bifurcation of various mixed modes is therefore expected. The Newton method described in § 2 does indeed converge to one or another of the nonlinear pure- or mixed-mode solutions when a suitably weighted superposition of the three neutral eigenmodes is taken as an initial guess. Solutions have initially been computed in this way in the close neighbourhood

Figure no.	Abbreviation	Solution type	(m_1, k_1)	(m_2, k_2)
3(*b*)	SPI_0	Spiral	(0, 5.672)	N/A
	SPI_1	Spiral	(1, 4.672)	N/A
	SPI_{-1}	Spiral	(−1, 2.818)	N/A
	MIX_0^{-1}	Mixed mode	(0, 5.672)	(−1, 2.818)
	MIX_1^{0}	Mixed mode	(1, 4.672)	(0, 5.672)
	MIX_1^{-1}	Mixed mode	(1, 4.672)	(−1, 2.818)
7(*a*)	SPI	Spiral	(1, 40.6)	N/A
	$\mathrm{SPI}_{\mathrm{D17}}$	Spiral	(1, 1.002)	N/A
	RIB	Ribbon	(1, 40.6)	(−1, 40.6)
	$\mathrm{RIB}_{\mathrm{D17}}$	Ribbon	(1, 1.002)	(−1, 1.002)
	MIX_+	Mixed mode	(1, 40.6)	(1, 1.002)
	MIX_-	Mixed mode	(1, 40.6)	(−1, 1.002)
7(*b*)	$\mathrm{SPI}_{\mathrm{D17}}$	Spiral	(1, 0.616)	N/A
	$\mathrm{SPI}_{\mathrm{MRI}}$	Spiral	(1, 1.984)	N/A
	$\mathrm{RIB}_{\mathrm{D17}}$	Ribbon	(1, 0.616)	(−1, 0.616)
	$\mathrm{RIB}_{\mathrm{MRI}}$	Ribbon	(1, 1.984)	(−1, 1.984)
	MIX_+	Mixed mode	(1, 1.984)	(1, 0.616)
	MIX_-	Mixed mode	(1, 1.984)	(−1, 0.616)

TABLE 1. Abbreviations used to describe the various nonlinear solution branches. Note that SPI_0 is a zero-pitch spiral, and therefore a toroidal-vortex-pair solution.

of the triple critical point and then continued as a function of H using either natural or pseudo-arclength continuation algorithms. Three of the solution branches, converged from single-mode initial guesses fed into the Newton method, correspond to helically invariant travelling spiral waves (black curves in figure 3*b*). These solutions we have dubbed as SPI_m, with the subscript m (solid black line for $m = 0$, dashed for $m = 1$, dotted for $m = -1$) denoting the azimuthal wavenumber of the mode (see table 1). All three branches bifurcate supercritically from the base laminar flow. Since these solutions can be computed in the usual rectangular domain using regular coordinates (θ, z), we omit a detailed analysis.

Suitable proportions of the weights applied to the critical eigenmodes in generating the initial seeds for the Newton method have allowed computation of all three possible mixed-mode nonlinear solution branches (red curves in figure 3*b*). These mixed modes have been labelled as $\mathrm{MIX}_{m_1}^{m_2}$, with the sub- and superscripts representing the azimuthal wavenumber of the two interacting modes, and duly reported in table 1. As mentioned earlier, these mixed modes can only be identified using an appropriate annular-parallelogram domain, as the superposition of the two modes does not fit any rectangular domain of affordable size.

All three mixed-mode branches bifurcate supercritically. A very remarkable feature of these mixed modes is that some of them have larger torque than the spirals. This aspect is of special relevance to the study of astrophysical accretion disks, as it is a paramount requirement for the large outward angular momentum flux that is believed to be the key to the observed rate of inward mass accretion. The MIX_{-1}^{0} mode possesses the largest torque of all mixed modes, as is also clear from the azimuthal mean flow distortion shown in figure 4 for $H = 140$, $(R_i, R_o) \approx (2074, 1078)$. Figure 5 shows the corresponding total azimuthal vorticity distribution of the three mixed

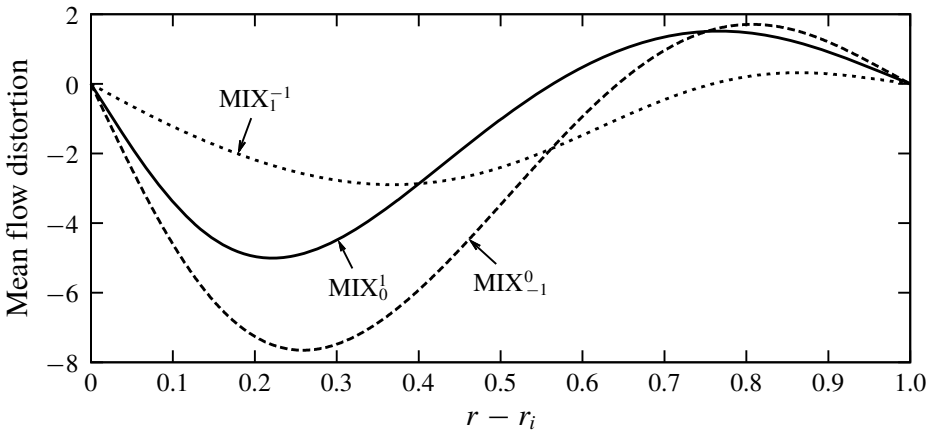

FIGURE 4. Azimuthal mean flow distortion $(\overline{v} - v_b)$ of the three different mixed modes shown in figure 3(*b*) for $H = 140$, and $(R_i, R_o) \approx (2074, 1078)$.

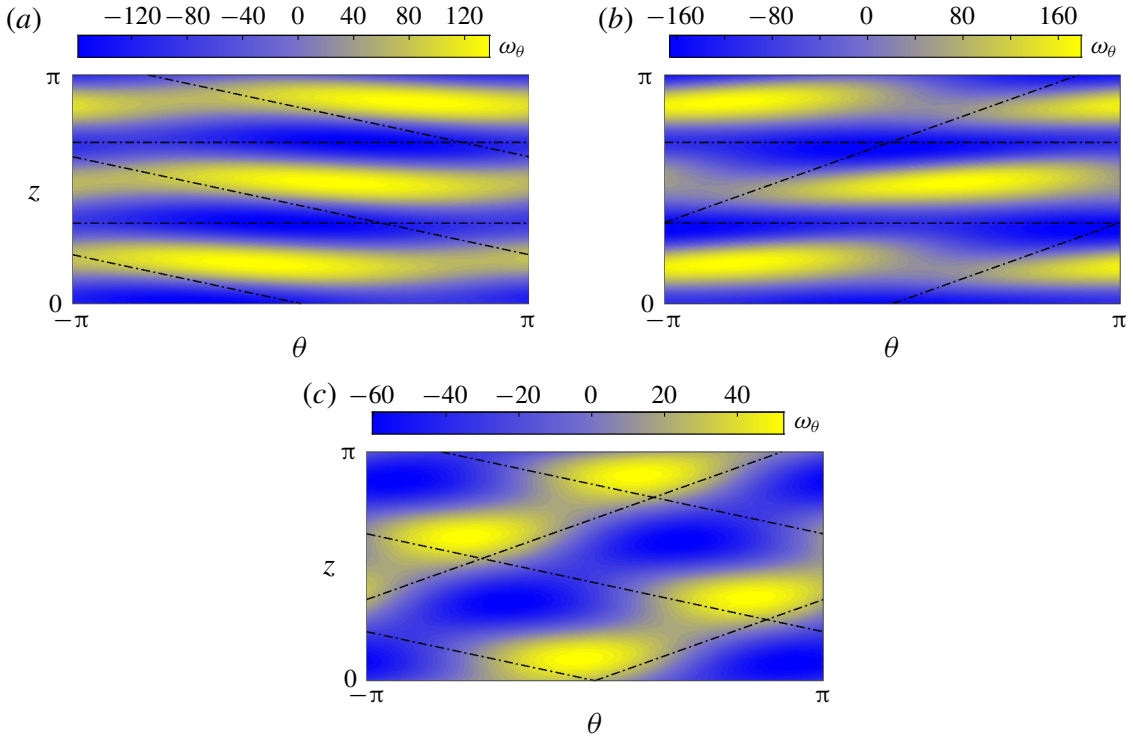

FIGURE 5. Colour maps of the total azimuthal vorticity $(\omega_\theta = \partial_z u - \partial_r w)$ distribution at the mid-radial-plane $r = r_i + 0.5$ of the three mixed-mode MRI solutions: (*a*) MIX_1^0, (*b*) MIX_{-1}^0 and (*c*) MIX_{-1}^1.

modes, represented through θ–z plane colour maps at mid-gap $r = r_i + 0.5$. As expected, mode MIX_{-1}^0 has the strongest flow field perturbation, clearly reflected in the colour bar range of the panels. The visualisations shown in figure 5(*a*) and (*b*) for MIX_0^1 and MIX_{-1}^0, respectively, are reminiscent of wavy Taylor vortex flow (see e.g. Andereck *et al.* (1986)) except that the patterns are tilted and wavy vortex pairs accumulate an azimuthal phase shift as they pile up in the axial direction. The reason for this is that one of its constituents is a zero-pitch spiral, which corresponds to a toroidal-vortex-pair solution much like Taylor vortices, while the superposition of a spiral mode generates the tilted azimuthal modulation. Meanwhile, the structure

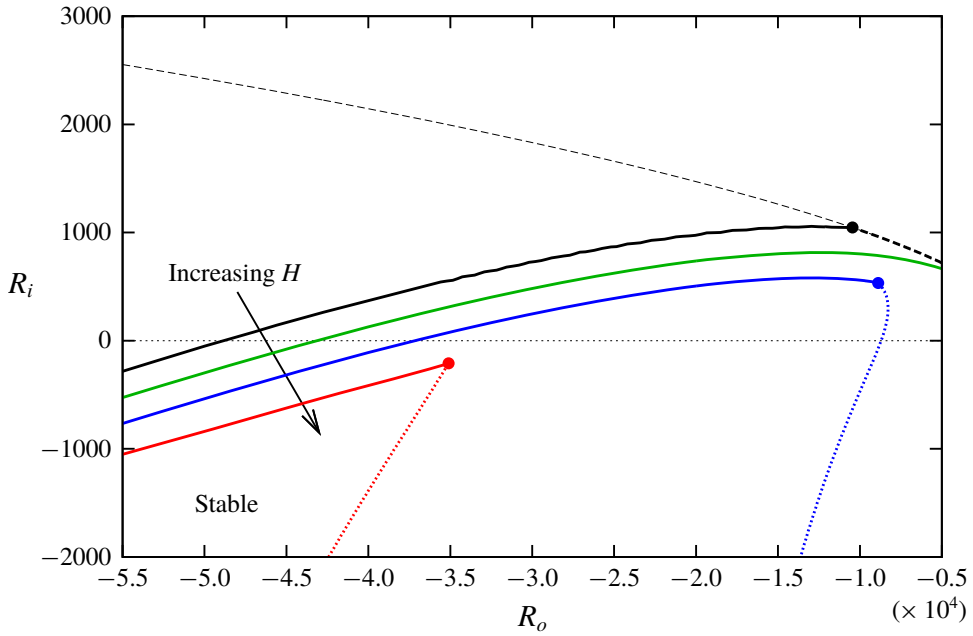

FIGURE 6. Neutral curves for $H = 0, 40, 60, 84$ (black, green, blue, red, respectively) and $\eta = 0.1$. The wavenumber pairs (k, m) are optimised to detect the most unstable eigenvalue. The neutral curve for the classical non-axisymmetric hydrodynamic mode (dashed black) is shown alongside those for the D17 mode (solid black) and the MRI mode (dotted). While m is large and obeys the asymptotic result by Deguchi (2016) for the classical neutral curve, the D17 and MRI neutral curves have typically $m = \pm 1$. Bicritical points, where direct bifurcation of mixed-mode solution branches are expected, are indicated with filled circles.

of the MIX_1^{-1} mode shown in figure 5(*c*) is evocative of the wavy spiral solution found in the hydrodynamic studies by Altmeyer & Hoffmann (2010) and Deguchi & Altmeyer (2013).

4. From counter-rotation to the cyclonic super-rotation regime

In this section we focus our attention on the bifurcations arising on the left half-plane of figure 1, as some of the instabilities carry on to the super-rotation regime. For $\eta = 0.1$, figure 6 outlines the neutral curves obtained from linear stability analyses corresponding to different levels of magnetisation. We begin our analysis by first focusing on the purely hydrodynamic case in the absence of magnetic effects. Shown in figure 6 are the classical neutral curve (dashed black) alongside the neutral curve for the D17 mode (solid black), recently discovered by Deguchi (2017) through linear stability analysis.

Along the classical boundary, the critical value of R_i increases with $|R_o|$, which is consistent with extensive numerical evidence as well as physical insights and the large-Reynolds-number formal asymptotic result (Esser & Grossmann 1996; Deguchi 2016; Grossmann *et al.* 2016). As a consequence, the neutral curve, which corresponds to a non-axisymmetric leading mode with large m (a spiral), cannot be continued across the line $R_i = 0$ into the super-rotation regime.

In contrast, the neutral curve for the D17 mode, typically with $m = \pm 1$, does indeed extend to the cyclonic super-rotation regime. The reason for choosing such a low value of the radius ratio ($\eta = 0.1$) follows from the observation that the curve shifts to very high counter-rotation rates as η is increased and narrower gaps are considered. For instance, taking $R_i = 0$ and $\eta = 5/7$ pushes the critical R_o value to

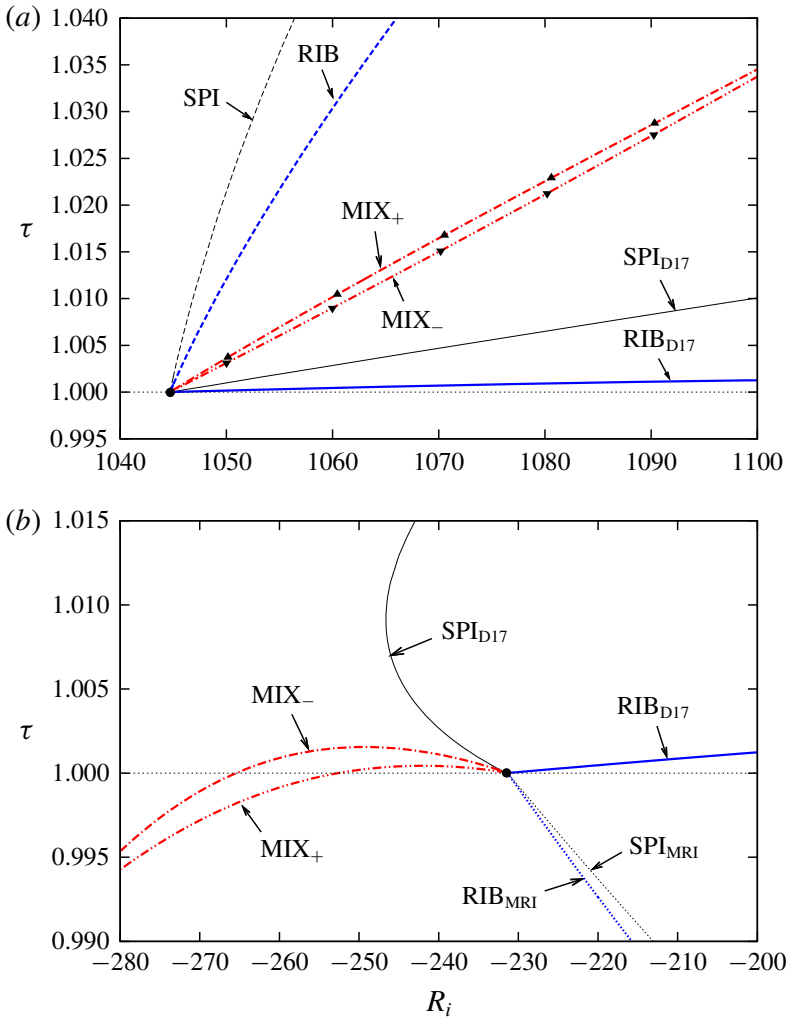

FIGURE 7. Bifurcation diagrams of spirals, ribbons and mixed nonlinear modes in super- and counter-rotation configurations. (*a*) Purely hydrodynamic case, in counter-rotation with $R_o = -10\,434$ and $H = 0$. The black circle indicates the linear bicritical point at $R_i = 1045$. A bunch of mixed-mode solutions computed with the alternative Petrov–Galerkin code are marked with triangles. (*b*) Magnetised case in the super-rotation regime with $R_o = -35\,150$ and $H = 84$. The bicritical point at $R_i = -231.5$ is indicated with a filled black circle.

$O(10^7)$, whereas for $\eta = 0.1$ it remains within order $O(10^4)$. In figure 6, the classical stability threshold (dashed black) and the new one set by the neutral curve of the D17 mode (solid black) meet at a bicritical point (black filled circle) located at $(R_i, R_o) \approx (1045, -10\,434)$, with associated critical wavenumbers $(m_1, k_1) = (1, 40.6)$ and $(m_2, k_2) = (1, 1.102)$, respectively. The critical axial wavenumbers k_1 and k_2 associated with either mode differ significantly, which explains why the latter, mode D17, escaped detection for so long. The asymptotic theory provided by Deguchi (2016) formally proved that the critical axial wavenumber of the classical mode gets asymptotically large for increasing Reynolds numbers, while that for the D17 mode seems to be insensitive to Reynolds-number variations.

The various nonlinear solution branches that bifurcate from the bicritical point (black filled circle in figure 6) are shown in figure 7(*a*). All branches bifurcate supercritically. The black curves correspond to the spiral solutions for the classical spiral mode (SPI, dashed) and the D17 mode ($\mathrm{SPI_{D17}}$, solid). The structure of the single-mode solutions, the nonlinear spirals, are qualitatively identical to the linear

neutral mode (see Deguchi 2017). Since the system is symmetric with respect to axial reflections ($z \to -z$), spiral modes become neutral in pairs, with exactly opposite pitch. As a result, there are actually four modes that simultaneously become neutral at the linear bicritical point (the black filled circle in figure 7*a*). Consequently, there exist six mixed modes arising from all possible combinations of modes taken in pairs. Two of them merely correspond to ribbon solutions (blue curves in figure 7*a*), labelled as RIB (dashed, SPI–SPI interaction) and $\mathrm{RIB}_{\mathrm{D17}}$ (solid, $\mathrm{SPI}_{\mathrm{D17}}$–$\mathrm{SPI}_{\mathrm{D17}}$ interaction), and listed in table 1. While ribbon solutions can be computed in a rectangular domain, all other mixed modes require the use of the annular-parallelogram domain. In fact, only two of the four remaining modes actually require computation, as the other two can be easily obtained from simple z reflection and, since the torque is invariant under this symmetry operation, the solution branches are exactly coincident. The branches corresponding to these mixed-mode solutions are shown in red in figure 7(*a*). The branch labelled as MIX_{+} originates from the interaction of two modes with pitches of the same sign, while the one labelled MIX_{-} arises from the nonlinear coupling of modes with opposite sign, as reported in table 1.

All hydrodynamic results reported in this work and initially computed with a code based on the hydromagnetic-potential formulation (2.13) have been reproduced using the independently developed solenoidal Petrov–Galerkin parallelogram formulation (2.20). A few nonlinear solutions at selected values of the parameters have been chosen and indicated with triangles in figure 7(*a*) to convey the excellent qualitative agreement between the two methods employed for the computations. Quantitative comparison shows that the torque discrepancy stays below 0.06 % for all the purely hydrodynamic nonlinear mixed-mode solutions computed. Figure 8(*a*) represents the azimuthal mean flow distortion for the mixed modes at $(R_i, R_o) = (1100, -10\,434)$. The distortion is the most significant in the vicinity of the inner cylinder, which indicates that the perturbation is strongest in this region. For the same values of the parameters, figure 9 shows azimuthal vorticity colour maps for both mixed modes on an unwrapped radial plane at $r = r_i + 0.05$. The observed flow structure is very different from any of the mixed-mode solutions reported by Deguchi & Altmeyer (2013). The observed small–large scale interaction reminds one of the stripe pattern that is characteristic of intermittent spiral turbulence (Dong 2009; Meseguer *et al.* 2009). While the Reynolds numbers and the gap are too large to claim there exists any relation between the mixed modes presented here and spiral turbulence, the similarity of the patterns indicates that spiral turbulence might indeed be supported by mixed-mode solutions of very different pitches as the ones investigated here in a completely different setting.

Now we turn our attention to the magnetised problem, where we will impose an external magnetic field with a strictly azimuthal orientation. For the MRI studies in an annulus, the azimuthal base magnetic field is typically the weighted superposition of r^{-1} and r components. The respective coefficients can be tuned by an appropriate uniform current imposed within the inner and outer cylinders. Rüdiger *et al.* (2016, 2018*b*) considered two extreme cases: $B_b(r) \propto r^{-1}$ (i.e. there is no current between the cylinders) and $B_b(r) \propto r$ (i.e. the axial current is homogeneous between the cylinders). The latter also has the alternative name z pinch, and is known to become unstable for sufficiently large Hartmann number even with both cylinders at rest (Tayler 1957). As the Taylor instability does not exist for the current-free case, the behaviour of the neutral curve for small Reynolds numbers must necessarily be quite different from that for the homogeneous current case. Rüdiger *et al.* (2016, 2018*b*) found that, for $\eta \gtrsim 0.8$, the neutral curves behave qualitatively alike in both cases when Reynolds numbers

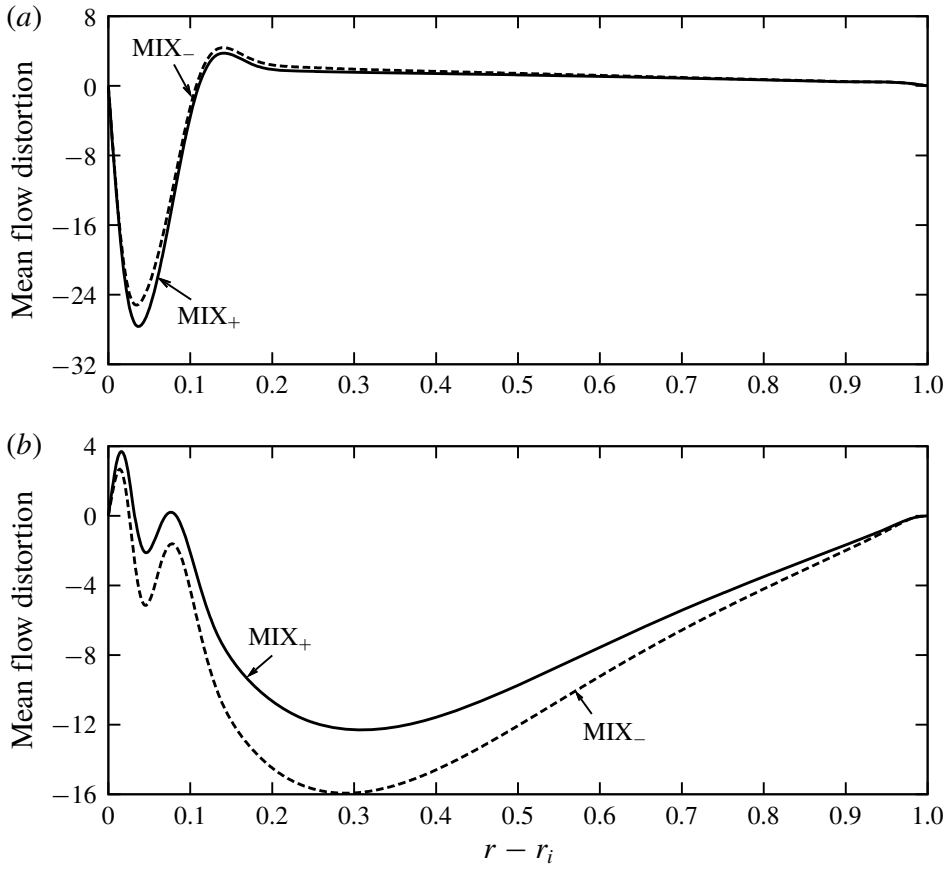

FIGURE 8. Azimuthal mean flow distortion ($\overline{v} - v_b$) of mixed-mode solutions. (*a*) Purely hydrodynamic case at $R_i = 1100$ from figure 7(*a*). (*b*) Magnetised case at $R_i = -280$ and $H = 84$ from figure 7(*b*).

are moderately large, thereby suggesting that super-AMRI is rather insensitive to the choice of the azimuthal magnetic field profile.

We have confirmed that the D17 mode is stabilised by both the current-free and the z-pinch cases. Nonetheless, when the two azimuthal magnetic field components exist simultaneously, the D17 mode can be destabilised, as clearly illustrated by the behaviour of the neutral stability curves in figure 6. Here the specific magnetic field profile used is

$$B_b(r) = \frac{r_i}{r} - \frac{r}{r_o}, \qquad C_b(r) = 0. \tag{4.1a,b}$$

Although the arguments by Rüdiger *et al.* (2016, 2018*b*) for the current-free case may not be applicable to the large gap $\eta = 0.1$ we tackle here, an MRI does indeed arise when a current is considered. This phenomenon had already been anticipated by a locally periodic approach (see Liu *et al.* 2006; Kirillov, Stefani & Fukumoto 2014), but the nature of the method used renders the approximation rather crude in view of the not-so-large critical wavenumbers we encounter here. As the Hartmann number is increased, the super-AMRI mode eventually takes over the classical mode, and hence changes the character of the bicritical point. In view of figure 6 at $H = 60$, the double critical point is already the result of the interaction of the D17 and the super-AMRI modes. The base flow remains stable within the region bounded by their respective stability thresholds. Along the combined neutral curve, the critical axial wavenumber experiences a discontinuous leap across the bicritical point, whence it must be inferred that the two instability mechanisms are indeed distinct. By further

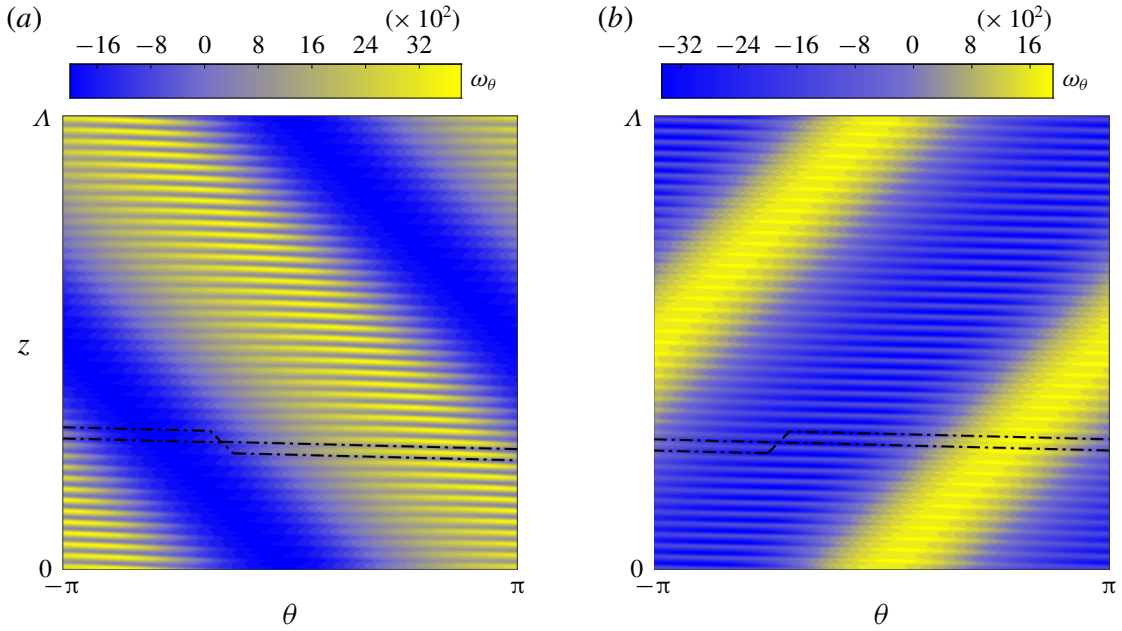

FIGURE 9. Visualisation of the total azimuthal vorticity ($\omega_\theta = \partial_z u - \partial_r w$) at $r = r_i + 0.05$ for the purely hydrodynamic mixed-mode solutions at $R_i = 1100$ in figure 7(*a*). Here $\Lambda = 2\pi/1.002 \approx 6.27$: (*a*) MIX_- and (*b*) MIX_+. The corresponding mean flow distortion was shown in figure 8(*a*).

increasing the Hartmann number, the bicritical point moves towards and eventually crosses into the super-rotation regime. We have determined that the bicritical point crosses the $R_i = 0$ line somewhere between $H = 80$ and $H = 84$.

The nonlinear solution branches issued from the bicritical point $(R_i,\ R_o) \approx (-231.5,\ -35\,150)$ at $H = 84$ have been computed in the same way they were for the strictly hydrodynamic case studied above. The critical wavenumbers of the magnetised D17 mode at this point are $(m,\ k) = (1,\ 0.616)$, while those for the super-AMRI modes are $(m,\ k) = (1,\ 1.984)$, which entails flow structures of similar sizes. The bifurcation diagram of figure 7(*b*) has been obtained by varying R_i at constant R_o. To the right (left) of the linear critical point, the base flow is unstable to the D17 (super-AMRI) mode. The imposed azimuthal magnetic field does not break any of the inherent symmetries of the hydrodynamic Taylor–Couette system so that, as in the hydrodynamic case discussed above, there still arise two spirals (along with their mirror images), two ribbons and two mixed modes (and mirror images). See table 1 for an account of all modes. Both nonlinear spiral branches (black curves: solid for $\mathrm{SPI}_{\mathrm{D17}}$, dashed for $\mathrm{SPI}_{\mathrm{MRI}}$) bifurcate subcritically, in the sense that they exist when the corresponding linear mode is stable. However, this is only true while their amplitude remains small, and the branch associated with the D17 mode turns back in a saddle-node bifurcation towards lower $|R_i|$. The $\mathrm{RIB}_{\mathrm{D17}}$ (solid blue) and $\mathrm{RIB}_{\mathrm{MRI}}$ (dashed blue) solution branches both exist to the right of the critical point (blue curves in figure 7*b*).

We note in passing that the super-AMRI-type ribbon solutions found by Rüdiger *et al.* (2016) were shown to be stable by direct numerical simulation. The mixed-mode solution branches (red curves) come in two types, namely MIX_+ and MIX_-, depending on whether the interacting modes have the same or opposite pitch, respectively. Unlike all other solution branches issued from the bicritical point, these extend to large $|R_i|$, and may thus govern the dynamics within the region of the super-rotation regime closest to solid-body rotation.

As is clear from figure 7(*b*), the nonlinear solution branches associated with the super-AMRI instability have the unforeseen property that the torque is reduced with respect to the laminar base value. The dependence of torque on Reynolds number associated with the two mixed modes follows very similar trends. The torque initially grows away from the bifurcation point as the branches dive deep into the super-rotation regime, but the trend is soon reversed and the torque eventually drops below laminar values.

The reason for torque reduction can be understood from the energy balance, since torque corresponds to one of the energy input mechanisms. The perturbation energy budget can be found by integrating $\widetilde{\boldsymbol{v}} \cdot (2.7a) + H^2 \widetilde{\boldsymbol{b}} \cdot (2.7b)$. For travelling-wave-type solutions, perturbation energy must be time-independent and thus the balance

$$\left\langle r \left(\frac{v_b}{r} \right)' \widetilde{u}\widetilde{v} \right\rangle - H^2 \langle r^{-1} (r B_b)' (\widetilde{a}\widetilde{v} - \widetilde{u}\widetilde{b}) \rangle = \langle \widetilde{\boldsymbol{v}} \cdot \nabla^2 \widetilde{\boldsymbol{v}} \rangle + H^2 \langle \widetilde{\boldsymbol{b}} \cdot \nabla^2 \widetilde{\boldsymbol{b}} \rangle \tag{4.2}$$

should be satisfied. Here the angle brackets denote integration over the annular-parallelogram domain. The first terms on the right- and left-hand sides are related to the torque, since integration of $v_b \boldsymbol{e}_\theta \cdot (2.7a)$ yields

$$- \left\langle r \left(\frac{v_b}{r} \right)' \widetilde{u}\widetilde{v} \right\rangle = \langle v_b \boldsymbol{e}_\theta \cdot \nabla^2 \widetilde{\boldsymbol{v}} \rangle \tag{4.3}$$

and integration by parts of the first term on the right-hand side results in

$$\langle \boldsymbol{v} \cdot \nabla^2 \boldsymbol{v} \rangle = (r_o^{-1} R_o - r_i^{-1} R_i) T - \langle |\nabla \boldsymbol{v}|^2 \rangle. \tag{4.4}$$

The energy balance equation (4.2) then becomes

$$- H^2 \langle \widetilde{\boldsymbol{b}} \cdot \nabla^2 \widetilde{\boldsymbol{b}} \rangle - H^2 \langle r^{-1} (r B_b)' (\widetilde{a}\widetilde{v} - \widetilde{u}\widetilde{b}) \rangle = (r_o^{-1} R_o - r_i^{-1} R_i) T - \langle |\nabla \boldsymbol{v}|^2 \rangle. \tag{4.5}$$

Showing that torque cannot decrease below the laminar value for purely hydrodynamic Taylor–Couette flow is a straightforward exercise, because the terms on the left-hand side are identically zero. The calculus of variations can then be used to prove that the minimum value of the functional $\boldsymbol{F}(\boldsymbol{v}) = \langle |\nabla \boldsymbol{v}|^2 \rangle$ under the divergence-free constraint for $\boldsymbol{v}$ is realised by the solution to the Stokes equation (see e.g. Doering & Gibbon 1995), namely the laminar Couette solution. Imposing $\langle |\nabla \boldsymbol{v}|^2 \rangle \geqslant \langle |\nabla \boldsymbol{v}_b|^2 \rangle = (r_o^{-1} R_o - r_i^{-1} R_i) T_b$ on (4.4) demands that $\tau \geqslant 1$ for the purely hydrodynamic case.

Moreover, the balance equation further leads to the conclusion that torque reduction cannot occur at all if the base magnetic field is current-free, as this entails that the second term on the left-hand side of (4.5) is absent. The proof is again straightforward, as integration by parts shows that $-H^2 \langle \widetilde{\boldsymbol{b}} \cdot \nabla^2 \widetilde{\boldsymbol{b}} \rangle$ is positive definite. The resulting inequality,

$$\begin{aligned} (r_o^{-1} R_o - r_i^{-1} R_i) T \;&\geqslant\; (r_o^{-1} R_o - r_i^{-1} R_i) T + H^2 \langle \widetilde{\boldsymbol{b}} \cdot \nabla^2 \widetilde{\boldsymbol{b}} \rangle = \langle |\nabla \boldsymbol{v}|^2 \rangle \\ &\geqslant\; (r_o^{-1} R_o - r_i^{-1} R_i) T_b, \end{aligned} \tag{4.6}$$

yields again $\tau \geqslant 1$. This outlines the necessity of a base current field if torque reduction is to be observed.

As seen in figure 7(*b*), the torque reduction is stronger for the MIX_+ mode, reflecting the fact that the perturbation is slightly larger for that mode. This is evidenced by figure 8(*b*), where the azimuthal mean flow distortion across the gap is

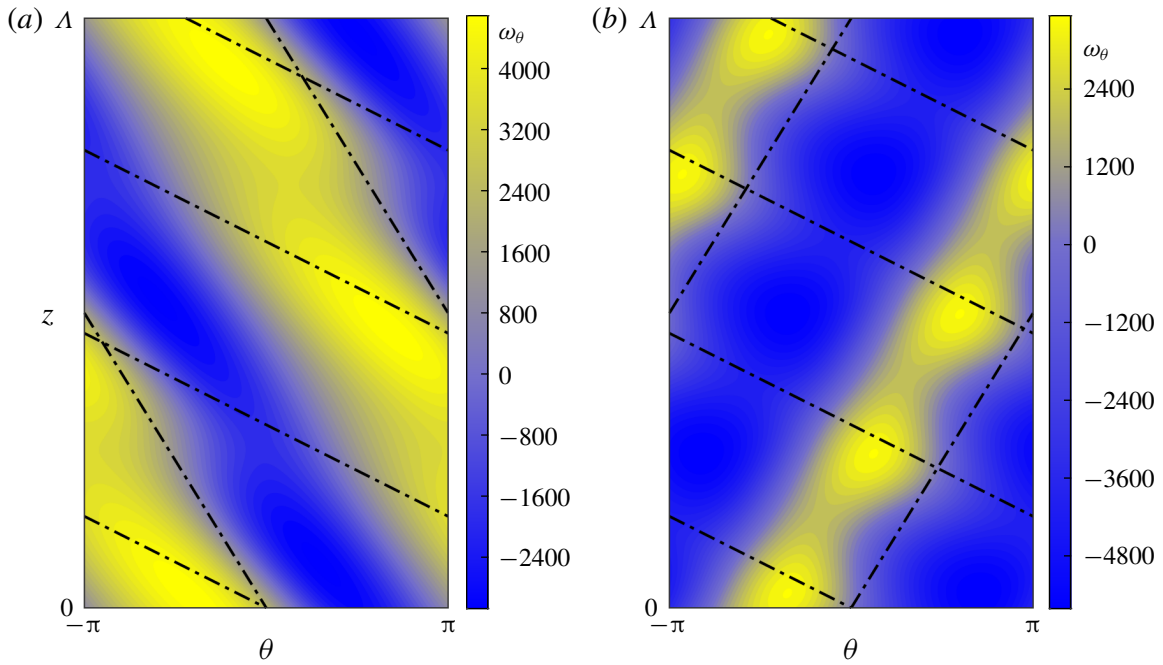

FIGURE 10. Visualisation of the total azimuthal vorticity ($\omega_\theta = \partial_z u - \partial_r w$) at $r = r_i + 0.05$ for the magnetised mixed-mode solutions at $R_i = -280$ in figure 7(*b*). Here $\Lambda = 2\pi/0.616 \approx 10.2$: (*a*) MIX$_-$ and (*b*) MIX$_+$. The corresponding mean flow distortion was shown in figure 8(*b*).

plotted at $R_i = -280$. The oscillatory modulation of the flow near the inner cylinder is responsible for the torque reduction and is driven by the vortex structure near the inner cylinder, as shown in the θ–z sections of figure 10. Here again we choose $r = r_i + 0.05$, very close to the inner cylinder, as the reference radius. As expected, the perturbation of the MIX$_+$ mode has larger amplitude than that for the MIX$_-$ mode. The flow patterns are similar to those of the wavy spiral computed by Altmeyer & Hoffmann (2010) and Deguchi & Altmeyer (2013), because the critical wavenumbers of the interacting modes are of comparable size.

5. Conclusions

We have investigated nonlinear mode competition in MHD Taylor–Couette flow subject to predominantly azimuthal magnetic fields. For this purpose, a Newton solver devised by Deguchi & Altmeyer (2013) for the Navier–Stokes equations in annular-parallelogram domains has been extended for its application to the inductionless limit of the MHD equations.

For the anticyclonic regime (see figure 1), a suitably adjusted weak axial magnetic field in addition to the azimuthal field stimulates linear instability modes with $m = -1,\ 0,\ 1$, as anticipated by Hollerbach *et al.* (2010). Consistent with their results, we find particularly rich nonlinear dynamics for $\delta \simeq 0.04$. In § 3, we identified that there is a triple critical point involving all three modes for $\delta \approx 0.0413$. We have tracked the three nonlinear mixed-mode solution branches that bifurcate simultaneously at the triple critical point using the purposely devised Newton solver and arclength continuation. Some of the mixed-mode solutions possess a larger angular momentum transport (they require application of higher driving torque to keep the cylinders rotating) than the single-mode solutions they result from. This increased transport of angular momentum makes these mixed-mode solutions an interesting target for future study, as they might be relevant in astrophysical flows involving

accretion disks. In particular, a better understanding of what their role might be in the nonlinear dynamics of such flows will require direct numerical simulations and experiments such as those by PROMISE (Rüdiger *et al.* 2006; Stefani *et al.* 2006, 2007).

In § 4, we have studied mode competition involving the D17 mode. In the purely hydrodynamic case, there is a point where both the classical spiral mode and the D17 mode become neutral simultaneously. This bicritical point lies within the counter-rotation regime (see figure 1). The corresponding mixed-mode solutions consist of an interesting stripe pattern where the small-scale classical spirals are modulated by the larger-scale structure of the D17 mode. All purely hydrodynamic results presented here are in excellent agreement with analogous computations done with an independently developed Petrov–Galerkin code devised by Meseguer *et al.* (2007) and presently extended to allow computation of mixed-mode travelling–rotating wave solutions in annular-parallelogram domains. This code is better suited for the study of large-scale pattern formation in Taylor–Couette flow and includes not only a travelling–rotating wave Newton–Krylov matrix-free solver (thus being capable of handling a much larger number of degrees of freedom), but also stability analysis, a solver for modulated travelling–rotating waves and pseudo-arclength continuation of solution branches adapted from Mellibovsky & Meseguer (2015), and also direct numerical simulation. Details of this second code and its adaptation to annular-parallelogram domains will be presented in our future work on the study of large-scale pattern formation in Taylor–Couette flow. The intricacies of the method reach beyond the scope of the present study.

The application of an external azimuthal magnetic field alters the picture obtained in the purely hydrodynamic case completely. The non-axisymmetric super-AMRI mode found by Rüdiger *et al.* (2016, 2018*a*,*b*) appears at moderate Hartmann numbers and eventually outweighs the classical mode for sufficiently strong magnetic fields. We clearly show that the mechanisms behind the magnetised D17 mode and the super-AMRI mode are distinct. Destabilisation of the D17 mode occurs for a given external magnetic field profile (4.1). As a result, an increase of the Hartmann number gradually shifts the bicritical point at which both modes are simultaneously destabilised towards the super-rotation regime. This fact renders this mode interaction interesting from an astrophysical point of view. Several nonlinear solution branches are issued from the bicritical point in both R_i directions at fixed R_o. While spirals and ribbons return towards the counter-rotation regime, the mixed-mode solution branches plunge deep into the super-rotation regime.

The solutions computed in § 4 show how the complex interplay between the nonlinear shear–Coriolis and the magneto-rotational instabilities can sometimes lead to torques lower than that of the base flow. This surprising result is in sharp contrast with what is typically assumed in purely hydrodynamic shear-flow studies, where nonlinearity is known to invariably enhance angular momentum transport. This torque reduction occurs even for finite P_m and sub-rotation of the cylinders; see appendix B. In view of this result, torque reduction might be a generic property of MHD flows in the presence of shear and Coriolis forces. A particularly interesting potential application of this phenomenon would be to design control strategies to reduce drag on the curved boundary layers by imposing suitable magnetic fields.

We have analysed the D17/super-AMRI mode interaction for a large gap $\eta = 0.1$. Interesting as it would be, we have not attempted here to track these modes to smaller annulus gaps in the order $\eta \sim 0.8$ and test the robustness of the coalescence point of both instabilities. The extremely large Reynolds numbers at which the D17

mode bifurcates in the narrow annulus case renders the task overly demanding from a computational point of view, if not altogether unaffordable.

Imposing more intense helical magnetic fields might also be an appealing topic for future research. The two axisymmetric super-HMRI modes found recently by Mamatsashvili *et al.* (2019), in combination with some of the modes studied here, may also yield rich interaction patterns worth exploring. While their type 2 super-HMRI mode belongs to the class of MRI requiring induction together with SMRI, the type 1 super-HMRI mode is inductionless and might therefore coexist with the super-AMRI mode and interact nonlinearly. Both types of super-HMRI modes might of course interact with the D17 mode. For HMRI, the further consideration of current in the fluid brings about even richer instability phenomena as anticipated by a locally periodic approach (Liu *et al.* 2006; Kirillov & Stefani 2013; Kirillov *et al.* 2014). The interaction of short-wavelength modes found using the locally periodic approach with longer-wavelength modes such as D17 or super-AMRI modes would generate band-like patterns much as those in figure 9.

Acknowledgements

K.D.'s research was supported by Australian Research Council Discovery Early Career Researcher Award DE170100171. The research of R.A., F.M. and A.M. was supported by the Spanish MINECO grants FIS2016-77849-R and FIS2017-85794-P and the Generalitat de Catalunya grant 2017-SGR-785. We gratefully acknowledge insightful comments and suggestions made by Professor R. Hollerbach during the review process.

Declaration of interests

The authors report no conflict of interest.

Appendix A. Basis function for the magnetic potentials

Following Roberts (1964), we first determine the magnetic field for the outer zones $r < r_i$ and $r > r_o$. Within the perfectly insulating walls, the magnetic field must have a potential φ because there is no current:

$$\widetilde{a} = \varphi_r, \quad \widetilde{b} = r^{-1}\varphi_\theta, \quad \widetilde{c} = \varphi_z. \tag{A 1a–c}$$

Since the magnetic field is solenoidal, the outer potential must satisfy Laplace's equation. Using the expansion

$$\varphi = \sum_{n_1,n_2} \widehat{\varphi}_{n_1 n_2}(r) \mathrm{e}^{\mathrm{i}(n_1\xi_1 + n_2\xi_2)}, \tag{A 2}$$

it is easy to find that the solution $\widehat{\varphi}_{n_1 n_2}(r)$ can be written down using the modified Bessel functions of the first and second kinds, $\mathrm{I}_\nu(x)$ and $\mathrm{K}_\nu(x)$, both of which satisfy $x^2 f'' + xf' - (x^2 + \nu^2)f = 0$. The requirement that the potential is analytic at $r = 0$ determines the solution for $r < r_i$ as

$$\widehat{\varphi}_{n_1 n_2} = \begin{cases} \mathrm{I}_{|A_{n_1 n_2}|}(|B_{n_1 n_2}|r) & \text{if } |B_{n_1 n_2}| \neq 0, \\ r^{|A_{n_1 n_2}|} & \text{if } |B_{n_1 n_2}| = 0, \end{cases} \tag{A 3a}$$

whilst if the amplitude of the potential decays for large r, the solution for $r > r_o$ is

$$\widehat{\varphi}_{n_1 n_2} = \begin{cases} \mathrm{K}_{|A_{n_1 n_2}|}(|B_{n_1 n_2}|r) & \text{if } |B_{n_1 n_2}| \neq 0, \\ r^{-|A_{n_1 n_2}|} & \text{if } |B_{n_1 n_2}| = 0. \end{cases} \tag{A 3b}$$

Here we have used the shorthand notation $A_{n_1n_2} = n_1m_1 + n_2m_2$ and $B_{n_1n_2} = n_1k_1 + n_2k_2$. Note that the mean part $\widehat{\varphi}_{00}$ must be zero, from the boundary conditions.

Across the cylinder walls, the magnetic field must be continuous. Thus from (A 1) and the outer potential solutions (A 3), the boundary conditions are found as

$$\widehat{b}_{n_1n_2} = \frac{A_{n_1n_2}}{r_i B_{n_1n_2}}\widehat{c}_{n_1n_2} \quad \text{and} \quad \widehat{a}_{n_1n_2} + \frac{\mathrm{i}Q^-_{n_1n_2}}{B_{n_1n_2}}\widehat{c}_{n_1n_2} = 0 \quad \text{at } r = r_i, \tag{A 4a}$$

$$\widehat{b}_{n_1n_2} = \frac{A_{n_1n_2}}{r_o B_{n_1n_2}}\widehat{c}_{n_1n_2} \quad \text{and} \quad \widehat{a}_{n_1n_2} + \frac{\mathrm{i}Q^+_{n_1n_2}}{B_{n_1n_2}}\widehat{c}_{n_1n_2} = 0 \quad \text{at } r = r_o. \tag{A 4b}$$

Here $Q^{\pm}_{n_1n_2}$ denotes the value of $\partial_r\widehat{\varphi}_{n_1n_2}/\widehat{\varphi}_{n_1n_2}$ on the walls:

$$Q^-_{n_1n_2} = \begin{cases} \dfrac{|A_{n_1n_2}|}{r_i} + \dfrac{|B_{n_1n_2}|\mathrm{I}_{|A_{n_1n_2}|+1}(|B_{n_1n_2}|r_i)}{\mathrm{I}_{|A_{n_1n_2}|}(|B_{n_1n_2}|r_i)} & \text{if } |B_{n_1n_2}| \neq 0, \\ \dfrac{|A_{n_1n_2}|}{r_i} & \text{if } |B_{n_1n_2}| = 0, \end{cases} \tag{A 5a}$$

$$Q^+_{n_1n_2} = \begin{cases} \dfrac{|A_{n_1n_2}|}{r_o} - \dfrac{|B_{n_1n_2}|\mathrm{K}_{|A_{n_1n_2}|+1}(|B_{n_1n_2}|r_o)}{\mathrm{K}_{|A_{n_1n_2}|}(|B_{n_1n_2}|r_o)} & \text{if } |B_{n_1n_2}| \neq 0, \\ -\dfrac{|A_{n_1n_2}|}{r_o} & \text{if } |B_{n_1n_2}| = 0. \end{cases} \tag{A 5b}$$

After some algebra, we can find the boundary conditions for the poloidal and toroidal potentials as

$$\widehat{f}'_{n_1n_2} + M^-_{n_1n_2}\widehat{f}_{n_1n_2} = 0 \quad \text{and} \quad \widehat{g}_{n_1n_2} - \gamma_{n_1n_2}(r_i)\widehat{f}_{n_1n_2} = 0 \quad \text{at } r = r_i, \tag{A 6a}$$

$$\widehat{f}'_{n_1n_2} + M^+_{n_1n_2}\widehat{f}_{n_1n_2} = 0, \quad \text{and} \quad \widehat{g}_{n_1n_2} - \gamma_{n_1n_2}(r_o)\widehat{f}_{n_1n_2} = 0 \quad \text{at } r = r_o, \tag{A 6b}$$

where

$$\gamma_{n_1n_2}(r) = \frac{2A_{n_1n_2}B_{n_1n_2}}{B^2_{n_1n_2}r^2 + A^2_{n_1n_2}}, \tag{A 7a}$$

$$M^-_{n_1n_2} = \frac{r_i^2B^2_{n_1n_2} - A^2_{n_1n_2}}{r_i^2B^2_{n_1n_2} + A^2_{n_1n_2}} - \frac{r_i^2B^2_{n_1n_2} + A^2_{n_1n_2}}{r_i^2Q^-_{n_1n_2}}, \tag{A 7b}$$

$$M^+_{n_1n_2} = \frac{r_o^2B^2_{n_1n_2} - A^2_{n_1n_2}}{r_o^2B^2_{n_1n_2} + A^2_{n_1n_2}} - \frac{r_o^2B^2_{n_1n_2} + A^2_{n_1n_2}}{r_o^2Q^+_{n_1n_2}}. \tag{A 7c}$$

The second boundary conditions in (A 6) suggest that the functions $\widehat{g}_{n_1n_2} - \gamma_{n_1n_2}\widehat{f}_{n_1n_2}$ must vanish on the walls, and thus we can use $(1 - y^2)T_l(y)$ to expand them. The function $\widehat{f}_{n_1n_2}$ satisfies Robin's conditions on the walls as seen in the first boundary conditions in (A 6). As shown in Deguchi (2019*b*), we can use the following modified basis functions

$$(1 - y^2)T_l(y) + \alpha_{ln_1n_2} + \beta_{ln_1n_2}y, \tag{A 8}$$

where

$$\alpha_{ln_1n_2} = 2\frac{(-1)^l(1 + M^+_{n_1n_2}) + (1 - M^-_{n_1n_2})}{(1 - M^-_{n_1n_2})M^+_{n_1n_2} - (1 + M^+_{n_1n_2})M^-_{n_1n_2}}, \tag{A 9a}$$

$$\beta_{ln_1n_2} = -2\frac{(-1)^lM^+_{n_1n_2} + M^-_{n_1n_2}}{(1 - M^-_{n_1n_2})M^+_{n_1n_2} - (1 + M^+_{n_1n_2})M^-_{n_1n_2}}. \tag{A 9b}$$

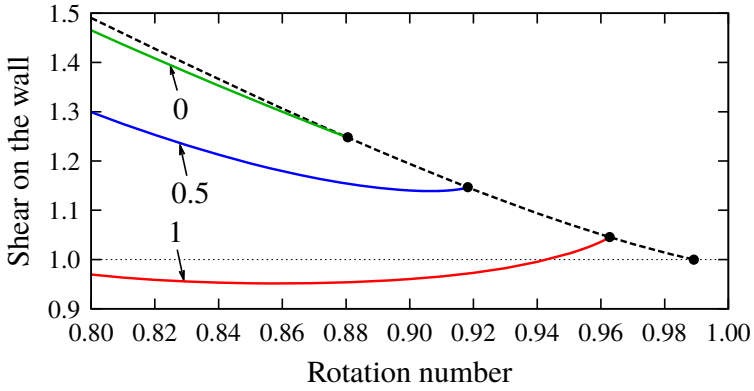

FIGURE 11. The narrow-gap computation for $P_m = 1$, $R = 400$, and the axial wavenumber $k = 3.117$. Dashed curve: Taylor-vortex flow. Solid curves: the wavy-vortex flow branches. The streamwise wavenumber (i.e. m/r_m at the narrow-gap limit) is 2.2. The values of B_0 are indicated by the arrows. The horizontal axis is the rotation number ω. In the vertical coordinate, the shear on the wall is normalised by its laminar value (i.e. τ at the narrow-gap limit).

Appendix B. Drag reduction of the wavy vortex flow

Here we show that the significant drag reduction observed in § 4 occurs even for the Rayleigh-unstable sub-rotation regime (see figure 1). Moreover, the Prandtl number is not necessarily small to observe this phenomenon; here we choose $P_m = 1$. The base magnetic field (4.1) is used.

We employ the narrow-gap limit $\eta \to 1$ in order to use the full MHD Cartesian code developed in Deguchi (2019*a*). Now we write $x = r_m\theta$ and $y = (r - r_m)$ using the mid-gap r_m. When η is close to unity, noting that $y/r_m \ll 1$, we have approximations

$$v_b(r) - \Omega r = -Ry + \cdots, \quad HB_b(r) = -B_0 Ry + \cdots, \tag{B 1a,b}$$

while keeping $\Omega = r_m^{-1} v_b(r_m)$, $R = 2r_m^{-2} R_p$ and $B_0 = H/R_p$ as $O((1-\eta)^0)$ constants. (Note that the definition of R differs by factor of 4 from that used in Deguchi (2019*a*), because in this paper the gap is 2.) The limiting system is the rotating plane Couette flow in Cartesian coordinates (x, y, z) with the rotation rate $\omega = 2\Omega/R$. The Rayleigh-unstable region is $\omega \in [0, 1]$. For $B_0 \neq 0$, the flow is subjected to a linear magnetic field pointing in the streamwise direction.

The first few bifurcation sequence of hydrodynamic rotating plane Couette flow is widely acknowledged (see e.g. Nagata 1986, Daly *et al.* 2014). Near the Rayleigh line $\omega = 1$, the Taylor-vortex flow bifurcates with the well-known axial critical wavenumber $k = 3.117$ as depicted by the dashed curve in figure 11. Further bifurcation of the green solid curve is due to the three-dimensional secondary instability of the Taylor vortex and called the wavy-vortex flow.

The other solid curves in figure 11 (blue for $B_0 = 0.5$, red for $B_0 = 1$) show that with increasing B_0 the shear associated with the wavy-vortex flow is eventually reduced even below the laminar value. Here note that this reduction only occurs when the flow is dependent on x (i.e. azimuthal direction). For example, Taylor-vortex flow is x-independent, and thus the shear is unchanged whatever the value of B_0 is. This is because the cross-streamwise components of the magnetic field needed to modify the mean flow remains zero under the influence of the streamwise magnetic field.

REFERENCES

ALTMEYER, S. & HOFFMANN, C. 2010 Secondary bifurcation of mixed-cross-spirals connecting travelling wave solutions. *New J. Phys.* **12**, 113035.

ANDERECK, C. D., LIU, S. S. & SWINNEY, H. L. 1986 Flow regimes in a circular Couette system with independently rotating cylinders. *J. Fluid Mech.* **164**, 155–183.

AVILA, M., MESEGUER, A. & MARQUES, F. 2006 Double Hopf bifurcation in corotating spiral Poiseuille flow. *Phys. Fluids* **18**, 064101.

BALBUS, S. A. 2017 When is high Reynolds number shear flow not turbulent? *J. Fluid Mech.* **824**, 1–4.

BALBUS, S. & HAWLEY, J. F. 1991 A powerful local shear instability in weakly magnetised disks. I. Linear analysis. *Astrophys. J.* **376**, 214–222.

BURIN, M. J. & CZARNOCKI, C. J. 2012 Subcritical transition and spiral turbulence in circular Couette flow. *J. Fluid Mech.* **709**, 106–122.

CHANDRASEKHAR, S. 1960 The stability of non-dissipative Couette flow in hydromagnetics. *Proc. Natl Acad. Sci. USA* **46**, 253–257.

CHILD, A., KERSALÉ, E. & HOLLERBACH, R. 2015 Nonaxisymmetric linear instability of cylindrical magnetohydrodynamic Taylor–Couette flow. *Phys. Rev.* E **92**, 033011.

CHOSSAT, P. & IOOSS, G. 1994 *The Couette-Taylor Problem*. Springer.

COLES, D. 1965 Transition in circular Couette flow. *J. Fluid Mech.* **21**, 385–425.

DALY, C. A., SCHNEIDER, T. M., SCHLATTER, P. & PEAKE, N. 2014 Secondary instability and tertiary states in rotating plane Couette flow. *J. Fluid Mech.* **761**, 27–61.

DAVEY, A., DIPRIMA, R. C. & STUART, J. T. 1968 On the instability of Taylor vortices. *J. Fluid Mech.* **31**, 17–52.

DAVIDSON, P. A. *Introduction to Magnetohydrodynamics*, 2nd edn. Cambridge University Press.

DEGUCHI, K. 2016 The rapid-rotation limit of the neutral curve for Taylor–Couette flow. *J. Fluid Mech.* **808**, R2.

DEGUCHI, K. 2017 Linear instability in Rayleigh-stable Taylor–Couette flow. *Phys. Rev.* E **95**, 021102.

DEGUCHI, K. 2019*a* High-speed shear-driven dynamos. Part 2. Numerical analysis. *J. Fluid Mech.* **876**, 830–858.

DEGUCHI, K. 2019*b* High-speed standard magneto-rotational instability. *J. Fluid Mech.* **865**, 492–522.

DEGUCHI, K. & ALTMEYER, S. 2013 Fully nonlinear mode competitions of nearly bicritical spiral or Taylor vortices in Taylor–Couette flow. *Phys. Rev.* E **87**, 043017.

DEGUCHI, K., MESEGUER, A. & MELLIBOVSKY, F. 2014 Subcritical equilibria in Taylor–Couette flow. *Phys. Rev. Lett.* **112**, 184502.

DEGUCHI, K. & NAGATA, M. 2011 Bifurcations and instabilities in sliding Couette flow. *J. Fluid Mech.* **678**, 156–178.

DOERING, C. R. & GIBBON, J. D. 1995 *Applied Analysis of the Navier–Stokes Equations*. Cambridge University Press.

DONG, S. 2009 Evidence for internal structures of spiral turbulence. *Phys. Rev.* E **80**, 067301.

EDLUND, E. M. & JI, H. 2014 Nonlinear stability of laboratory quasi-Keplerian flows. *Phys. Rev.* E **89**, 021004.

ESSER, A. & GROSSMANN, S. 1996 Analytic expression for Taylor–Couette stability boundary. *Phys. Fluids* **8**, 1814–1819.

GOLUBITSKY, M., STEWART, I. & SCHAEFFER, D. G. 1988 *Singularities and Groups in Bifurcation Theory*, App. Math. Sci., vol. 2. Springer.

GOODMAN, J. & JI, H. 2002 Magnetorotational instability of dissipative Couette flow. *J. Fluid Mech.* **462**, 365–382.

GROSSMANN, S., LOHSE, D. & SUN, C. 2016 High–Reynolds number Taylor–Couette turbulence. *Annu. Rev. Fluid Mech.* **48**, 53–80.

GUSEVA, A., WILLIS, A. P., HOLLERBACH, R. & AVILA, M. 2015 Transition to magnetorotational turbulence in Taylor–Couette flow with imposed azimuthal magnetic field. *New J. Phys.* **17**, 093018.

GUSEVA, A., WILLIS, A. P., HOLLERBACH, R. & AVILA, M. 2017 Transport properties of the azimuthal magnetorotational instability. *Astrophys. J.* **849** (2), 92.

HEGSETH, J. J., ANDERECK, C. D., HAYOT, F. & POMEAU, Y. 1989 Spiral turbulence and phase dynamics. *Phys. Rev. Lett.* **62** (3), 257–260.

HERRON, I. & SOLIMAN, F. 2006 The stability of Couette flow in a toroidal magnetic field. *Appl. Maths Lett.* **19**, 1113–1117.

HOLLERBACH, R. & RÜDIGER, G. 2005 New type of magnetorotational instability in cylindrical Taylor–Couette flow. *Phys. Rev. Lett.* **95**, 124501.

HOLLERBACH, R., TEELUCK, V. & RÜDIGER, G. 2010 Nonaxisymmetric magnetorotational instabilities in cylindrical Taylor–Couette flow. *Phys. Rev. Lett.* **104**, 044502.

IOOSS, G. 1986 Secondary bifurcations of Taylor vortices into wavy inflow or outflow boundaries. *J. Fluid Mech.* **173**, 273–288.

JI, H., BURIN, M., SCHARTMAN, E. & GOODMAN, J. 2006 Hydrodynamic turbulence cannot transport angular momentum effectively in astrophysical disks. *Nature* **444**, 343–346.

KELLEY, C. T. 2003 *Solving Nonlinear Equations with Newton's Method*. SIAM.

KIRILLOV, O. N. & STEFANI, F. 2013 Extending the range of the inductionless magnetorotational instability. *Phys. Rev. Lett.* **111**, 061103.

KIRILLOV, O. N., STEFANI, F. & FUKUMOTO, Y. 2012 A unifying picture of helical and azimuthal magnetorotational instability, and the universal significance of the Liu limit. *Astrophys. J.* **756** (1), 83.

KIRILLOV, O. N., STEFANI, F. & FUKUMOTO, Y. 2014 Local instabilities in magnetized rotational flows: a short-wavelength approach. *J. Fluid Mech.* **760**, 591–633.

KUZNETSOV, Y. A. 2004 *Elements of Applied Bifurcation Theory*, 3rd edn. Springer.

LIU, W., GOODMAN, J., HERRON, I. & JI, H. 2006 Helical magnetorotational instability in magnetized Taylor–Couette flow. *Phys. Rev.* E **74**, 056302.

LOPEZ, J. M. & AVILA, M. 2017 Boundary-layer turbulence in experiments on quasi-Keplerian flows. *J. Fluid Mech.* **817**, 21–34.

MAMATSASHVILI, G., STEFANI, F., HOLLERBACH, R. & RÜDIGER, G. 2019 Two types of axisymmetric helical magnetorotational instability in rotating flows with positive shear. *Phys. Rev. Fluids* **4**, 103905.

MELLIBOVSKY, F. & MESEGUER, A. 2006 The role of streamwise perturbations in pipe flow transition. *Phys. Fluids* **18**, 074104.

MELLIBOVSKY, F. & MESEGUER, A. 2015 A mechanism for streamwise localisation of nonlinear waves in shear flows. *J. Fluid Mech.* **779**, R1.

MESEGUER, A., AVILA, M., MELLIBOVSKY, F. & MARQUES, F. 2007 Solenoidal spectral formulations for the computation of secondary flows in cylindrical and annular geometries. *Eur. Phys. J. Spec. Top.* **146**, 249–259.

MESEGUER, A., MELLIBOVSKY, F., AVILA, M. & MARQUES, F. 2009 Instability mechanisms and transition scenarios of spiral turbulence in Taylor–Couette flow. *Phys. Rev.* E **80**, 046315.

MICHAEL, D. 1954 The stability of an incompressible electrically conducting fluid rotating about an axis when current flows parallel to the axis. *Mathematika* **1**, 45–50.

NAGATA, M. 1986 Bifurcations in Couette flow between almost corotating cylinders. *J. Fluid Mech.* **169**, 229–250.

OSTILLA-MONICO, R., VERZICCO, R. & LOHSE, D. 2016 Turbulent Taylor–Couette flow with stationary inner cylinder. *J. Fluid Mech.* **799**, R1.

PINTER, A., LÜCKE, M. & HOFFMANN, C. 2006 Competition between traveling fluid waves of left and right spiral vortices and their different amplitude combinations. *Phys. Rev. Lett.* **96**, 044506.

PRIGENT, A., GREGOIRE, G., CHATE, H., DAUCHOT, O. & VAN SAARLOOS, W. 2002 Finite-wavelength modulation within turbulent shear flows. *Phys. Rev. Lett.* **89**, 014501.

ROBERTS, P. H. 1964 The stability of hydromagnetic Couette flow. *Proc. Camb. Phil. Soc.* **60**, 635–651.

RÜDIGER, G., GELLERT, M., HOLLERBACH, R., SCHULTZ, M. & STEFANI, F. 2018*a* Stability and instability of hydromagnetic Taylor–Couette flows. *Phys. Rep.* **741**, 1–89.

RÜDIGER, G. & HOLLERBACH, R. 2007 Comment on 'helical magnetorotational instability in magnetized Taylor–Couette flow'. *Phys. Rev.* E **76**, 068301.

RÜDIGER, G., HOLLERBACH, R., STEFANI, F., GUNDRUM, T., GERBETH, G. & ROSNER, R. 2006 The traveling-wave MRI in cylindrical Taylor–Couette flow: comparing wavelengths and speeds in theory and experiment. *Astrophys. J.* **649**, L145–L147.

RÜDIGER, G., SCHULTZ, M., GELLERT, M. & STEFANI, F. 2016 Subcritical excitation of the current-driven Tayler instability by super-rotation. *Phys. Fluids* **28**, 014105.

RÜDIGER, G., SCHULTZ, M., GELLERT, M. & STEFANI, F. 2018*b* Azimuthal magnetorotational instability with super-rotation. *J. Plasma Phys.* **84**, 735840101.

SEILMAYER, M., GALINDO, V., GERBETH, G., GUNDRUM, T., STEFANI, F., GELLERT, M., RÜDIGER, G., SCHULTZ, M. & HOLLERBACH, R. 2014 Experimental evidence for nonaxisymmetric magnetorotational instability in a rotating liquid metal exposed to an azimuthal magnetic field. *Phys. Rev. Lett.* **113**, 024505.

STEFANI, F., GERBETH, G., GUNDRUM, T., HOLLERBACH, R., PRIEDE, J., RÜDIGER, G. & SZKLARSKI, J. 2009 Helical magnetorotational instability in a Taylor–Couette flow with strongly reduced Ekman pumping. *Phys. Rev.* E **80**, 066303.

STEFANI, F., GUNDRUM, T., GERBETH, G., RÜDIGER, G., SCHULTZ, J., SZKLARSKI, J. & HOLLERBACH, R. 2006 Experimental evidence for magnetorotational instability in a Taylor–Couette flow under the influence of a helical magnetic field. *Phys. Rev. Lett.* **97**, 184502.

STEFANI, F., GUNDRUM, T., GERBETH, G., RÜDIGER, G., SZKLARSKI, J. & HOLLERBACH, R. 2007 Experiments on the magnetorotational instability in helical magnetic fields. *New J. Phys.* **9**, 295.

STEFANI, F. & KIRILLOV, O. N. 2015 Destabilization of rotating flows with positive shear by azimuthal magnetic fields. *Phys. Rev.* E **92**, 051001.

TAGG, R., EDWARDS, W. S., SWINNEY, H. L. & MARCUS, P. S. 1989 Nonlinear standing waves in Couette–Taylor flow. *Phys. Rev.* A **39**, 3734–3737.

TAYLER, R. J. 1957 Hydromagnetic instabilities of an ideally conducting fluid. *Proc. R. Phys. Soc.* **70**, 31–48.

TAYLOR, G. I. 1923 Stability of a viscous fluid contained between two rotating cylinders. *Phil. Trans. R. Soc. Lond.* A **223**, 289–343.

VAN ATTA, C. 1966 Exploratory measurements in spiral turbulence. *J. Fluid Mech.* **25**, 495–512.

VELIKHOV, E. P. 1959 Stability of an ideally conducting liquid flowing between cylinders rotating in a magnetic field. *Sov. Phys. JETP* **36**, 1389–1404.

WENDT, F. 1933 Turbulente strömungen zwischen zwei rotierenden koaxialen zylindern. *Ing.-Arch.* **4**, 577–595.

3.4 Concluding remarks

This work explores in detail the mode competition between different spirals arising from magnetic and hydrodynamic instabilities. Our participation in this collaboration has been focused on analysing the purely hydrodynamical structures, specially exploring the bicritical point where the classical and the new CCF instabilities become simultaneously neutral. All computations have been performed by using skewed domains suitably adapted to align with the underlying spiral solutions.

The emerging nonlinear structures captured in the vicinity of the bicritical point, namely spirals, ribbons and mixed modes, show a characteristic shift towards the inner cylinder, being specially stronger in the centrifugally unstable region of the gap. In particular, the hydrodynamic mixed modes exhibit small-large scale interactions, surprisingly resembling the characteristic SPT helical structure. We have performed extensive explorations analysing the possible subcriticality of these modes, trying to extend them down to moderate R_o where they could coexist with stable CCF and might act as SPT precursors. Unfortunately, none of these explorations reported any subcritical behaviour for either the mixed modes or the spirals, so that their possible relation with SPT remains unclear.

Chapter 4

Flows between orthogonally stretching parallel plates

Flows driven by stretching or shrinking membranes are of special interest for many industrial applications such as cooling and extrusion processes, paper production, polymer processing and metallurgy (Aziz & Mahomed, 2016), or in modelling physiological blood flows (Waters, 2001, 2004). In spite of this, extensional flows have attracted minor attention from the scientific community compared to classical open flows such as pipes or channels. For this reason, in this chapter we address the generalisation of flows between biorthogonally stretching parallel plates.

4.1 Introduction

The first self-similar solution for stretching-shrinking flows was computed by Crane (1970), who studied the fluid motion induced by a linearly stretching flat plate whose velocity is proportional to the distance from the stagnation point. Afterwards, Wang (1984) explored the three-dimensional generalisation of the Crane's problem, by considering a membrane stretching from the origin towards the boundaries; see Fig. 4.1a. Following these explorations in unbounded stretching flows, recent studies have reported new self-similar solutions for the biorthogonal generalisation (Ariel, 2003; Weidman & Ishak, 2015).

In addition, two-dimensional channel flows between stretching or shrinking parallel plates were initially explored by Brady & Acrivos (1981). Although these flows

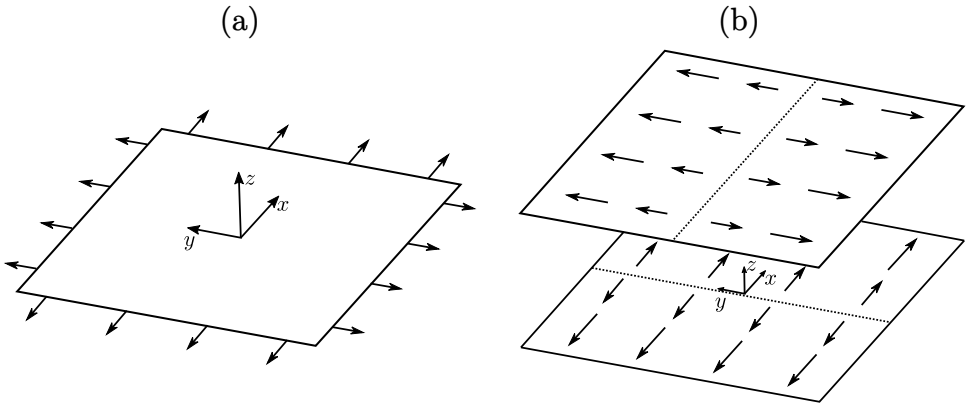

Figure 4.1. (a) Wang (1984) stretching membrane with the corresponding stagnation point located at the origin. (b) Three-dimensional biorthogonally stretching parallel plates configuration considered in Ayats *et al.* (2021).

have been recently further investigated by Marques *et al.* (2017), allowing for arbitrary stretching-shrinking rates, the corresponding three-dimensional generalisation was still missing. For this reason, in Ayats *et al.* (2021) we perform such generalisation and compute the emerging exact solutions of the Navier-Stokes equations under the self-similar ansatz assumption. Fig. 4.1b shows an schematic representation of the three-dimensional domain by depicting the boundary conditions at the confining walls. In our case, arbitrary configurations of the acceleration rates are explored by unfolding the calculated solutions in the corresponding parameter space.

Due to the particularity of the boundary conditions at the confining plates, most of the aforementioned studies exclusively consider self-similar solutions of the Navier-Stokes equations, which significantly simplify the functional dependence of the flow by taking advantage of spatial scale invariance properties. This kind of solutions are widely used not only in mathematical studies (see Drazin & Riley, 2006, for a detailed description) but also in a vast range of multidisciplinary applications such as physiological blood flows and oxygen transport in cardiac systems (Waters, 2001, 2004).

The validity of the aforementioned self-similar solutions has been recently tested by Espin & Papageorgiou (2009) in two-dimensional finite domains, by imposing self-similar boundary conditions exclusively at the sides of the computational domain. This study concludes that both flows are qualitatively equivalent up to moderate Reynolds numbers when plates are symmetrically stretching. However, substantial

differences were reported for the shrinking configurations due to some strong flow instabilities.

4.2 Research objectives

The main objective of this research is to address the missing three-dimensional generalisation of extensional flows in planar channels whose confining parallel walls are independently stretching or shrinking at arbitrary acceleration rates. Unknown three-dimensional exact solutions of the Navier-Stokes equations, under the assumption of the self-similar ansatz, have to be initially identified and subsequently unfolded along the parameter space, to cover all possible configurations of the acceleration rates.

4.3 Indexed publication

This section is a reproduction of Ayats *et al.* (2021), containing a complete exploration of the steady flows found in this particular problem.

Physics of Fluids ARTICLE scitation.org/journal/phf

Flows between orthogonally stretching parallel plates

Cite as: Phys. Fluids 33, 024103 (2021); doi: 10.1063/5.0037097
Submitted: 10 November 2020 • Accepted: 28 December 2020 •
Published Online: 4 February 2021

R. Ayats,[1] F. Marques,[1] A. Meseguer,[1,a)] and P. D. Weidman[2]

AFFILIATIONS

[1] Department of Physics, Universitat Politècnica de Catalunya, Barcelona 08034, Spain
[2] Department of Mechanical Engineering, University of Colorado, Boulder, Colorado 80309-0427, USA

[a)] **Author to whom correspondence should be addressed:** alvaro.meseguer@upc.edu

ABSTRACT

Navier–Stokes equilibrium solutions of a viscous fluid confined between two infinite parallel plates that can independently stretch or shrink in orthogonal directions are studied. It is assumed that the admissible solutions satisfy spatial self-similarity in the stretching or shrinking perpendicular coordinates. The nonlinear steady boundary-value problem is discretized using a spectral Legendre method, and equilibrium solutions are found and tracked in the two-dimensional parameter space by means of pseudo-arclength continuation Newton–Krylov schemes. Different families of solutions have been identified, some of which are two-dimensional and correspond to the classical Wang and Wu self-similar flows arising in a plane channel with one stretching–shrinking wall [Wang, C.-A. and Wu, T.-C., "Similarity solutions of steady flows in a channel with accelerating walls," Comput. Math. Appl. **30**, 1–16 (1995)]. However, a large variety of three-dimensional solutions have also been found, even for low stretching or shrinking rates. When slightly increasing those rates, some of these solutions disappear at saddle-node bifurcations. By contrast, when both plates are simultaneously stretching or shrinking at higher rates, a wide variety of new families of equilibria are created and annihilated in the neighborhood of cuspidal codimension-2 bifurcation points. This behavior has similarities with the one observed in other planar and cylindrical self-similar flows.

I. INTRODUCTION

The study of viscous fluid motions bounded by stretching or shrinking surfaces is of fundamental importance in the mathematical modeling of physiological fluid flows (Waters, 2001; 2004). In these types of flows, self-similarity of the Navier–Stokes solution is usually assumed, where the velocity field incorporates the spatial dependence of the non-uniform boundary conditions at the stretching or shrinking walls. Fluid motion induced by a single stretching flat plate was first studied by Crane (1970). The generalized problem, consisting of a biorthogonally stretching membrane, was later addressed in the study of Wang (1984) and more recently in the study of Weidman and Ishak (2015). For a comprehensive review of exact Navier–Stokes solutions, including self-similar flow profiles, see the monograph by Drazin and Riley (2006). For a recent update on these types of unbounded flows induced by extended stretching boundaries, see the more recent review by Wang (2011). In Crane's original formulation, as well as in its biorthogonal generalization, it is assumed that the wall-normal coordinate is unbounded. By contrast, other studies have explored flows arising in two-dimensional channels with confining parallel walls stretching and shrinking in the streamwise direction (Brady and Acrivos, 1981 and Marques *et al.*, 2017). In these planar geometries, alternative finite difference discretizations providing more realistic boundary conditions have been recently proposed (Espín and Papageorgiou, 2009). Although these formulations do not impose the self-similarity ansatz in the interior of the computational domain, the observed dynamics are consistent with the extensional computations, at least for moderate Reynolds numbers.

In this work, we address the generalization of extensional flows in planar channels whose confining parallel walls are biorthogonally and independently stretching or shrinking at arbitrary acceleration rates. In particular, we search for equilibrium solutions (steady flows) that are exact solutions of the Navier–Stokes equations under the assumption of the self-similar ansatz. We aim at providing a comprehensive and detailed description of possible equilibria by means of a highly accurate Legendre spectral spatial discretization of the Navier–Stokes self-similar boundary value problem, followed by a robust pseudo-arclength Newton–Krylov continuation method,

capable of tracking all solutions and their potential bifurcations. The use of spectral methods is particularly convenient in this case due to the simplicity of the geometry and boundary conditions, allowing for an exponential (or spectral) convergence of the discretized solutions.

This paper is structured as follows. Section II is devoted to the mathematical formulation of the problem, where the self-similar ansatz is introduced and the governing system of nonlinear partial differential equations is obtained. Section II also introduces the symmetry transformations that leave invariant the domain, the boundary conditions, and the self-similarity of the solution. The spectral Legendre spatial discretization of the aforementioned partial differential equations is described in detail in Sec. III. Section IV is focused on the search of steady flow solutions for moderate stretching–shrinking rates of the plates. Section V describes the mechanism by which new and old solutions are created and annihilated when the stretching–shrinking rates are increased and, in particular, the role of codimension-2 cusp bifurcations in such mechanism. Finally, Sec. VI summarizes the main findings of the current exploration.

II. MATHEMATICAL FORMULATION

We consider a viscous fluid of kinematic viscosity ν and density ρ confined between two infinite parallel plates separated by a distance $2h$, as depicted in Fig. 1(a). The problem is formulated in Cartesian coordinates (x^*, y^*, z^*), where starred variables henceforth stand for dimensional quantities. In this coordinate system, the motion of the fluid between the parallel plates is described by the velocity field $\mathbf{u}^* = (u^*, v^*, w^*)$. As shown in Fig. 1(a), the lower and upper plates are located at the *wall-normal* coordinates $z^* = \pm h$, linearly stretching along the x^* and y^* coordinates, respectively. The velocities of the fluid on the lower and upper impermeable plates are

$$u^*(x^*, y^*, -h) = ax^*, \qquad v^*(x^*, y^*, -h) = 0, \qquad w^*(x^*, y^*, -h) = 0, \tag{1}$$

$$u^*(x^*, y^*, h) = 0, \qquad v^*(x^*, y^*, h) = by^*, \qquad w^*(x^*, y^*, h) = 0, \tag{2}$$

where a and b are the strain rates of stretching along the x^* and y^* axes, respectively.

The problem is rendered nondimensional after using h, h^2/ν, ν/h, and $\rho\nu^2/h^2$ as units of length, time, velocity, and pressure, respectively, leading to the dimensionless incompressible Navier–Stokes equations,

$$\nabla \cdot \mathbf{u} = 0, \qquad \partial_t \mathbf{u} + (\mathbf{u} \cdot \nabla)\mathbf{u} = -\nabla p + \nabla^2 \mathbf{u}. \tag{3}$$

In dimensionless coordinates, the boundary conditions read

$$u(x, y, -1) = \frac{ah^2}{\nu} x \equiv \sigma_- x, \quad v(x, y, -1) = 0, \quad w(x, y, -1) = 0, \tag{4}$$

$$u(x, y, 1) = 0, \quad v(x, y, 1) = \frac{bh^2}{\nu} y \equiv \sigma_+ y, \quad w(x, y, 1) = 0, \tag{5}$$

where the new dimensionless quantities $\sigma_- = ah^2\nu^{-1}$ and $\sigma_+ = bh^2\nu^{-1}$ introduced in (4) and (5) measure the strain rates of the lower and upper plates, respectively. In what follows, we assume the solenoidal self-similar ansatz,

$$u(x, y, z, t) = xf'(z, t), \; v(x, y, z, t) = yg'(z, t), \; w(x, y, z, t) = -(f + g). \tag{6}$$

Formal substitution of (6) into the incompressible Navier–Stokes equations (3) yields the nonlinearly coupled relations,

$$f''' + (f + g)f'' - f'^2 - \partial_t f' = \beta_1, \tag{7a}$$

$$g''' + (f + g)g'' - g'^2 - \partial_t g' = \beta_2, \tag{7b}$$

where a prime denotes differentiation with respect to the nondimensional wall-normal coordinate z and β_1 and β_2 are constants to be determined. The corresponding pressure distribution is

$$p(x, y, z, t) = \frac{1}{2}(\beta_1 x^2 + \beta_2 y^2) - f' - g' - \frac{1}{2}(f + g)^2 + \partial_t \int (f + g)dz. \tag{8}$$

Assuming zero mass-flux along finite vertical planes parallel to the x and y axes, the solutions f and g of system (7) satisfy the boundary conditions,

$$f'(-1) = \sigma_-, \quad f(-1) = 0, \quad f(1) = 0, \quad f'(1) = 0, \tag{9a}$$

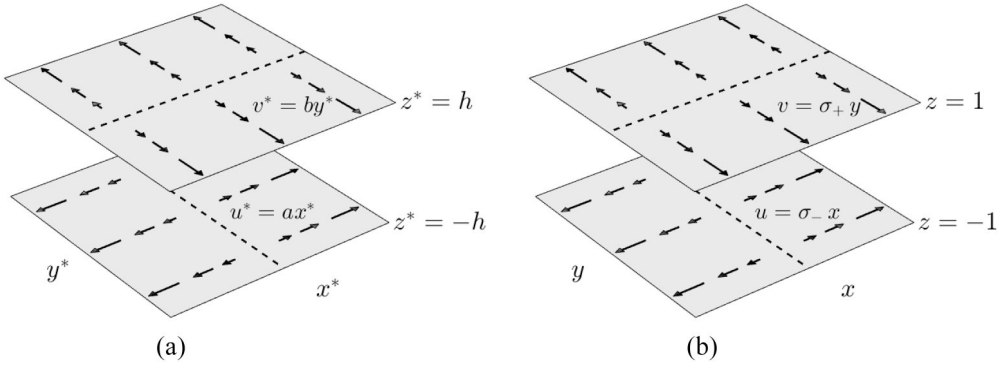

FIG. 1. Schematics of the problem: (a) in the dimensional form and (b) using non-dimensional variables.

$$g'(-1) = 0, \quad g(-1) = 0, \quad g(1) = 0, \quad g'(1) = \sigma_+. \tag{9b}$$

Following Marques *et al.* (2017), we introduce the two alternative parameters,

$$\sigma_+ = R\cos\alpha, \qquad \sigma_- = R\sin\alpha, \tag{10}$$

where $R = \sqrt{\sigma_+^2 + \sigma_-^2}$ is the Reynolds number and $0 \le \alpha \le 2\pi$ measures the relative strength of the two stretching walls. This gives rise to four regions

Region 1. $0 \le \alpha \le \pi/2$ (top stretches and bottom stretches)
Region 2. $\pi/2 \le \alpha \le \pi$ (top shrinks and bottom stretches)
Region 3. $\pi \le \alpha \le 3\pi/2$ (top shrinks and bottom shrinks)
Region 4. $3\pi/2 \le \alpha \le 2\pi$ (top stretches and bottom shrinks)

For purposes of integration, we take the derivative of (7) to obtain the eighth order system,

$$\partial_t f'' = f^{iv} + (f+g)f''' - (f'-g')f'', \tag{11a}$$
$$\partial_t g'' = g^{iv} + (f+g)g''' + (f'-g')g'', \tag{11b}$$

and calculate the pressure gradients from any of the relevant equations as

$$\beta_1 = f'''(1) = f'''(-1) - 1, \qquad \beta_2 = g'''(-1) = g'''(1) - 1. \tag{12}$$

Relations for the x and y directed wall shear stresses at the upper and lower walls are given in the nondimensional form (unit $\rho\nu^2/h^2$) as

$$\tau_x = \tau_{xz} = xf''(\pm 1), \qquad \tau_y = \tau_{yz} = yg''(\pm 1). \tag{13}$$

We have used the dimensional expression

$$\tau_{ij}^* = \mu(\partial_i u_j + \partial_j u_i)^* = \frac{\rho\nu^2}{h^2}(\partial_i u_j + \partial_j u_i) = \frac{\rho\nu^2}{h^2}\tau_{ij}. \tag{14}$$

Assuming that the flow is steady, and neglecting the nonlinear terms appearing in (11), the solution must satisfy $f^{iv} = g^{iv} = 0$. In this case, we obtain the third order polynomials,

$$f_0(z) = \frac{\sigma_-}{4}(z-1)^2(z+1) = \frac{R\sin\alpha}{4}(z^3 - z^2 - z + 1), \tag{15a}$$

$$g_0(z) = \frac{\sigma_+}{4}(z+1)^2(z-1) = \frac{R\cos\alpha}{4}(z^3 + z^2 - z - 1), \tag{15b}$$

that lead to the base *Stokes* flow,

$$u_0(x,z) = x\frac{R\sin\alpha}{4}(3z^2 - 2z - 1),$$
$$v_0(y,z) = y\frac{R\cos\alpha}{4}(3z^2 + 2z - 1), \tag{16a}$$

$$w_0(x,y,z) = \frac{R}{4}(1-z^2)[\sin\alpha(z-1) + \cos\alpha(z+1)], \tag{16b}$$

depicted in Fig. 2 for $R = 8$ and selected values of α. This base flow is not a solution of the Navier–Stokes equations and the advection term modifies the flow, as can be seen by comparing the base flow in Fig. 2 with the steady solution A_1 in Fig. 5, which is the self-similar solution of the Navier–Stokes equations at $R = 8$ that smoothly connects with the base flow for $R \to 0$. This connection is clearly shown in Fig. 5, where the U and V components of the A_1 solution are very similar to the Stokesian profiles u_0 and v_0, respectively, shown in Fig. 2. However, the effects of the advection already lead to noticeable differences in the wall-normal components W and w_0, particularly for $\alpha = \pi$ and $\alpha = \pi/2$.

A. Symmetries

The domain, along with the governing equations (11), the boundary conditions (9), and the self-similar ansatz (6), is invariant with respect to the two specular reflections about the planes $x = 0$ and $y = 0$,

$$K_x : (x,y,z) \mapsto (-x,y,z), \qquad K_y : (x,y,z) \mapsto (x,-y,z). \tag{17}$$

The domain and governing equations (but not the boundary conditions) satisfy the additional reflectional symmetry about the mid plane,

$$K_z : (x,y,z) \mapsto (x,y,-z). \tag{18}$$

In order to get the correct direction of the velocities on the domain boundary, we can compose this reflection with a reflection about the

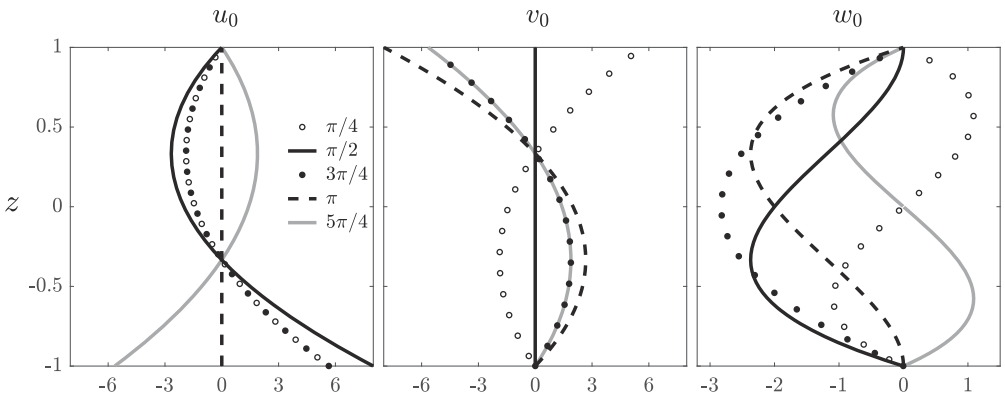

FIG. 2. Structure of the base Stokes flow (16) at $R = 8$ for the α values indicated. Panels show velocity profiles of u_0, v_0, and w_0 of (16) at $x = 1$ and $y = 1$.

plane bisector of the first quadrant, $x = y$, resulting in the rotation of π around the straight line $x = y$ and $z = 0$,

$$H : (x, y, z) \mapsto (y, x, -z). \tag{19}$$

This symmetry operation leaves invariant the domain and governing equations and exchanges σ_+ and σ_- (or what is the same, changes α into $\pi/2 - \alpha$). It is, therefore, a true symmetry of the problem for the particular cases $\sigma_+ = \sigma_-$, i.e., for $\alpha = \pi/4$ and $5\pi/4$.

According to the previous considerations, the induced actions of the symmetries on the velocity field are

$$K_x : [u, v, w](x, y, z, t; R, \alpha) \mapsto [-u, v, w](-x, y, z, t; R, \alpha), \tag{20a}$$

$$K_y : [u, v, w](x, y, z, t; R, \alpha) \mapsto [u, -v, w](x, -y, z, t; R, \alpha), \tag{20b}$$

$$H : [u, v, w](x, y, z, t; R, \alpha) \mapsto [v, u, -w](y, x, -z, t; R, \pi/2 - \alpha). \tag{20c}$$

The self-similar ansatz (6) is left invariant by K_x and K_y: $K_x\mathbf{u} = K_y\mathbf{u} = \mathbf{u}$. The only non-trivial action that remains in the self-similar formulation is the half-turn H whose square is the identity. The action of H on f and g is

$$H : [f, g](z, t; R, \alpha) \mapsto [-g, -f](-z, t; R, \pi/2 - \alpha). \tag{21}$$

As a consequence of the H-symmetry, from any solution for (R, α), another solution for $(R, \pi/2 - \alpha)$ is obtained. Therefore, it is sufficient to compute the solutions for $\alpha \in [\pi/4, 5\pi/4]$ and then apply the H symmetry to obtain the solutions in the whole interval $\alpha \in [0, 2\pi]$.

It is convenient to represent the velocity field of a given solution by plotting the z-profiles $\mathbf{u}(1, 1, z, t)$,

$$\mathbf{u}(1, 1, z, t) = (U(z, t), V(z, t), W(z, t)) = (f', g', -f - g). \tag{22}$$

From them, the whole velocity field at any (x, y) value is obtained by using (6). The action of H on (U, V, W) is

$$H : [U, V, W](z, t; R, \alpha) \mapsto [V, U, -W](-z, t; R, \pi/2 - \alpha). \tag{23}$$

Another useful feature of the flow is its *helicity*, defined as

$$h = \mathbf{u} \cdot (\nabla \times \mathbf{u}), \tag{24}$$

which is a pseudo-scalar (i.e., it changes sign under reflections K_x and K_y), and it is a true scalar for rotations H. For a self-similar solution, the expression of h is

$$h(x, y, z, t) = xy(g' f'' - f' g''). \tag{25}$$

Its symmetry properties are

$$h(x, y, z, t; R, \alpha) = -h(-x, y, z, t; R, \alpha) = -h(x, -y, z, t; R, \alpha), \tag{26a}$$

$$H : h(x, y, z, t; R, \alpha) \mapsto h(y, x, -z, t; R, \pi/2 - \alpha). \tag{26b}$$

III. SPECTRAL LEGENDRE DISCRETIZATION

Henceforth, in this study, we seek steady solutions of (11), satisfying

$$f^{iv} + (f + g) f''' - (f' - g') f'' = 0, \tag{27a}$$

$$g^{iv} + (f + g) g''' + (f' - g') g'' = 0, \tag{27b}$$

where $f(z)$ and $g(z)$ are functions defined within the domain $z \in [-1, 1]$ that satisfy the boundary conditions

$$f(-1) = 0,\ f'(-1) = R \sin\alpha,\ f(1) = 0,\ f'(1) = 0 \tag{28}$$

and

$$g(-1) = 0,\ g'(-1) = 0,\ g(1) = 0,\ g'(1) = R \cos\alpha. \tag{29}$$

To simplify the numerical setting, we consider the splittings

$$f(z) = f_0(z) + F(z),\ g(z) = g_0(z) + G(z), \tag{30}$$

where $f_0(z)$ and $g_0(z)$ constitute the basic Stokes solution (15) satisfying the boundary conditions (28) and (29) and $F(z)$ and $G(z)$ are deviations from the basic flow satisfying Dirichlet–Neumann homogeneous boundary conditions,

$$F(\pm 1) = G(\pm 1) = F'(\pm 1) = G'(\pm 1) = 0. \tag{31}$$

After introducing (30) in (27), the BVP reads

$$\begin{aligned} &F^{iv} + (f_0 + F + g_0 + G)(f_0''' + F''') \\ &\quad - (f_0' + F' - g_0' - G')(f_0'' + F'') = 0, \\ &G^{iv} + (f_0 + F + g_0 + G)(g_0''' + G''') \\ &\quad + (f_0' + F' - g_0' - G')(g_0'' + G'') = 0, \end{aligned} \tag{32}$$

or simply

$$\mathbf{N}(F, G, f_0, g_0) = \begin{bmatrix} N_1(F, G, f_0, g_0) \\ N_2(F, G, f_0, g_0) \end{bmatrix} = \begin{bmatrix} 0 \\ 0 \end{bmatrix}, \tag{33}$$

where N_1 and N_2 stand for nonlinear differential operators acting on the sought functions F and G, implicitly depending on the Stokes base fields f_0 and g_0. We discretize the nonlinear differential system (32) using spectral expansions of the form

$$\begin{bmatrix} F(z) \\ G(z) \end{bmatrix} = \sum_{m=0}^{M} a_m \Phi_m^{(1)}(z) + b_m \Phi_m^{(2)}(z), \tag{34}$$

where

$$\Phi_m^{(1)}(z) = \begin{bmatrix} \phi_m(z) \\ 0 \end{bmatrix},\ \Phi_m^{(2)}(z) = \begin{bmatrix} 0 \\ \phi_m(z) \end{bmatrix},\ \phi_m(z) = (1 - z^2)^2 P_m(z) \tag{35}$$

and where $P_m(z)$ is the mth Legendre polynomial. We introduce the inner Hermitian product between two arbitrary vector fields $\Psi(z) = [\psi_1(z)\ \psi_2(z)]^{\mathrm{T}}$ and $\Theta(z) = [\theta_1(z)\ \theta_2(z)]^{\mathrm{T}}$,

$$(\Psi, \Phi) \doteq \int_{-1}^{1} \Psi(z) \cdot \Theta(z)\, dz. \tag{36}$$

The Galerkin formulation consists in formally substituting the spectral expansion (34) in (33) and projecting on the set of quasi-orthogonal vector fields $\Phi_m^{(1)}$ and $\Phi_m^{(2)}$ defined in (35). These Hermitian products are computed with a Gauss–Legendre quadrature, which provides a maximum exactness with a reduced number of nodes (Quarteroni *et al.*, 2010), and the spectral expansion is evaluated on the corresponding nodes so that the wall-normal integral can be accurately computed. This results in an algebraic system of nonlinear equations for the spectral coefficients $\mathbf{a} = [a_0 a_1 \cdots a_M]$ and $\mathbf{b} = [b_0 b_1 \cdots b_M]$, that is,

$$\begin{aligned} \left(\Phi_m^{(1)}, \mathbf{N}(F, G, f_0, g_0)\right) &= \mathcal{N}_1(\mathbf{a}, \mathbf{b}, R, \alpha) = 0, \\ \left(\Phi_m^{(2)}, \mathbf{N}(F, G, f_0, g_0)\right) &= \mathcal{N}_2(\mathbf{a}, \mathbf{b}, R, \alpha) = 0. \end{aligned} \tag{37}$$

The above system defines $\mathbf{a}$ and $\mathbf{b}$ as implicit functions of R and α. All derivatives in the wall-normal direction have been computed by means of differentiation matrices based on Legendre nodes (Meseguer, 2020). System (37) is solved using matrix-free Newton–Krylov methods (Kelley, 2003) that only require the action of the Jacobian operator instead of the full matrix typically required by classical Newton–Raphson methods. The numerical solution of system (37) is particularly challenging in the neighborhood of folds or cuspidal points, where the Jacobian is extremely ill-conditioned. All the solutions of system (37) reported henceforth in the present work are computed using $M = 50$ Legendre polynomials and converged to the tolerance condition $\sqrt{\mathcal{N}_1^2 + \mathcal{N}_2^2} < 10^{-12}$, which ensures reliable results for all bifurcations and singular points, as shown in the Appendix. The solutions found have been subsequently tracked (homotopic transformations) in the two-dimensional (α, R) parameter space by means of pseudo-arclength continuation methods, Kuznetsov (2004). It is worth mentioning that these methods are specially challenging when a branch approaches a critical point, such as cusps or folds, as the Jacobian matrix is ill-conditioned near to singular points. The homotopic methods employed in the present work, along with complementary methodologies to identify saddle-node (fold) bifurcations or cusp points, have been previously used successfully for the continuation of equilibria in extensional planar and cylindrical geometries (Marques *et al.*, 2017 and Marques and Meseguer, 2019) and also in more generic shear or annular hydrodynamic and hydromagnetic flows (Meseguer *et al.*, 2009; Deguchi *et al.*, 2014; Ayats *et al.*, 2020a; and Ayats *et al.*, 2020b).

IV. FAMILIES OF STEADY SOLUTIONS FOR LOW-MODERATE *R*

We start the exploration of steady solutions by reproducing the results of a former analysis carried out in Wang and Wu (1995) for a two-dimensional channel, where one of the plates stretches at a constant rate and the other remains stationary. In our formulation, Wang and Wu's problem can therefore be recovered by setting in system (37) $\alpha = 0$ (top plate stretching in the y-direction and the lower plate being stationary) or $\alpha = \pi/2$ (lower plate stretching in the x-direction and the upper plate being stationary). Figure 3 shows the continuation curves of all identified branches for $\alpha = 0$ as a function of the Reynolds number within the range $R \in [-20, 110]$. One

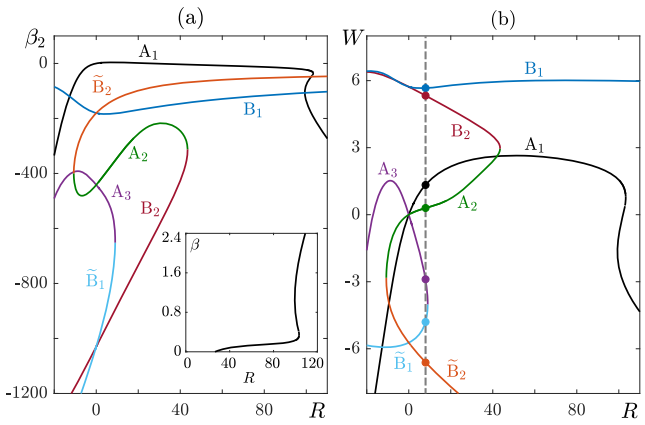

FIG. 3. Continuation of solution branches for $\alpha = 0$. In black, Wang and Wu's (A_1) solution branch formerly reported in the study of Wang and Wu (1995). (a) Pressure factor β_2 [the inset shows the normalized factor $\beta = -\beta_2/R$, following Fig. 2 in the study of Wang and Wu (1995)]. (b) Wall-normal velocity W at mid-plane $z = 0$. A gray dashed vertical line has been placed at $R = 8$, along with color coded bullets, to guide the eye in the α-unfolding of the solution branches, depicted in Fig. 4.

of these branches, namely, A_1 (black curves in Fig. 3) is the solution branch found in the study of Wang and Wu (1995). For consistency, Fig. 3(a) also includes an inset plot depicting Wang and Wu's solution in terms of the normalized pressure factor $\beta = -\beta_2/R$ used in their analysis, showing a perfect agreement with the zoom in of branches II and III detailed in Fig. 2 in the study of Wang and Wu (1995). The analysis carried out in the study of Wang and Wu also studied the flow for negative acceleration (shrinking) of one of the plates, that is, for $R < 0$. In our computations, branch A_1 has also been continued for negative values of the Reynolds number. In particular, Fig. 3(a) shows branch A_1 intercepting the ordinate $\beta_2 = -334.4$ for $R = -20$, leading to a pressure factor $\beta = -16.7$ that

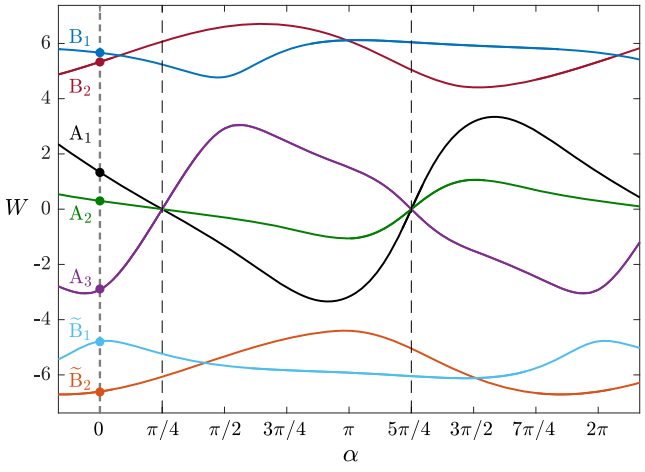

FIG. 4. Wall-normal velocity W at mid plane $z = 0$ corresponding to the families of steady solutions found for $R = 8$. A dashed gray vertical line has been placed to guide the eye when identifying the unfolded branches shown in Fig. 3(b) by color coded bullets.

is in very good agreement with the value of β showed in Fig. 2 in the study of Wang and Wu (1995).

The other branches appearing in Fig. 3 have been found after performing a comprehensive exploration of solutions of system (37) for different values of the parameter α and tracking them back to $\alpha = 0$ via pseudo-arclength continuation. Figure 4 illustrates this homotopic unfolding in α for a constant value of $R = 8$, which corresponds to continuations along the cross section depicted as a dashed gray vertical line in Fig. 3(b). To guide the eye, color coded bullets have been placed along the gray dashed line in order to identify the unfolded branches. For $R = 8$, we have overall identified seven solution branches: $A_{1,2,3}$, $B_{1,2}$, and $\widetilde{B}_{1,2}$. Branches A_i are H-symmetric, while branches $\widetilde{B}_1$ and $\widetilde{B}_2$ are in fact H-symmetry-related to the B_1 and B_2, respectively: a reflection $z \to -z$ plus a reflection around $\alpha = \pi/4$ (and $5\pi/4$). Figures 5 and 6 illustrate panels of the velocity profiles U, V, and W of each one of the genuinely independent types of flows (i.e., not related through symmetry transformations) for $R = 8$ and for certain selected values of α, covering representative stretching–shrinking configurations of the top and bottom plates. For example, the case $\alpha = 0$ is not included since it can be recovered from the case $\alpha = \pi/2$ (after performing a suitable symmetry transformation), as illustrated before for the Wang and Wu case. All seven families of solutions are in general three-dimensional. However, branch A_1 solutions become two-dimensional for $\alpha = \pi/2$

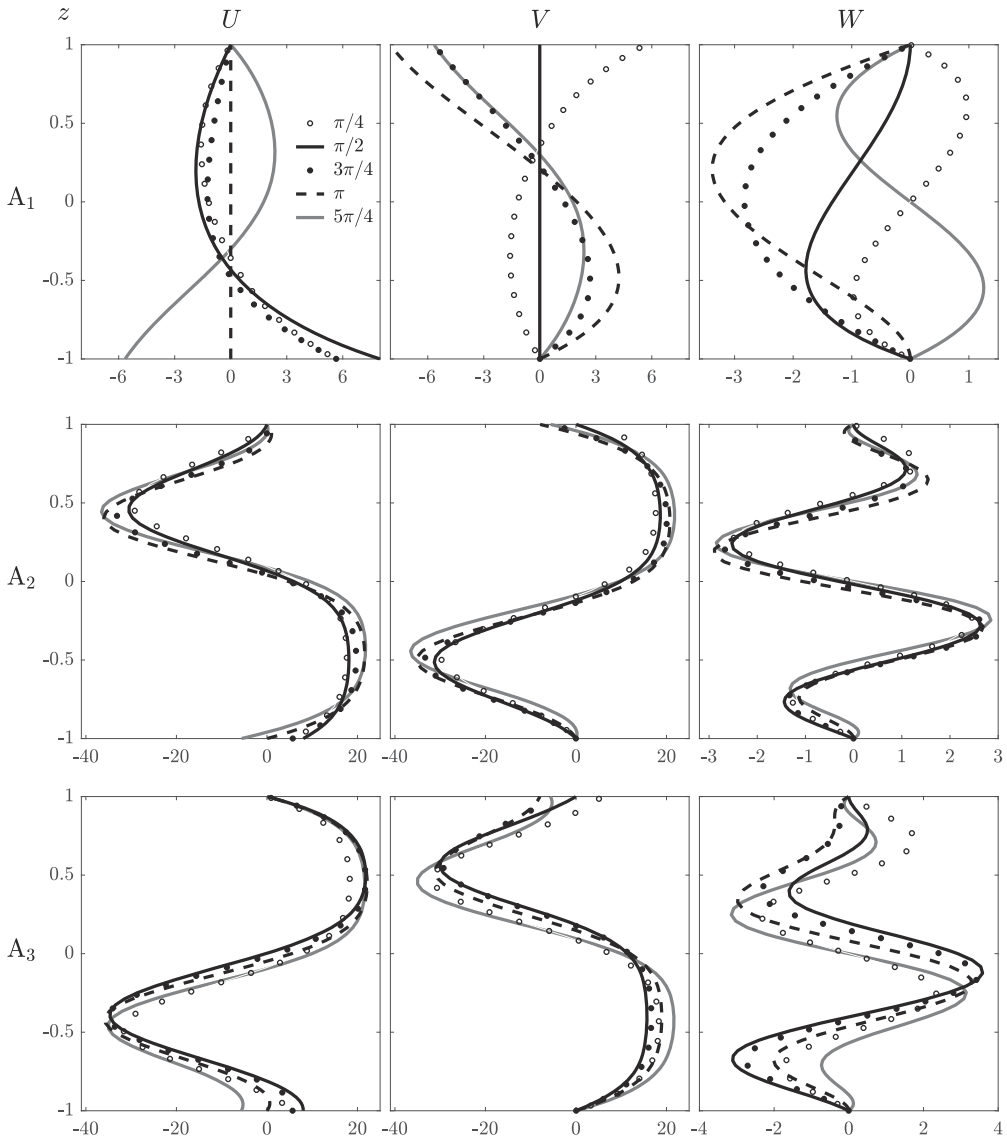

FIG. 5. Structure of the steady solutions A_1, A_2, and A_3 at $R = 8$ for the α values indicated. Panels show velocity profiles of U, V, and W.

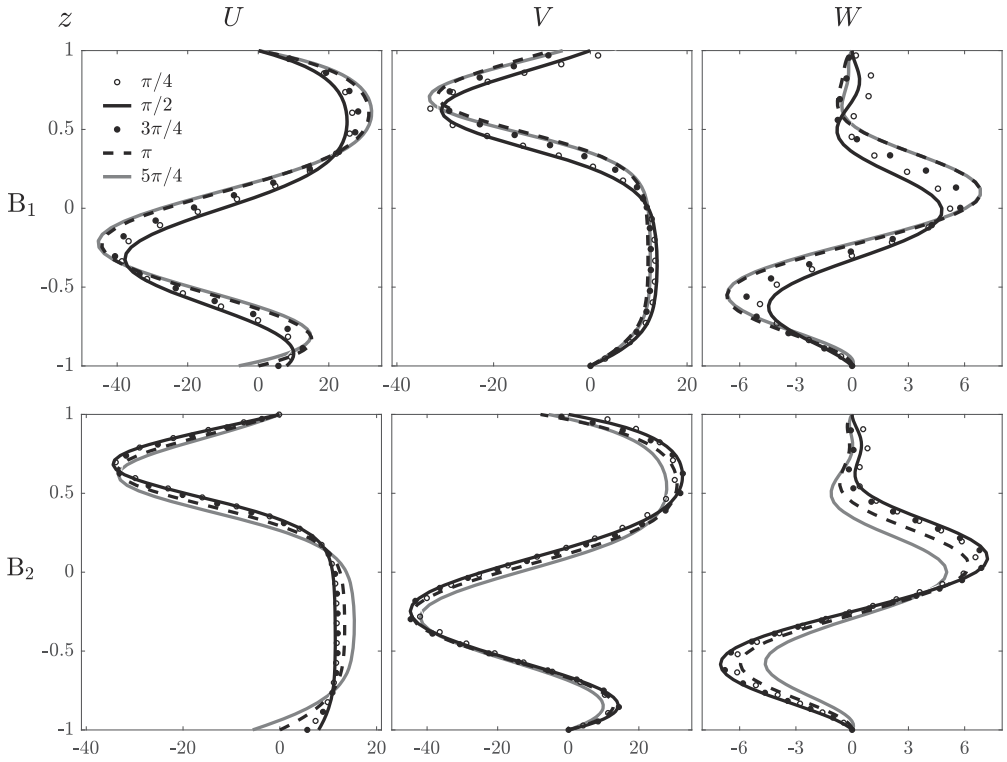

FIG. 6. Same as Fig. 5 for solutions B_1 and B_2. The profiles of the solutions $\widetilde{B}_{1,2}$ have not been included, as they are symmetry related to $B_{1,2}$.

(bottom plate stretching in the x-direction and the top plate being stationary) or $\alpha = \pi$ (top plate shrinking in the y-direction and the bottom plate being stationary). This is clearly reflected in the top panel of Fig. 5, where $V = 0$ for $\alpha = \pi/2$ and $U = 0$ for $\alpha = \pi$. A careful inspection of the speed profiles shown in panel A_1 of Fig. 5 reveals, as it has been stated in Sec. II, a remarkable similarity to those corresponding to the Stokes flow (16) previously shown in Fig. 2. In fact, the A_1 solution branch is actually the nonlinear continuation of the Stokesian flow when, after increasing the Reynolds number, the nonlinearities can no longer be neglected. Furthermore, Figs. 5 and 6 also reveal that all solution branches except A_1 exhibit their maximum and minimum values of velocities U and V inside the channel, significantly far from the walls and independent of the value of α. By contrast, the low relevance of the nonlinear term in the case of A_1 produces a simpler solution whose velocity profiles peaks are always governed by the walls. These nonlinear effects, already reported in the two-dimensional extensional channel flow Marques *et al.* (2017), allow disturbances coming from the boundaries that interfere with the velocity field and produce such kind of solutions.

To have more insight into the flow structure of these new families of solutions and to compare them with the Stokesian base flow, Fig. 7 depicts helicity h isocontours of these solutions over a cylinder of unit radius placed at $(x, y, z) = (0, 0, 0)$. A visual inspection of h confirms that all solutions satisfy the symmetry relations (26). It is worth mentioning that for $\alpha = \pi/4$, both the base Stokesian flow and the A_i solutions are self-symmetric: invariant under the $H-$rotation described in (26b). By contrast, the B_i solutions are not $H-$invariant: the symmetry transforms one branch into the other, $H: B_i \mapsto \widetilde{B}_i$. Similarly, Fig. 8 shows radial velocity v_r isocontours for the same cases previously depicted in Fig. 7. All solutions satisfy velocity field symmetries (20) in the same terms as the aforementioned for the helicity. As expected, solutions BF and A_1 are very similar, both having their maximum radial velocities located at the boundary planes. By contrast, the other solutions show intense internal return jets (in yellow) in the x and y directions. More remarkably, the maximum velocity of these jets is larger than the stretching velocity at the boundaries. A very similar phenomenon has recently been observed in flows arising in stretching pipes, where dominant axial jets appear in the center line of the pipe, and with velocities considerably larger than the ones induced near the stretching wall, Marques and Meseguer (2019).

In order to reveal the origin and fate of these and other solution branches, we have carefully tracked the number of solutions of system (37) throughout the two-dimensional parameter space (α, R). Figure 9(a) summarizes the results by depicting the parameter regions where a different number (boxed) of equilibrium solutions has been identified. These regions are delimited by boundaries (solid black curves) along which solutions are created or annihilated by means of a saddle-node bifurcation (fold) mechanism. Figure 9 has two vertical reflection symmetries, about $\alpha = \pi/4$ and $5\pi/4$, due to the symmetry H. The bifurcation curve starting at C_1 for $\alpha > 5\pi/4$ has a local minimum at the point F_1 (white bullet), located at the coordinates $(\alpha, R) = (4.54, 10.54)$. The bifurcation curve symmetric

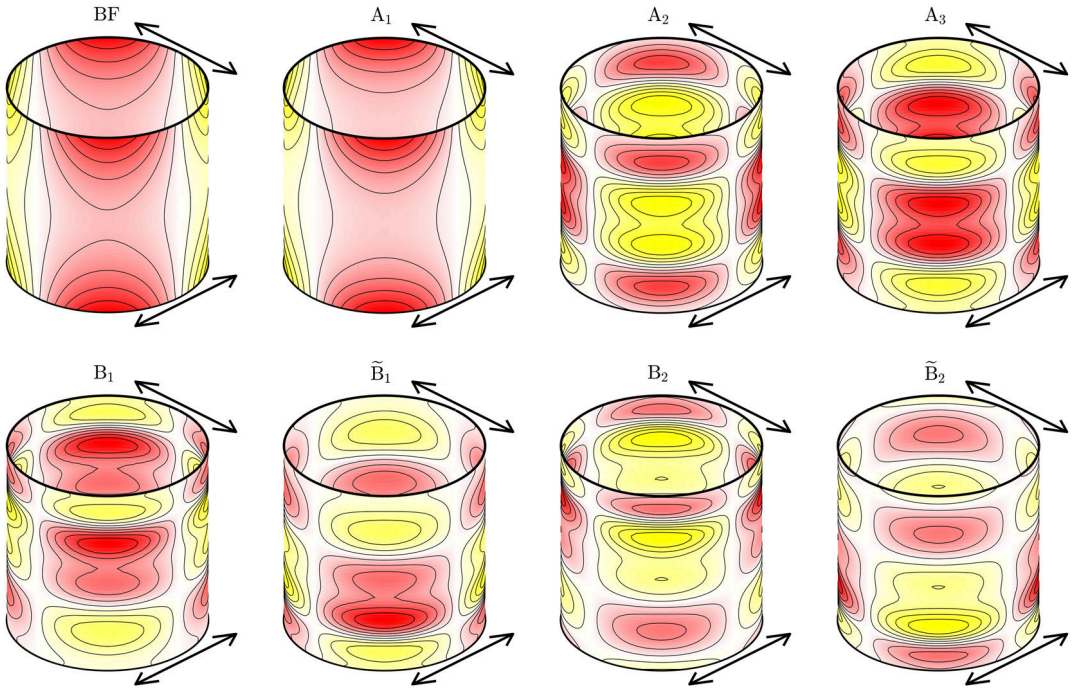

FIG. 7. Isocontours of helicity h over a cylinder of unit radius for base Stokes flow (BF) and solutions $A_{1,2,3}$, $B_{1,2}$, and $\widetilde{B}_{1,2}$. Red and yellow colors indicate positive and negative h values, respectively. All cases are for $R = 8$ and $\alpha = \pi/4$, top and bottom plates stretching with the same acceleration rate in the directions indicated by the arrows. For a correct interpretation, these projections are aligned with the symmetry plane $x = y$.

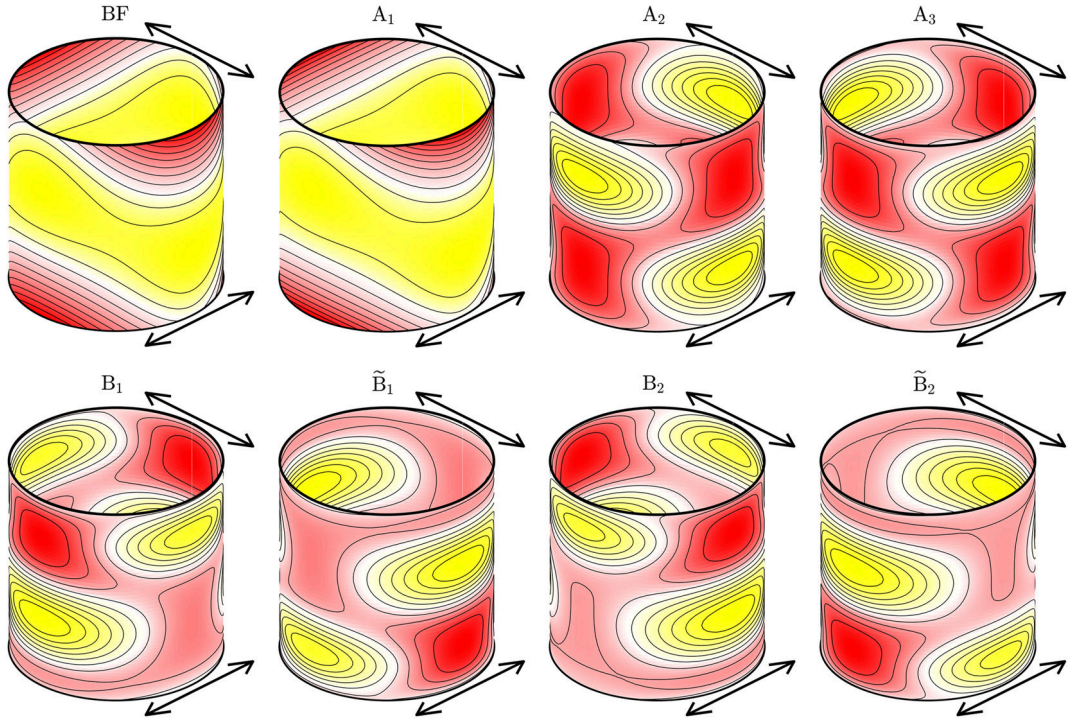

FIG. 8. Isocontours of radial velocity v_r for $R = 8$ and $\alpha = \pi/4$. Red and yellow colors indicate positive and negative values of v_r, respectively.

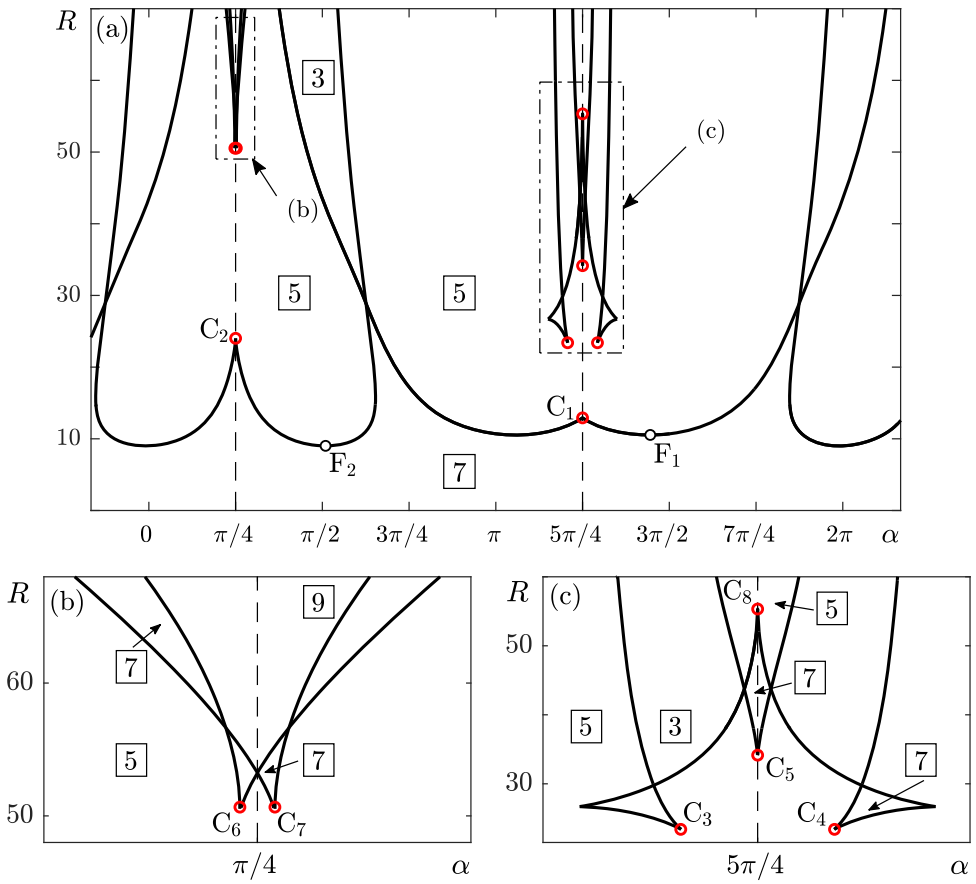

FIG. 9. (a) Explored domain in parameter space (α, R) indicating the number of equilibrium solutions (squared inset numbers) found in each region. (b) and (c) Detailed views of selected regions in (a). Dashed vertical symmetry lines are located at abscissas $\alpha = \pi/4$ and $\alpha = 5\pi/4$.

about $\alpha = 5\pi/4$ has the symmetric of the F_1 minimum at $\alpha = 3.31$ (not shown). The bifurcation curve starting at C_2 for $\alpha > \pi/4$ has its minimum at the point F_2, with coordinates $(\alpha, R) = (1.6, 9.019)$. The symmetric counterpart with respect $\alpha = \pi/4$ has the minimum at $\alpha = 0.0293$ or $\alpha = 6.2539$ due to the natural 2π-periodicity of the diagram. We have extended the α range beyond the interval $[0, 2\pi]$ in Fig. 9 to facilitate following the bifurcation curves. As a result, the aforementioned starting seven solutions exist for Reynolds numbers within the range $[0, 9.019]$.

For Reynolds numbers slightly below and above the critical value 9.019 and α near 0 or $\pi/2$, two of the seven solutions are lost, as it can be observed from Figs. 10(a) and 10(b), for $R = 9$ and $R = 10$, respectively. Specifically, in a neighborhood of $\alpha = \pi/2$ and $R = 9.019$, branches A_3 and B_1 exhibit a pinch, indicated by red vertical arrows in Fig. 10(a) for $R = 9$. These two branches eventually merge, annihilating two solutions in that neighborhood and creating two detached new branches that separate apart, as indicated by red horizontal diverging arrows in Fig. 10(b) for $R = 10$. As expected, the A_3 curve simultaneously merges with the symmetric $\widetilde{B}_1$ branch for $\alpha = 0$ or $\alpha = 2\pi$, also indicated by vertically converging red arrows in Fig. 10(a). For $R = 10$, other regions, away from $\alpha = 0, \pi/2, 2\pi$, may still have seven solutions. However, a slight increase in the Reynolds number beyond $R = 10.54$ also induces the loss of some of these solutions as well. In particular, branches A_2 and B_2 exhibit another pinch phenomenon for $R = 10.54$ in the neighbourhoods of $\alpha = 3\pi/2$ (also exhibited by branches A_2 and $\widetilde{B}_2$ near $\alpha = \pi$), as indicated by vertically converging blue arrows in Fig. 10(b). For $R = 10.8$, these two pairs of branches have already merged and destroyed two solutions near $\alpha = 3\pi/2$ and $\alpha = \pi$, eventually creating two detached independent connections that separate apart, as indicated by horizontal diverging blue arrows in Fig. 10(c). This mechanism of creation–annihilation of branch pairs is similar to the one recently observed in extensional planar or cylindrical flows, Marques *et al.* (2017) and Marques and Meseguer (2019).

V. CODIMENSION-2 CUSP BIFURCATION POINTS

When crossing the saddle-node bifurcation curves, two solutions merge and disappear. This is the generic situation in steady bifurcations of ODEs or PDEs. However, the presence of the symmetry H (symmetry group Z_2) for $\alpha = \pi/4$ and $5\pi/4$ modify the scenario. The generic steady bifurcation of a Z_2-symmetric solution ($\alpha = \pi/4$ or $5\pi/4$ fixed and increasing R) is a pitchfork. Here, three different solutions merge and only one survives after the

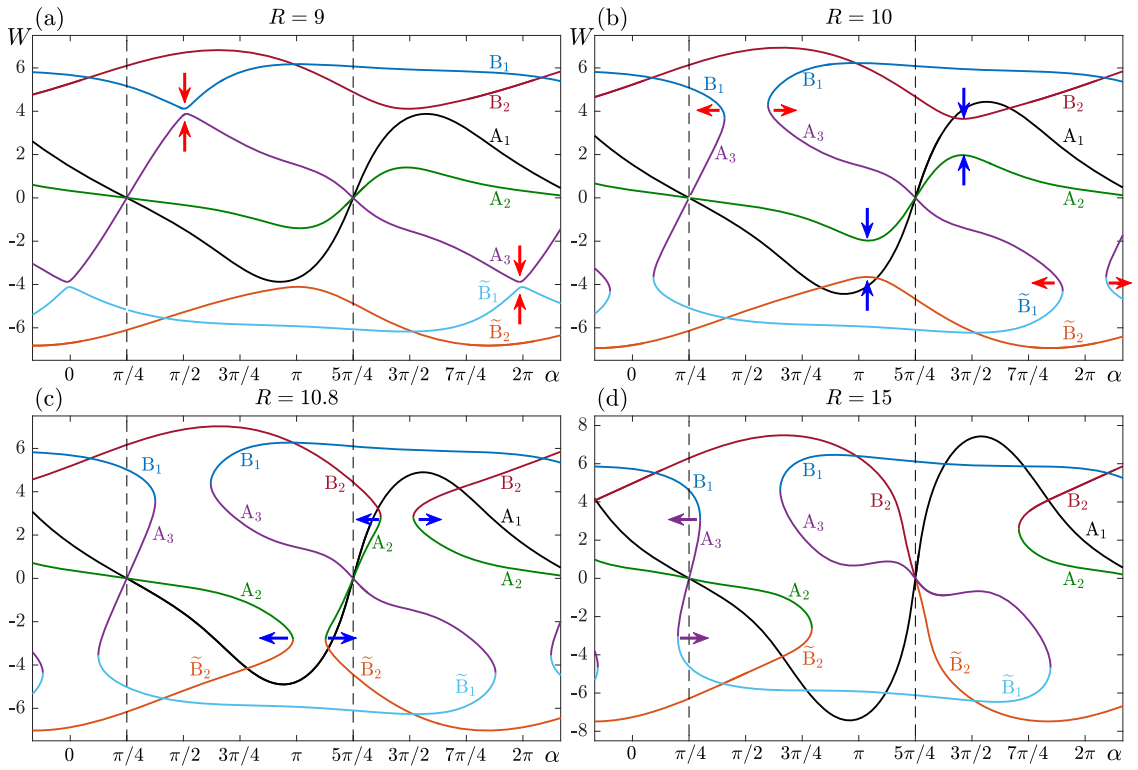

FIG. 10. (a)–(d) Continuations in α of the families of steady solutions for the indicated R values. Red and blue vertically converging and horizontally diverging arrows have been included to indicate the regions where pairs of solutions are lost. (d) Violet arrows indicate saddle-node bifurcations movements converging to cusp bifurcation point C_2.

bifurcation; the solution that remains is Z_2-symmetric, and the other two are symmetrically related, Kuznetsov (2004). What we observe in a neighborhood of $\alpha = \pi/4$ and $5\pi/4$ is a *cusp* bifurcation of codimension two. The cusp points C_1, C_2, C_5, and C_8 are of this type, with the symmetry H playing a critical role. Figures 10(c) and 10(d) illustrate the formation of the cusp C_1 located at $(\alpha, R) = (5\pi/4, 12.92)$. In Fig. 10(c), for $\alpha = 5\pi/4$, we see three solutions (B_2, A_2, and $\widetilde{B}_2$) on the same S-shaped bifurcation curve. When increasing R, the three solutions approach each other, merge at $R = 12.92$, and only one remains at larger R, as shown in Fig. 10(d), where the S-shaped curve has become a smooth univalued function. The same happens at cusp C_2 located at $(\alpha, R) = (\pi/4, 24.02)$. Figure 10(d) at $R = 15$ shows that the three solutions B_1, A_3, and $\widetilde{B}_1$ on the same S-shaped bifurcation curve approach [purple arrows in Fig. 10(d)] and merge at $R = 24.02$.

The two saddle-node bifurcation curves that meet at a cusp point are different. For example, at C_1, the saddle-node curve that has minimum F_1 (for $\alpha > 5\pi/4$) corresponds to the merging of B_2 and A_2, while the symmetric counterpart (for $\alpha < 5\pi/4$) corresponds to the merging of A_2 and $\widetilde{B}_2$. Two different saddle-node bifurcation curves can meet in the absence of symmetry (away from the lines $\alpha = \pi/4$ and $5\pi/4$), resulting also in a codimension-2 cusp bifurcation point without symmetry, Kuznetsov (2004). This is what happens at the cusp points C_3, C_4, C_6, and C_7.

For moderately larger Reynolds numbers, our parametric exploration reveals a remarkable increase in the complexity of the topology of equilibria. This feature is clearly shown in Figs. 9(a) and 9(c) for $R = 23.4$ and beyond, showing the presence of multiple cuspidal points, namely, C_3 and C_4 for $\alpha = 3.792$ and $\alpha = 4.062$, very close to their central value $\alpha = 5\pi/4$, respectively. These two symmetric cuspidal bifurcation points lead to two small regions inside which we may find seven equilibria again, as summarized in Fig. 9(c). Figures 11(a) and 11(b) are detailed views slightly below and above $C_{3,4}$ for $R = 22$ and $R = 25$, respectively. The simultaneous cusp bifurcations appear along branch A_1, bounded by two saddle-node bifurcations (white squares in Fig. 11), leading to the new solution branch A_4. As the Reynolds number is increased, Fig. 11(c) shows that A_1–A_4 and A_3 branches approach and exhibit a pinch near two of the saddle-nodes leading to an α-isolated A_1–A_3 branch, which is clearly depicted in Fig. 11(d). However, as this isolation reduces significantly, two of these seven solutions soon disappear again for $R > 30$.

Figure 12 shows the structure of the seven solutions indicated in blue in Fig. 11(d), coexisting for the same value of the parameters $(\alpha, R) = (4.18, 27)$ and including two solutions on the isolation. These solutions are close to but not equal to $\alpha = 5\pi/4$; therefore, none of them is H-symmetric. Comparing these solutions at $R = 27$ with the solutions at $R = 8$ shown in Fig. 8, there are two main differences. One is the increased strength of the internal return jets.

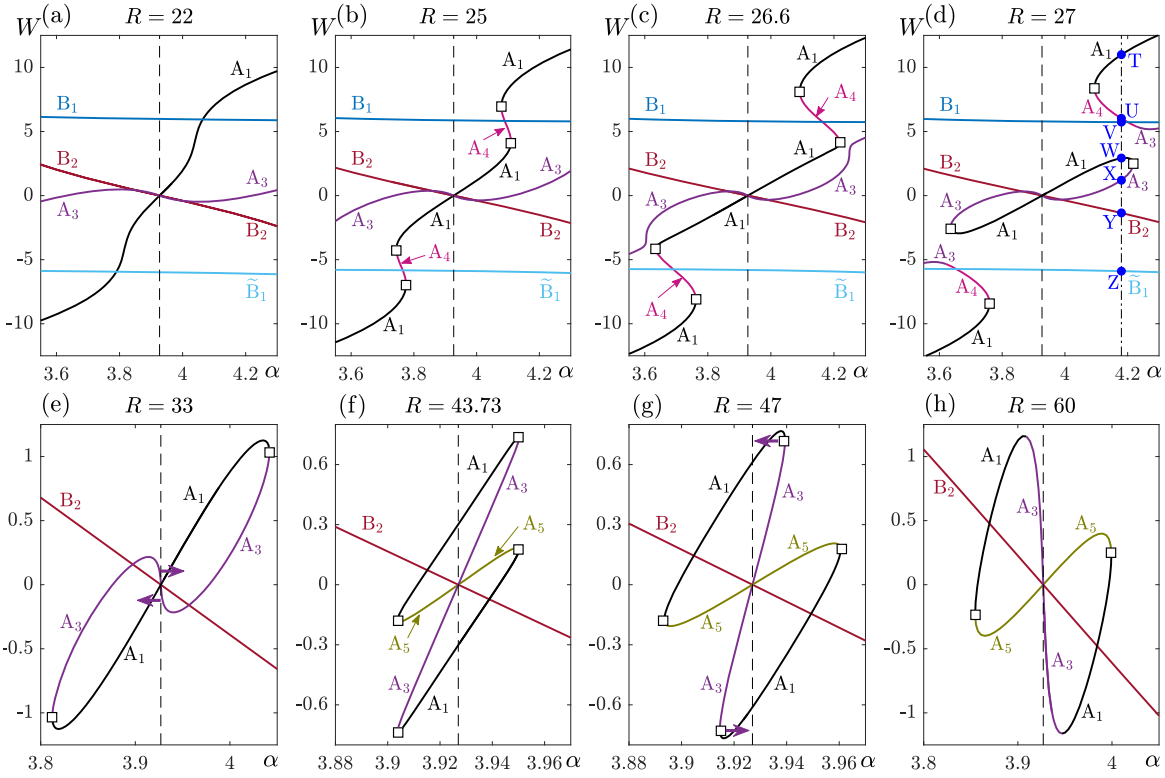

FIG. 11. Continuations in α in a neighborhood of $\alpha = 5\pi/4$ (dashed line) for the selected Reynolds number. (a)–(d) All solution branches corresponding to Fig. 9(c). (e)–(h) Detailed continuations of the isolated A_1–A_3 branch. White squares are saddle-node bifurcations and violet arrows indicate branch shifts leading to (e) C_5 and (g) C_8 cuspidal points for $\alpha = 5\pi/4$. (d) Blue symbols correspond to the seven solutions coexisting for the same parameter values $(\alpha, R) = (4.18, 27)$ that are described in the text and in Fig. 12.

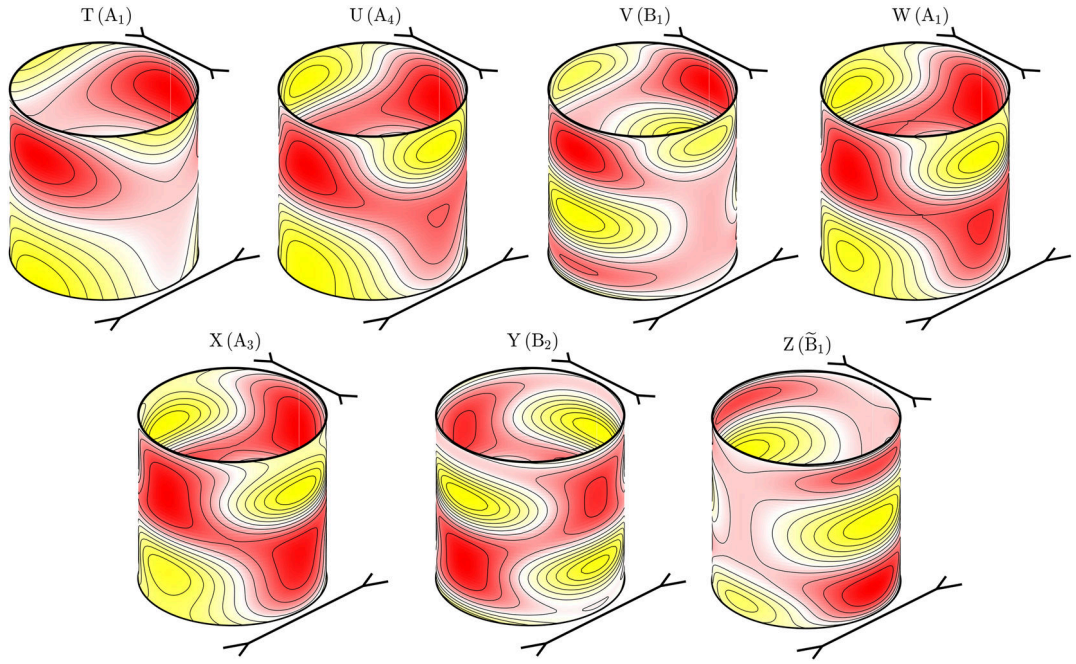

FIG. 12. Radial velocity v_r for solutions at $\alpha = 4.18$ and $R = 27$. Red and yellow colors indicate positive and negative v_r values, respectively.

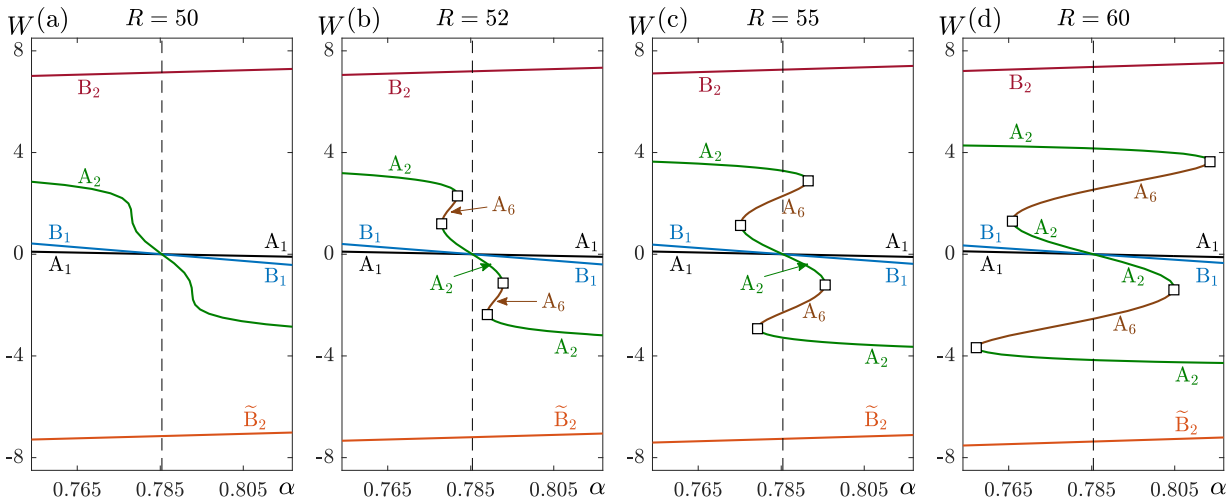

FIG. 13. (a)–(d) Continuations in α in a neighborhood of $\alpha = \pi/4$ (dashed line) for the selected Reynolds number. White squares indicate saddle-node bifurcations.

The other difference is that the number of jets increases; this is clearly seen in solutions V and Y, exhibiting four layers, two at the boundary planes and other two in the interior, with opposite radial velocity. This results in an increased shear stress between layers, which can be a source of dynamical instabilities. This increase in the number of layers and its strength has also been observed in two-dimensional planar channels, Marques *et al.* (2017), when the walls are simultaneously shrinking, as shown in Fig. 12. Notice that the solutions for $R = 8$ shown in Fig. 8 correspond to a stretching situation ($\alpha = \pi/4$).

For Reynolds numbers within the range $R \in [34.15, 55.34]$, and in a very narrow neighborhood of $\alpha = 5\pi/4$, seven solutions are available again. This region is bounded by two cusp points, namely, C_5 and C_8, located along the line $\alpha = 5\pi/4$, for $R = 33.73$ and $R = 55.34$, respectively. In fact, C_5 is the cusp bifurcation located along the α-isolated branch responsible for the appearance of a new solution branch, namely, A_5. Violet arrows in Fig. 11(e) illustrate this process of solution creation by indicating branch displacements, and Fig. 11(f) depicts the isolation with these new A_5 solutions. If the Reynolds number is further increased, the outermost pair of saddle-node bifurcations move toward the symmetry line $\alpha = 5\pi/4$, indicated with violet arrows in Fig. 11(g), and merge together forming C_8. As a result, in a neighborhood of $\alpha = 5\pi/4$ and for $R > 55.34$, five solutions remain [see Fig. 11(h) for $R = 60$]. This increase in complexity in the topology of equilibria when the boundaries are shrinking has also been recently reported in flows arising inside contracting pipes and two-dimensional parallel plates, Marques *et al.* (2017) and Marques and Meseguer (2019).

We end our analysis by describing the last pair of symmetric cuspidal points that simultaneously appear in a neighborhood of $\alpha = \pi/4$ when both plates are stretching at the same higher acceleration rate. Figure 9(a) depicts these cuspidal points for $R = 50.49$, namely, C_6 and C_7 located at $\alpha = 0.7784$ and $\alpha = 0.7924$, respectively. These two cusps are so close that an inset has been also provided in Fig. 9(b) to facilitate visualization. This pair of symmetric cusps is also responsible for generation of two more solutions in an extremely narrow region of the parameter space. In this case, however, increasing the Reynolds number leads to the creation of a total number of nine equilibria. For $R \lesssim 50.49$, only five solution branches coexist within the interval $\alpha \in [0.755, 0.815]$, as shown, for example, in Fig. 13(a) for $R = 50$. For $R \gtrsim 50.49$, after the cuspidal points C_6 and C_7 appear along branch A_2, a new solution branch A_6 is born, bounded by two saddle-node points, depicted as white squares in Fig. 13(b) for $R = 52$. Further increase in the Reynolds number leads to a separation of these saddle-node points, widening the range of α values for which up to nine solution branches coexist, as depicted in Figs. 13(c) and 13(d) in a neighborhood of $\alpha = \pi/4$ for $R = 55$ and $R = 60$, respectively. Table I summarizes the location of the two fold and eight cuspidal points identified in this exploration.

TABLE I. Locations of fold and cuspidal points in Fig. 9.

Point	α	R
F_1	4.54	10.54
F_2	1.6	9.019
C_1	$5\pi/4$	12.92
C_2	$\pi/4$	24.02
C_3	3.792	23.40
C_4	4.062	23.40
C_5	$5\pi/4$	33.73
C_6	0.7784	50.49
C_7	0.7924	50.49
C_8	$5\pi/4$	55.34

VI. CONCLUSIONS

A comprehensive exploration of equilibrium flows arising between two parallel plates that stretch–shrink orthogonally and independently has been performed. The exploration has covered a wide range of stretching–shrinking acceleration rates. For moderately low Reynolds numbers, up to seven steady flows have been

identified. Three of these flows are genuinely independent, whereas two of the remaining four flows are related through rotational symmetry transformations. For higher Reynolds numbers, however, the number of equilibrium solutions may range between three and nine. For moderate Reynolds numbers, our exploration reveals that equilibria tend to be created or annihilated more likely when both plates are simultaneously shrinking. These new solutions are the result of codimension-2 cusp bifurcations. Similar cuspidal points have been identified for higher Reynolds numbers when both plates are simultaneously stretching. In this case, the cusps only favor the creation of new solutions. All cusp bifurcations and new solutions are close to the H-symmetry lines, corresponding to stretching or shrinking planes with the same acceleration rate. In fact, it is the breaking of the H-rotational symmetry that results in this plethora of new solutions and cusp bifurcations.

The presence of cuspidal points when the boundaries are shrinking is consistent with recent analyses carried out in cylindrical geometries and in two-dimensional channels [Marques *et al.* (2017) and Marques and Meseguer (2019)]. The natural continuation of the present work would be the exploration of the dynamical properties of the found solutions. This would require performing time integration of the original equations in order to clarify the linear and nonlinear stability of these solutions. However, these aspects are far from the scope of the present analysis.

ACKNOWLEDGMENTS

This work was supported by the Spanish MINECO, Grant Nos. FIS2017-85794-P and PRX18/00179, and the Generalitat de Catalunya, Grant No. 2017-SGR-785.

APPENDIX: SPECTRAL CONVERGENCE

All the solutions reported in the present study have been confirmed to satisfy *spectral convergence*, that is, the exponential decay of the coefficients a_m and b_m corresponding to the Legendre expansions (34). Figure 14 illustrates this property by depicting on a linear-log plot the modulus of these coefficients as function of m. Figure 14(a) shows the decay of the Legendre coefficients corresponding to the two-dimensional solution in the study of Wang and Wu (1995), shown in Fig. 3(a) for $R = 90$ and $\alpha = 0$. In this case, the lower plate is at rest, whereas the upper one is stretching at the maximum acceleration rate, inducing fluid motion in the y direction only, the u-component of the velocity therefore being zero. This is reflected in the almost negligible, to machine precision, magnitude of the a_m Legendre coefficients associated with the u-component of the flow. The v-component of the flow is governed by the b_m coefficients that show a clear exponential decay, covering nearly 14 orders of magnitude, as a distinctive characteristic of spectral convergence. Figure 14(b) corresponds to the Legendre coefficients of the solution $\mathrm{Z}(\widetilde{\mathrm{B}}_1)$ shown in Fig. 12 for $R = 27$. In this case, the fluid motion has non-zero components in the x and y directions and exhibits multiple inner jets. We have chosen this solution precisely because of its complexity, therefore demanding a higher number of Legendre modes. In this case, both coefficients also exhibit a very neat spectral convergence law, overall showing an exponential decay of early 12 orders of magnitude using $M = 50$ Legendre polynomials.

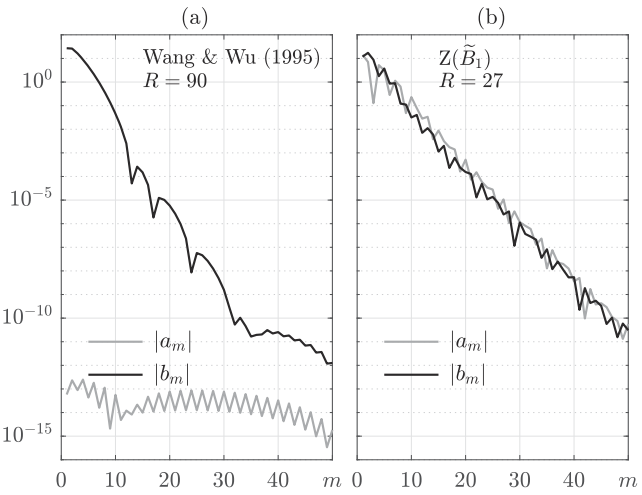

FIG. 14. Exponential convergence of the spectral Legendre expansions (34).

TABLE II. Locations of fold F_2 and cusp C_8 points in the (α, R)-plane as a function of the Legendre modes, M, used in the discretization. The cuspidal point appears along the symmetry line $\alpha = 5\pi/4$.

M	$R(\mathrm{F}_2)$	$\alpha(\mathrm{F}_2)$	$R(\mathrm{C}_8)$
20	9.018 980 591 6	1.598 160 358 3	55.350 699 461 5
30	9.019 014 407 7	1.598 148 910 0	55.335 942 271 4
40	9.019 014 378 8	1.598 148 820 9	55.335 956 884 1
45	9.019 014 380 3	1.598 148 821 3	55.335 956 243 6
50	9.019 014 379 3	1.598 148 821 5	55.335 956 727 3
55	9.019 014 379 3	1.598 148 821 3	55.335 956 112 2

The reliability of the Legendre spectral discretization used in this work has been tested by computing the coordinates of cuspidal and fold points and for a number of Legendre polynomials within the range $M \in [20, 55]$. Table II outlines this test, exhibiting an outstanding exponential convergence in the coordinates of the codimension-1 and 2 bifurcation points F_2 and C_8, respectively, as shown in Fig. 9. We can conclude that $M = 50$ Legendre polynomials already provides nearly ten exact figures in the critical R of the fold point and eight in the cuspidal one (located at $\alpha = 5\pi/4$). Increasing the number of Legendre polynomials does not improve the accuracy of the presented results, being overall more than satisfactory.

DATA AVAILABILITY

The data that support the findings of this study are available from the corresponding author upon reasonable request.

REFERENCES

Ayats, R., Deguchi, K., Mellibovsky, F., and Meseguer, A., "Fully nonlinear mode competition in magnetised Taylor–Couette flow," J. Fluid Mech. **897**, A14 (2020a).

Ayats, R., Meseguer, A., and Mellibovsky, F., "Symmetry-breaking waves and space-time modulation mechanisms in two-dimensional plane Poiseuille flow," Phys. Rev. Fluids **5**, 094401 (2020b).

Brady, J. F. and Acrivos, A., "Steady flow in a channel or tube with an accelerating surface velocity. An exact solution to the Navier–Stokes equations with reverse flow," J. Fluid Mech. **112**, 127–150 (1981).

Crane, L. J., "Flow past a stretching plate," Z. Angew. Math. Phys. **21**, 645–647 (1970).

Deguchi, K., Meseguer, A., and Mellibovsky, F., "Subcritical equilibria in Taylor–Couette flow," Phys. Rev. Lett. **112**, 184502 (2014).

Drazin, P. G. and Riley, N., *The Navier–Stokes Equations: A Classification of Flows and Exacts Solutions* (Cambridge University Press, Cambridge, 2006).

Espín, L. and Papageorgiou, D. T., "Flow in a channel with accelerating or decelerating wall velocity: A comparison between self-similar solutions and Navier–Stokes computations in finite domains," Phys. Fluids **21**, 113601 (2009).

Kelley, C., *Solving Nonlinear Equations With Newton's Method* (SIAM, 2003).

Kuznetsov, Y. A., *Elements of Applied Bifurcation Theory*, 3rd ed. (Springer, 2004).

Marques, F. and Meseguer, A., "Extensional and torsional pipe flow," Phys. Rev. Fluids **4**, 103908 (2019).

Marques, F., Meseguer, A., Mellibovsky, F., and Weidman, P., "Extensional channel flow revisited: A dynamical systems perspective," Proc. R. Soc. London, Ser. A **473**, 20170151 (2017).

Meseguer, A., *Fundamentals of Numerical Mathematics for Physicists and Engineers* (John Wiley & Sons, 2020).

Meseguer, A., Mellibovsky, F., Avila, M., and Marques, F., "Families of subcritical spirals in highly counter-rotating Taylor–Couette flow," Phys. Rev. E **79**, 036309 (2009).

Quarteroni, A., Sacco, R., and Saleri, F., *Numerical Mathematics* (Springer Science & Business Media, 2010), Vol. 37.

Wang, C.-A. and Wu, T.-C., "Similarity solutions of steady flows in a channel with accelerating walls," Comput. Math. Appl. **30**, 1–16 (1995).

Wang, C. Y., "The three-dimensional flow due to a stretching flat surface," Phys. Fluids **27**, 1915 (1984).

Wang, C. Y., "Review of similarity stretching exact solutions of the Navier–Stokes equations," Eur. J. Mech.: B/Fluids **30**, 475–479 (2011).

Waters, S. L., "Solute uptake through the walls of a pulsating channel," J. Fluid Mech. **433**, 193–208 (2001).

Waters, S. L., "A mathematical model for the laser treatment of heart disease," J. Biomech. **37**, 281–288 (2004).

Weidman, P. and Ishak, A., "Multiple solutions of two-dimensional and three-dimensional flows induced by a stretching flat surface," Commun. Nonlinear Sci. Numer. Simul. **25**, 1–9 (2015).

4.4 Further research

In Ayats *et al.* (2021), we searched for steady solutions in the parameter space (α, R). Additionally, direct numerical simulation and Arnoldi eigenvalue routines have been developed to study the time evolution and the stability of the reported solutions, respectively. Section §4.4.1 shows the temporal discretisation of the nonlinear system of equations, whereas section §4.4.2 is devoted to the linear stability analysis scheme.

4.4.1 Temporal discretisation

To study the dynamical properties of the flow, we start from the 8^{th} order system

$$\partial_t f'' = f^{iv} + (f+g)f''' - (f'-g')f'', \tag{4.1a}$$

$$\partial_t g'' = g^{iv} + (f+g)g''' + (f'-g')g'', \tag{4.1b}$$

where $f(z,t)$ and $g(z,t)$ are now time-dependent functions satisfying the same boundary conditions as in the steady analysis; see §4.3(Eq. 28) and (Eq. 29). Therefore, these functions are now expressed as

$$f(z,t) = f_0(z) + F(z,t),\ g(z,t) = g_0(z) + G(z,t), \tag{4.2}$$

where $f_0(z)$ and $g_0(z)$ correspond to the basic Stokes profile derived in §4.3(Eq. 15), satisfying the aforementioned boundary conditions §4.3(Eq. 28) and (Eq. 29), and $F(z,t)$ and $G(z,t)$ represent deviations from this profile satisfying Dirichlet-Neumann homogeneous boundary conditions; see §4.3(Eq. 31).

After introducing (4.2) in (4.1), now the initial-boundary value problem reads

$$\begin{aligned} \partial_t F'' &= F^{iv} + (f_0+F+g_0+G)(f_0''' + F''') - (f_0'+F'-g_0'-G')(f_0''+F''), \\ \partial_t G'' &= G^{iv} + (f_0+F+g_0+G)(g_0''' + G''') + (f_0'+F'-g_0'-G')(g_0''+G''), \end{aligned} \tag{4.3}$$

or simply

$$\begin{aligned} \partial_t F'' &= L(F) + N_1(F,G,f_0,g_0), \\ \partial_t G'' &= L(G) + N_2(F,G,f_0,g_0), \end{aligned} \tag{4.4}$$

where L stands for the fourth order linear biharmonic operator, and N_1 and N_2 for the nonlinear differential advective operators.

We now discretise (4.4) using spectral expansions for the time-dependent deviation fields $F(z,t)$ and $G(z,t)$, of the form

$$\begin{bmatrix} F(z,t) \\ G(z,t) \end{bmatrix} = \sum_{m=0}^{M} a_m(t)\Phi_m^{(1)}(z) + b_m(t)\Phi_m^{(2)}(z), \tag{4.5}$$

where $\Phi_m^{(1)}$ and $\Phi_m^{(2)}$ are defined as previously showed in §4.3(Eq. 35).

The Galerkin formulation is applied by substituting the spectral expansion (4.5) in (4.4), followed by the Hermitian projection on the set of orthogonal vector fields $\Phi_m^{(1)}$ and $\Phi_m^{(2)}$; as defined in §4.3(Eq. 36). The result is the nonlinear dynamical system for the spectral coefficients $\mathbf{a}(t) = [a_0\ a_1\ \cdots a_M]^{\mathrm{T}}$ and $\mathbf{b}(t) = [b_0\ b_1\ \cdots b_M]^{\mathrm{T}}$:

$$\sum_{m=0}^{M} A_{\ell m}\,\frac{\mathrm{d}a_m}{\mathrm{d}t} = \sum_{m=0}^{M} B_{\ell m}\,a_m + N_{\ell,1}(\mathbf{a},\mathbf{b}) \tag{4.6a}$$

$$\sum_{m=0}^{M} A_{\ell m}\,\frac{\mathrm{d}b_m}{\mathrm{d}t} = \sum_{m=0}^{M} B_{\ell m}\,b_m + N_{\ell,2}(\mathbf{a},\mathbf{b}) \tag{4.6b}$$

where the matrix elements $A_{\ell m}$ and $B_{\ell m}$ are given by Legendre inner products

$$A_{\ell m} = \int_{-1}^{1} \phi_\ell\,\phi_m''\,\mathrm{d}z, \qquad B_{\ell m} = \int_{-1}^{1} \phi_\ell\,\phi_m^{iv}\,\mathrm{d}z, \tag{4.7}$$

and $N_{\ell,1}(\mathbf{a},\mathbf{b})$ and $N_{\ell,2}(\mathbf{a},\mathbf{b})$ are the projections of the nonlinear terms

$$N_{\ell,1} = \int_{-1}^{1} \phi_\ell\,N_1(\mathbf{a},\mathbf{b})\,\mathrm{d}z, \qquad N_{\ell,2} = \int_{-1}^{1} \phi_\ell\,N_2(\mathbf{a},\mathbf{b})\,\mathrm{d}z. \tag{4.8}$$

All these wall-normal integrals are accurately computed by means of Gauss-Legendre quadrature formulas (Quarteroni *et al.*, 2010). The resulting system of nonlinear ordinary differential equations (4.6) can be expressed as

$$\left[\begin{array}{c|c} A_{\ell m} & 0 \\ \hline 0 & A_{\ell m} \end{array}\right] \left[\begin{array}{c} \dot{\mathbf{a}} \\ \hline \dot{\mathbf{b}} \end{array}\right] = \left[\begin{array}{c|c} B_{\ell m} & 0 \\ \hline 0 & B_{\ell m} \end{array}\right] \left[\begin{array}{c} \mathbf{a} \\ \hline \mathbf{b} \end{array}\right] + \left[\begin{array}{c} N_{\ell,1} \\ \hline N_{\ell,2} \end{array}\right]. \tag{4.9}$$

or for simplicity just

$$\mathbb{A}\dot{\mathbf{x}} = \mathbb{B}\mathbf{x} + \mathbb{N}(\mathbf{x}), \tag{4.10}$$

where $\mathbf{x} = [a_0\ a_1\ \cdots a_M\ b_0\ b_1\ \cdots b_M]^{\mathrm{T}}$, and $\dot{\mathbf{x}}$ stands for time differentiation.

The time integration is carried out with a 4^{th}-order IMEX method (BDF4 backward-differences linearly-implicit method for the linear biharmonic term and 4^{th}-order explicit extrapolation for the nonlinear term), whose linear multistep formula reads

$$\begin{aligned} &(25\mathbb{A} - 12\Delta t\mathbb{B})\mathbf{x}^{(j+1)} = \\ &\quad \mathbb{A}(48\mathbf{x}^{(j)} - 36\mathbf{x}^{(j-1)} + 16\mathbf{x}^{(j-2)} - 3\mathbf{x}^{(j-3)}) \\ &\quad + \Delta t(48\mathbb{N}^{(j)} - 72\mathbb{N}^{(j-1)} + 48\mathbb{N}^{(j-2)} - 12\mathbb{N}^{(j-3)}), \end{aligned} \tag{4.11}$$

where $\mathbf{x}^{(j)} = \mathbf{x}(j\Delta t)$. All DNS computations are initiated with a 4^{th}-order explicit Runge-Kutta method.

4.4.2 Linear stability of steady solutions

Linear stability analysis formally consists in adding infinitesimal perturbations of order $O(\varepsilon)$ to an equilibrium solution $(F_0(z), G_0(z))$ of system (4.3), so that the expressions for deviations from basic Stokes profile now read

$$\begin{aligned} F(z,t) &= F_0(z) + \varepsilon \widetilde{F}(z,t), \\ G(z,t) &= G_0(z) + \varepsilon \widetilde{G}(z,t), \end{aligned} \tag{4.12}$$

where $\widetilde{F}(z,t) = \mathrm{e}^{\lambda t}\mathcal{F}(z)$ and $\widetilde{G}(z,t) = \mathrm{e}^{\lambda t}\mathcal{G}(z)$, with $\mathcal{F}(z)$ and $\mathcal{G}(z)$ being the eigenfunctions of the perturbation associated with the eigenvalue λ, satisfying homogeneous boundary conditions

$$\mathcal{F}(\pm 1) = \mathcal{G}(\pm 1) = \mathcal{F}'(\pm 1) = \mathcal{G}'(\pm 1) = 0. \tag{4.13}$$

Introducing (4.12) in (4.1) and neglecting $O(\varepsilon^2)$ terms leads to the system of linear partial differential equations

$$\begin{aligned} \lambda\mathcal{F}'' = \mathcal{F}^{iv} &+ (f_0 + F_0 + g_0 + G_0)\mathcal{F}''' + (f_0''' + F_0''')(\mathcal{F} + \mathcal{G}) \\ &-(f_0'' + F_0'')(\mathcal{F}' - \mathcal{G}') - (f_0' + F_0' - g_0' - G_0')\mathcal{F}'', \\ \lambda\mathcal{G}'' = \mathcal{G}^{iv} &+ (f_0 + F_0 + g_0 + G_0)\mathcal{G}''' + (g_0''' + G_0''')(\mathcal{F} + \mathcal{G}) \\ &+(g_0'' + G_0'')(\mathcal{F}' - \mathcal{G}') + (f_0' + F_0' - g_0' - G_0')\mathcal{G}'', \end{aligned} \tag{4.14}$$

or, for simplicity,

$$\begin{aligned} \lambda\mathcal{F}'' &= C_1(\mathcal{F}, \mathcal{G}, F_0, G_0, f_0, g_0), \\ \lambda\mathcal{G}'' &= C_2(\mathcal{F}, \mathcal{G}, F_0, G_0, f_0, g_0), \end{aligned} \tag{4.15}$$

We again discretise the eigenperturbations using Legendre spectral expansions

$$\begin{bmatrix} \mathcal{F}(z) \\ \mathcal{G}(z) \end{bmatrix} = \sum_{m=0}^{M} \widetilde{a}_m \Phi_m^{(1)}(z) + \widetilde{b}_m \Phi_m^{(2)}(z). \tag{4.16}$$

After the corresponding Hermitian projections, as formulated in §4.3(Eq. 36), the linear stability analysis is reduced to solve a $2(M+1)$-dimensional generalised eigenvalue problem of the form

$$\lambda \mathbb{A}\mathbf{x} = \mathbb{C}\mathbf{x}, \tag{4.17}$$

or more specifically

$$\lambda \left[\begin{array}{c|c} A_{\ell m} & 0 \\ \hline 0 & A_{\ell m} \end{array}\right] \left[\begin{array}{c} \mathbf{a} \\ \hline \mathbf{b} \end{array}\right] = \left[\begin{array}{c} C_{\ell,1} \\ \hline C_{\ell,2} \end{array}\right] \left[\begin{array}{c} \mathbf{a} \\ \hline \mathbf{b} \end{array}\right], \tag{4.18}$$

where $C_{\ell,1}$ and $C_{\ell,2}$ are the projections given by the Legendre inner products

$$C_{\ell,1} = \int_{-1}^{1} \phi_\ell \, C_1(\mathbf{a}, \mathbf{b}) \, \mathrm{d}z, \qquad C_{\ell,2} = \int_{-1}^{1} \phi_\ell \, C_2(\mathbf{a}, \mathbf{b}) \, \mathrm{d}z. \tag{4.19}$$

Instead of computing the full spectrum, we search for its leading eigenvalues, usually the ten rightmost, by using Arnoldi iteration method combined with suitable Cayley transformations (Trefethen & Bau, 1997).

4.5 Concluding remarks

Explorations started with a two-dimensional acceleration configuration, that is, one plate stretching and the other at rest. With this special configuration, which allows for the coexistence of two- and three-dimensional structures, we showed that the two-dimensional flows initially reported by Wang & Wu (1995) are particular instances of our generalised three-dimensional families.

As a result of the explorations, seven families of three-dimensional solutions have been identified. Due to the boundary conditions arrangement, symmetric relations between different solutions become evident when analysing the fields. In fact, three of them are completely independent and the other four are related in pairs by suitably combined reflectional and rotational transformations. Not surprisingly, the most interesting solutions with intricated branches are concentrated in the neighbourhood of some stretching-shrinking configurations, when both plates are driven with the same acceleration rate. Around these regions, solution branches interact by means of fold and codimension-2 cusp bifurcations, leading to an isolated branch when both plates are symmetrically shrinking. This increase in the complexity of the topology of equilibria in the vicinity of symmetric acceleration rates has also been observed in other extensional flow studies (Marques *et al.*, 2017; Marques & Meseguer, 2019).

The numerical reliability of the results here presented has been systematically checked by monitoring the exponential decay of the spectral expansion coefficients, confirming that all reported flows are genuine solutions of the governing equations.

Chapter 5

Final conclusions

For most technological and engineering applications involving fluid motion, turbulence is a major concern often leading to additional energy consumption, frictional looses, structural stresses or vibrations. Particularly in these cases, studying the origin of turbulence is a crucial necessary precondition for proposing innovative techniques to mitigate or even suppress its detrimental effects.

From a deterministic point of view, turbulence is understood as a chaotic state driven by several equilibria, i.e., exact coherent structures, of the governing equations. In this state, the flow is continuously approaching and escaping from unstable coherent structures, so that, in each of the subsequent rendezvous with exact solutions, some kind of organised spatio-temporal patterns are identified. In fact, turbulence is the result of a transitional process that starts from the first nonlinear structures. These initial solutions, usually in the form of nonlinear equilibria or travelling waves, undergo a sequence of instabilities that progressively increase flow complexity and finally lead to chaotic motion. Therefore, analysing the nature and evolution of these coherent states is a key element for understanding the production and sustainment of turbulence.

In the first work we have explored transition by means of intervening *Tollmien-Schlichting* waves, which arise from two-dimensional instabilities. We have identified a new symmetry-breaking instability leading to asymmetric travelling waves that, according to recent explorations, play an important role in the dynamics at sufficiently high Reynolds numbers (Markeviciute & Kerswell, 2021). However, their relevance to three-dimensional channel flows is still unexplored. Thus, the homotopic

extension of these solutions, gradually extending in the third dimension, remain an interesting object for future work. In addition, space-time-modulation instabilities responsible for the localisation mechanisms have been further analysed, reporting a novel branch-connection scenario.

By contrast, in Taylor-Couette flow it is the competition between centrifugal and shear instabilities that is responsible for the appearance of a vast range of rich nonlinear patterns. Dynamical explorations in this problem reveal intricated transition routes depending on the parameter choice, as a slight variation in inner or outer cylinder rotation rates produces a significant change in the dynamics. For instance, when the outer cylinder is at rest, transition is progressive with a simple supercritical path towards chaotic states. However, in the counter-rotation regime turbulence coexists with the stable laminar base flow, exhibiting significant hysteretical cycles depending on the exploration path. In these cases, exact coherent structures emanated from saddle-node bifurcations act as underlying solutions sustaining turbulence, typically appearing in the form of intermittency, i.e., laminar-turbulent patterns such as turbulent spots or spiral turbulence. Therefore, finite-amplitude perturbations on the laminar flow could trigger transition in the absence of linear instability.

In this problem, nonlinear interactions between classical base flow instabilities and the new mode reported by Deguchi (2017) have been analysed. All explorations have been carried out in a particular computational domain, suitably tilted in the direction of the spirals. This new domain definition, initially proposed by Deguchi & Altmeyer (2013), efficiently adapts to the coherent structures and reduces significantly the computational cost as compared to the classical orthogonal domains. Although the computed emerging structures qualitatively resemble the laminar-turbulent pattern of spiral turbulence, they are found to be supercritical within the explored region. Therefore, the coexistence of both structures has not been observed and their role as a possible precursor of spiral turbulence remains unclear. Preliminary explorations, currently under scrutiny, provide sound evidence that using suitably adapted non-orthogonal domains allows for the identification of underlying coherent structures within spiral turbulence.

The generalisation of flows between biorthogonally stretching and shrinking parallel plates has also been analysed within the framework of this thesis. This kind of flows, strongly influenced by several symmetries, exhibit a peculiar transition sce-

nario. For the lowest wall acceleration rates, up to seven different steady solutions have been identified, even though some of them are symmetry related. When increasing these rates, the topology of equilibria in phase space gradually increases in complexity, as the solution families soon interact by means of fold or codimension-2 cusp bifurcations. Moreover, an interesting feature is that the most complex topology and bifurcation scenarios are found in the vicinity of symmetric stretching-shrinking configurations, when both plates are driven with the same acceleration rates. This becomes specially evident in the case when both plates are simultaneously shrinking. The dynamical relevance of the identified steady flows is currently being explored by means of Arnoldi linear stability analysis as well as time integration of the initial value problem. This results will be addressed in future work.

In this thesis, three types of hydrodynamic instability mechanisms have been successfully studied by means of a wide variety of numerical techniques, ranging from spectral methods to Newton-Krylov solvers, arclength continuations and the Arnoldi iteration method. Such numerical methods, in combination with bifurcation and dynamical systems theory, provide a deterministic approach to the understanding of the different routes to turbulence that fluid flows may exhibit.

When comparing the transition scenarios explored in the course of this thesis, it is clear that the underlying mechanisms are diverse and geometry dependent. Although some basic features and bifurcation scenarios are widely observed, each flow exhibits its own characteristic features and peculiarities. However, the study of these canonical flows with simple geometries provides valuable insight into the types and scope of bifurcation scenarios and transition routes that might be expected in more complex flows that remain still far from the reach of available numerical methods and computational resources.

Bibliography

Andereck, C. D., & Hayot, F. 2012. *Ordered and turbulent patterns in Taylor-Couette flow.* Vol. 297. Springer Science & Business Media.

Andereck, C. D., Liu, S. S., & Swinney, H. L. 1986. Flow regimes in a circular Couette system with independently rotating cylinders. *J. Fluid Mech.*, **164**, 155–183.

Ariel, P. D. 2003. Generalized three-dimensional flow due to a stretching sheet. *Z. Angew. Math. Mech.*, **83**(12), 844–852.

Arnoldi, W. E. 1951. The principle of minimized iterations in the solution of the matrix eigenvalue problem. *Quarterly of applied mathematics*, **9**(1), 17–29.

Ayats, R., Deguchi, K., Mellibovsky, F., & Meseguer, A. 2020a. Fully nonlinear mode competition in magnetised Taylor-Couette flow. *J. Fluid Mech.*, **897**, A14.

Ayats, R., Meseguer, A., & Mellibovsky, F. 2020b. Symmetry-breaking waves and space-time modulation mechanisms in two-dimensional plane Poiseuille flow. *Physical Review Fluids*, **5**, 094401.

Ayats, R., Marques, F., Meseguer, A., & Weidman, P.D. 2021. Flows between orthogonally stretching parallel plates. *Physics of Fluids*, **33**(2), 024103.

Aziz, T., & Mahomed, F. M. 2016. Remark on classical Crane's solution of viscous flow past a stretching plate. *Applied Mathematics Letters*, **52**, 205–211.

Babenko, V. V., & Surkina, R. M. 1969. Some hydrodynamic features of dolphin swimming. *Bionika*, **3**, 19–26.

Balbus, S., & Hawley, J. F. 1991. A powerful local shear instability in weakly magnetised disks. I. Linear analysis. *Astrophys. J.*, **376**, 214–222.

Barkley, D., & Tuckerman, L. S. 2005. Computational study of turbulent laminar patterns in Couette flow. *Phys. Rev. Lett.*, **94**(1), 014502.

Blasius, H. 1908. Grenzschichten in Flüssigkeiten mit kleiner Reibung. *Zeits. f. Math. u. Phys.*, **56**, 1–37.

Brady, J. F., & Acrivos, A. 1981. Steady flow in a channel or tube with an accelerating surface velocity. An exact solution to the Navier–Stokes equations with reverse flow. *J. Fluid Mech.*, **112**, 127–150.

Brandt, Luca. 2014. The lift-up effect: The linear mechanism behind transition and turbulence in shear flows. *Eur. J. Mech. B Fluids*, **47**(sep).

Carpenter, P. W., Davies, C., & Lucey, A. D. 2000. Hydrodynamics and compliant walls: Does the dolphin have a secret? *Current Science*, 758–765.

Casas, P. S., & Jorba, A. 2004. Unstable manifold computations for the two-dimensional plane Poiseuille flow. *Theor. Comput. Fluid Dyn.*, **18**(2), 285–299.

Casas, P. S., & Jorba, A. 2012. Hopf bifurcations to quasi-periodic solutions for the two-dimensional plane Poiseuille flow. *Comm. Nonlinear Sci. Num. Simul.*, **17**(7), 2864–2882.

Chandrasekhar, S. 1960. The stability of non-dissipative Couette flow in hydromagnetics. *Proc. Nat. Acad. Sci.*, **46**, 253–257.

Chossat, P., & Iooss, G. 1994. *The Couette-Taylor Problem.* Springer-Verlag.

Coles, D. 1965. Transition in circular Couette flow. *J. Fluid Mech.*, **21**, 385–425.

Coles, D., & Van Atta, C. W. 1967. Digital experiment in spiral turbulence. *Phys. Fluids Suppl.*, **121**, S120–S121.

Collier, F. S. 1994. Recent Progress in the Development of Laminar Flow Aircraft. *Page 2436 of: ICAS proceedings*, vol. 19.

Couette, M. 1888. Sur un nouvel appareil pour l'étude du frottement des fluides. *Compt. Rend. Acad. Sci. Paris*, **107**, 388–390.

Coullet, P. H., & Spiegel, E. A. 1983. Amplitude equations for systems with competing instabilities. *SIAM J. Appl. Math.*, **43**(4), 776–821.

Cox, S. M., & Matthews, P. C. 2002. Exponential time differencing for stiff systems. *J. Comput. Phys.*, **176**(2), 430–455.

Crane, L. J. 1970. Flow past a stretching plate. *Z. Angew. Math. Phys.*, **21**, 645–647.

Crowley, C. J., Krygier, M. C., Borrero-Echeverry, D., Grigoriev, R. O., & Schatz, M. F. 2020. A novel subcritical transition to turbulence in Taylor-Couette flow with counter-rotating cylinders. *J. Fluid Mech.*, **892**, A12.

Deguchi, K. 2017. Linear instability in Rayleigh-stable Taylor-Couette flow. *Phys. Rev. E*, **95**, 021102.

Deguchi, K., & Altmeyer, S. 2013. Fully nonlinear mode competitions of nearly bicritical spiral or Taylor vortices in Taylor-Couette flow. *Phys. Rev. E*, **87**, 043017.

Drazin, P. G., & Riley, N. 2006. *The Navier-Stokes Equations, A Classification of Flows and Exacts Solutions.* Cambridge: Cambridge University Press.

Drazin, P. G., & Reid, W. H. 1981. *Hydrodynamic Stability.* Cambridge University Press.

Duda, D., Klimko, M., Skach, R., Uher, J., & Uruba, V. 2019. Hydrodynamic education with rheoscopic fluid. *EPJ Web Conf.*, **213**, 2014.

Eckhardt, B., Faisst, H., Schmiegel, A., & Schneider, T. M. 2008. Dynamical systems and the transition to turbulence in linearly stable shear flows. *Phil. Trans. Roy. Soc. Lond. A*, **366**(1868), 1297–1315.

Eckmann, J. P. 1981. Roads to turbulence in dissipative dynamical systems. *Rev. Mod. Phys.*, **53**, 643–654.

Ehrenstein, U., & Koch, W. 1991. Three-dimensional wavelike equilibrium states in plane Poiseuille flow. *J. Fluid Mech.*, **228**, 111–148.

Espin, Leonardo, & Papageorgiou, Demetrios T. 2009. Flow in a channel with accelerating or decelerating wall velocity: A comparison between self-similar solutions and Navier-Stokes computations in finite domains. *Phys. Fluids*, **21**(11).

Feigenbaum, Mitchell J. 1978. Quantitative universality for a class of nonlinear transformations. *J. Stat. Phys.*, **19**(07).

Hof, B., Juel, A., & Mullin, T. 2003. Scaling of the turbulence transition threshold in a pipe. *Phys. Rev. Lett.*, **91(24)**, 244502.

Hof, B., van Doorne, C. W. H., Westerweel, J., M., Nieuwstadt F. T., Holger Faisst, H., Eckhardt, B., Wedin, H., Kerswell, R. R., & Waleffe, F. 2004. Experimental Observation of Nonlinear Traveling Waves in Turbulent Pipe Flow. *Science*, **305**, 1594–1598.

Hopf, E. 1942. Abzweigung einer periodischen Lösung von einer stationären Lösung eines Differentialsystems. *Ber. Math.-Phys. Kl Sächs. Akad. Wiss. Leipzig*, **94**, 1–22.

Hopf, E. 1948. A mathematical example displaying features of turbulence. *Commun. Pure Appl. Math.*, **1**(4), 303–322.

IATA. 2019. *Aircraft Technology Roadmap to 2050.*

Kagan, D., & Wheeler, J. C. 2014. The role of the magnetorotational instability in the Sun. *Astrophys. J.*, **787**(1), 21.

Kármán, T. 1930. Mechanische Ähnlichkeit und Turbulenz. *Proc. 3. Int. Cong. Appl. Mech*, 322–346.

Kawahara, G., Uhlmann, M., & Van Veen, L. 2012. The significance of simple invariant solutions in turbulent flows. *Ann. Rev. Fluid Mech.*, **44**, 203–225.

Kelley, C.T. 2003. *Solving nonlinear equations with Newton's method.* SIAM.

Kerswell, R. R. 2005. Recent progress in understanding the transition to turbulence in a pipe. *Nonlinearity*, **18**(6), R17.

King, G. P., Li, Y., Lee, W., Swinney, H. L., & Marcus, P. S. 1984. Wave speeds in wavy Taylor-vortex flow. *J. Fluid Mech.*, **141**, 365–390.

Kolmogorov, A. N. 1941. The local structure of turbulence in incompressible viscous fluid for very large Reynolds numbers. *Dokl. Akad. Nauk SSSR*, **30**, 299–301.

Kreilos, T., & Eckhardt, B. 2012. Periodic orbits near onset of chaos in plane Couette flow. *Chaos*, **22**(4), 047505.

Krygier, M. C., Pughe-Sanford, J. L., & Grigoriev, R. O. 2021. Exact coherent structures and shadowing in turbulent Taylor–Couette flow. *J. Fluid Mech.*, **923**, A7.

Kuznetsov, Y. A. 2004. *Elements of Applied Bifurcation Theory.* 3 edn. Springer.

Landau, L. D. 1944. On the problem of turbulence. *Dokl. Akad. Nauk SSSR*, **44**, 339–342.

Landau, L. D., & Lifshitz, E. M. 1984. Chapter VIII - Magnetohydrodynamics. *Pages 225–256 of: Electrodynamics of Continuous Media (Second Edition)*, second edition edn. Course of Theoretical Physics, vol. 8. Pergamon.

Mallock, A. 1889. Determination of the viscosity of water. *Proc. Roy. Soc. Lond.*, **45**(273-279), 126–132.

Manneville, P. 2010. *Instabilities, chaos and turbulence.* Vol. 1. World Scientific.

Markeviciute, V. K., & Kerswell, R. R. 2021. Degeneracy of turbulent states in two-dimensional channel flow. *J. Fluid Mech.*, **917**, A57.

Marques, F., & Meseguer, A. 2019. Extensional and torsional pipe flow. *Physical Review Fluids*, **4**, 103908.

Marques, F., Meseguer, A., Mellibovsky, F., & Weidman, P.D. 2017. Extensional channel flow revisited: a dynamical systems perspective. *Proc. Roy. Soc. Lond. A*, **473**, 20170151.

Masada, Y. 2011. Impact of magnetohydrodynamic turbulence on thermal wind balance in the Sun. *Mon. Not. R. Astron. Soc.: Lett.*, **411**(1), L26–L30.

Mellibovsky, F., & Eckhardt, B. 2012. From travelling waves to mild chaos: a supercritical bifurcation cascade in pipe flow. *J. Fluid Mech.*, **709**, 149–190.

Mellibovsky, F., & Meseguer, A. 2009. Critical threshold in pipe flow transition. *Phil. Trans. Roy. Soc. Lond. A*, **367**, 449–455.

Mellibovsky, F., & Meseguer, A. 2015. A mechanism for streamwise localisation of nonlinear waves in shear flows. *J. Fluid Mech.*, **779**, R1–1.

Melnikov, K., Kreilos, T., & Eckhardt, B. 2014. Long-wavelength instability of coherent structures in plane Couette flow. *Phys. Rev. E*, **89**, 043008.

Meseguer, A. 2002. Energy transient growth in the Taylor-Couette problem. *Phys. Fluids*, **14**(5), 1655–1660.

Meseguer, A., Avila, M., Mellibovsky, F., & Marques, F. 2007. Solenoidal spectral formulations for the computation of secondary flows in cylindrical and annular geometries. *Eur. Phys. J. Spec. Top.*, **146**(1), 249–259.

Meseguer, A., Mellibovsky, F., Avila, M., & Marques, F. 2009a. Families of subcritical spirals in highly counter-rotating Taylor-Couette flow. *Phys. Rev. E*, **79**, 036309.

Meseguer, A., Mellibovsky, F., Avila, M., & Marques, F. 2009b. Instability mechanisms and transition scenarios of spiral turbulence in Taylor-Couette flow. *Phys. Rev. E*, **80**, 046315.

Meseguer, Alvaro. 2020. *Fundamentals of Numerical Mathematics for Physicists and Engineers.* John Wiley & Sons.

Nagata, M. 1990. Three-dimensional finite-amplitude solutions in plane couette flow: Bifurcation from infinity. *J. Fluid Mech.*, **217**, 519–527.

Orr, W. M. F. 1907. The stability or instability of the steady motions of a perfect liquid and of a viscous liquid. Part II: A viscous liquid. *Math. Proc. R. Ir. Acad.*, **27**, 69–138.

Orszag, S. A. 1971. Numerical simulation of incompressible flows with simple boundaries-accuracy. *J. Fluid Mech.*, **49**, 75–112.

Page, J., Dubief, Y., & Kerswell, R. R. 2020. Exact Traveling Wave Solutions in Viscoelastic Channel Flow. *Phys. Rev. Lett.*, **125**, 154501.

Paranjape, C. S., Duguet, Y., & Hof, B. 2020. Oblique stripe solutions of channel flow. *J. Fluid Mech.*, **897**, A7.

Piau, J. M., Brémond, M., Couette, J., & Piau, M. 1994. Maurice Couette, one of the founders of rheology. *Rheologica Acta*, **33**, 357–368.

Poincaré, Henri. 2017. *The three-body problem and the equations of dynamics: Poincaré's foundational work on dynamical systems theory.* Vol. 443. Springer.

Pomeau, Y., & Manneville, P. 1980. Intermittent transition to turbulence in dissipative dynamical systems. *Commun. Math. Phys.*, **74**, 189–197.

PRANDTL, L. 1904. Über Flüssigkeitsbewegung bei sehr kleiner Reibung. *Verhandlungen des III. Internationalen Mathematiker Kongresses, Heidelberg*, 484–491.

PRAT, J., MERCADER, I., & KNOBLOCH, E. 1998. Resonant mode interactions in Rayleigh-Bénard convection. *Phys. Rev. E*, **58**, 3145–3156.

PUGH, J.D., & SAFFMAN, P.G. 1988. Two-dimensional superharmonic stability of finite-amplitude waves in plane Poiseuille flow. *J. Fluid Mech.*, **194**, 295–307.

QUARTERONI, ALFIO, SACCO, RICCARDO, & SALERI, FAUSTO. 2010. *Numerical mathematics*. Vol. 37. Springer Science & Business Media.

RAMADIER, S. 2017. *A340 laminar flow BLADE demonstrator.* `http://web.archive.org/web/20080207010024/http://www.808multimedia.com/winnt/kernel.htm`. Airbus.

RAYLEIGH, L. 1917. On the Dynamics of Revolving Fluids. *Proc. Roy. Soc. Lond. A*, **93**(648), 148–154.

RAYLEIGH, LORD. 1879. On the Stability, or Instability, of certain Fluid Motions. *Proc. London Math. Soc.*, **s1-11**(1), 57–72.

REETZ, F., KREILOS, T., & SCHNEIDER, T. M. 2019. Exact invariant solution reveals the origin of self-organized oblique turbulent-laminar stripes. *Nat. Commun.*, **10**, 2277.

REYNOLDS, OSBORNE. 1883. An experimental investigation of the circumstances which determine whether the motion of water shall be direct or sinuous, and of the law of resistance in parallel channels. *Phil. Trans. R. Soc.*, **174**, 935–982.

RITTER, P., MELLIBOVSKY, F., & AVILA, M. 2016. Emergence of spatio-temporal dynamics from exact coherent solutions in pipe flow. *New J. Phys.*, **18**(8), 083031.

ROZHDESTVENSKY, B. L., & SIMAKIN, I. N. 1984. Secondary flows in a plane channel: their relationship and comparison with turbulent flows. *J. Fluid Mech.*, **147**, 261–289.

RUELLE, T., & TAKENS, F. 1971. On the nature of turbulence. *Commun. Math. Phys.*, **20**, 167–192.

SARIC, W. S., REED, H. L., & WHITE, E. B. 2003. Stability and transition of three-dimensional boundary layers. *Annu. Rev. Fluid Mech.*, **35**(1), 413–440.

SCHLICHTING, H. 1933. Berechnung der Anfachung kleiner Störungen bei der Plattenströmung. *Zeits. f. Math. u. Mech.*, **13**, 171–174.

SCHMID, P. J., & HENNINGSON, D. S. 2001. *Stability and Transition in Shear Flows*. 1 edn. Applied Mathematical Sciences. Springer-Verlag New York.

SCHNEIDER, T. M., ECKHARDT, B., & YORKE, J. A. 2007. Turbulence transition and the edge of chaos in pipe flow. *Phys. Rev. Lett.*, **99**(3), 034502.

SCHNEIDER, T.M., GIBSON, J.F., & BURKE, J. 2010. Snakes and ladders: Localized solutions of plane Couette flow. *Phys. Rev. Lett.*, **104**.

SCHRAUF, G. 2005. Status and perspectives of laminar flow. *The aeronautical journal*, **109**(1102), 639–644.

SCHUBAUER, G. B., & SKRAMSTAD, H. K. 1947. Laminar Boundary-Layer Oscillations and Stability of Laminar Flow. *Journal of the Aeronautical Sciences*, **14**(2), 69–78.

SOMMERFELD, A. 1908. Ein Beitrag zur hydrodynamischen Erklärung der turbulenten Flüssigkeitsbewegungen. *Pages 116–124 of: Prooceedings 4th International Congress of Mathematicians*, vol. 3.

SQUIRE, H. B. 1933. On the stability for three-dimensional disturbances of viscous fluid flow between parallel walls. *Proc. Roy. Soc. Lond. A*, **142**(847), 621–628.

TAGG, R. 1994. The Couette-Taylor problem. *Nonlinear Sci. Today*, **4(3)**, 1–25.

TAYLOR, G. I. 1923. Stability of a viscous fluid contained between two rotating cylinders. *Phil. Trans. Roy. Soc. Lond. A*, **223**, 289–343.

THOMAS, L. H. 1953. The Stability of Plane Poiseuille Flow. *Phys. Rev.*, **91**, 780–783.

TOLLMIEN, W. 1928. Über die Entstehung der Turbulenz. 1. Mitteilung. *Nachr. Ges. Wiss. Gottingen, Math.-Phys. Kl.*, **1929**, 21–44.

TREFETHEN, L. N., & BAU, D. 1997. *Numerical Linear Algebra*. Philadelphia: SIAM.

VAN ATTA, C. 1966. Exploratory measurements in spiral turbulence. *J. Fluid Mech.*, **25**, 495–512.

VELIKHOV, E. P. 1959. Stability of an ideally conducting liquid flowing between cylinders rotating in a magnetic field. *Soviet. Phys. JETP*, **36**, 1389–1404.

VISWANATH, D. 2007. Recurrent motions within plane Couette turbulence. *J. Fluid Mech.*, **580**, 339–358.

WALEFFE, F. 1997. On a self-sustaining process in shear flows. *Phys. Fluids*, **9**, 883–900.

WALEFFE, F. 2003. Homotopy of exact coherent structures in plane shear flows. *Phys. Fluids*, **15(6)**, 1517–1534.

WANG, C. Y. 1984. The three-dimensional flow due to a stretching flat surface. *Phys. Fluids*, **27**, 1915.

WANG, CHING-AN, & WU, TU-CHENG. 1995. Similarity solutions of steady flows in a channel with accelerating walls. *Comput. Math. Applic.*, **30**(10), 1–16.

WATERS, S. L. 2001. Solute uptake through the walls of a pulsating channel. *J. Fluid Mech.*, **433**, 193–208.

WATERS, S. L. 2004. A mathematical model for the laser treatment of heart disease. *J. Biomech.*, **37**, 281–288.

WEDIN, H., & KERSWELL, R. R. 2004. Exact coherent structures in pipe flow: travelling wave solutions. *J. Fluid Mech.*, **508**, 333–371.

WEIDMAN, P.D., & ISHAK, A. 2015. Multiple solutions of two-dimensional and three-dimensional flows induced by a stretching flat surface. *Commun. Nonlinear Sci. Numer. Simul.*, **25**, 1–9.

ZAMMERT, S., & ECKHARDT, B. 2014. Streamwise and doubly-localised periodic orbits in plane Poiseuille flow. *J. Fluid Mech.*, **761**, 348–359.